The Stabilizing Influence of Radiofrequency Phase Modulation Counteracting Coupled-Bunch Instabilities

Dissertation

zur Erlangung des akademischen Grades
Doktor der Naturwissenschaften
(Dr. rer. nat.)
vorgelegt der Fakultät Physik
der Technischen Universität Dortmund

Malte Sommer
geboren am 27.07.1988 in Herdecke

November 2019

Vorsitzender der Prüfungskomission: Prof. Dr. Markus Betz

1. Gutachter : Prof. Dr. Shaukat Khan

2. Gutachter : Prof. Dr. Andreas Jankowiak

Vetreter der wissenschaftlichen Mitarbeiter: Dr. Christian Sternemann

Tag der mündlichen Prüfung: 24. Februar 2020

Abstract

Synchrotron radiation sources have become an essential part of modern science. The ongoing development to reach higher performance levels with improved quality of synchrotron light demands upgrades of current synchrotron radiation facilities or even construction of new accelerators. During this process, new challenges, both technological and in the accelerator physics, need to be addressed to achieve a higher light quality in terms of brightness, coherence, pulse duration, etc. This includes the suppression of coupled-bunch instabilities. These instabilities are based on the interaction of the accelerated particles with the vacuum chamber surrounding them, especially the accelerating cavities. Beam instabilities can significantly lower the beam quality or even result in particle loss.

The development of digital bunch-by-bunch feedback systems in the 1990's made detailed analysis of coupled-bunch instability eigenmodes possible, replacing the former approaches to counteract coupled-bunch instabilities like analog feedback systems or radiofrequency (RF) phase modulation. Since the coupled-bunch effects increase in upcoming storage rings due to, e.g., higher beam currents and smaller vacuum chambers, the suppression of instabilities is once again in the focus of current accelerator research.

The scope of this thesis is to use a digital bunch-by-bunch feedback system to analyze and quantify the suppression of longitudinal coupled-bunch instabilities by RF phase modulation. Both options are available at DELTA, a 1.5 GeV electron storage ring operated by the TU Dortmund University. For this purpose, a numerical tracking code was developed. It is capable of analyzing coupled-bunch instabilities in the presence of a modulated RF phase. The numerical results show that the instability growth rates decrease quadratically with the modulation amplitude. In addition, a new method was established to measure the growth and damping rates of coupled-bunch instability modes in the presence of RF phase modulation. The results also show a quadratic dependence on the modulation amplitude.

Based on the knowledge and experienced gained throughout this work, studies were performed in order to improve the user operation of the DELTA storage ring. An investigation

of the injection process at DELTA showed that the injection efficiency can be increased with the bunch-by-bunch feedback system. In addition, a beam-stability map was created by sweeping the parameters of the RF phase modulation system and the optimal parameters for user operation were found. Thereupon, two new easy-to-use tools were added to the DELTA control system which help to utilize the bunch-by-bunch feedback system during user operation.

Zusammenfassung

Heutzutage sind Synchrotronstrahlungsquellen ein wichtiges Element der modernen Forschung. Die kontinuierliche Weiterentwicklung zur Erzeugung höherer Lichtqualität, erfordert die Erweiterung bestehender Strahlungsquellen bzw. den Bau neuer Anlagen. Durch die laufend steigenden Anforderungen der Nutzer von Synchrotronstrahlung in Bezug auf Brillanz, Kohärenz, Pulsdauer etc., müssen stetig neue technische und physikalische Herausforderungen bewältigt werden. Im Besonderen gilt dies auch für kollektive Schwingungen der Teilchenpakete. Diese Instabilitäten basieren auf der Wechselwirkung der beschleunigten Teilchenpakete mit der sie umgebenden Vakuumkammer, insbesondere den zur Beschleunigung verwendeten Hochfrequenz(HF)-Resonatoren. Diese Effekte können die Strahlqualität beeinträchtigen oder sogar zum Strahlverlust führen.

Mit der Entwicklung von so genannten “bunch-by-bunch”-Rückkoppelsystemen in den 1990er Jahren, ist es möglich geworden, kollektive Schwingungsmoden im Detail zu untersuchen und ihnen entgegenzuwirken. Dadurch wurden die bis dahin verwendeten Systeme wie z.B. analoge Rückkoppelsysteme oder HF-Phasenmodulation, größtenteils von digitalen “bunch-by-bunch”-Rückkoppelsystemen abgelöst. Da die Anregung von Strahlinstabilitäten mit der Entwicklung neuer Beschleunigermodelle kontinuierlich steigt, z.B. aufgrund höherer Strahlströme und kleinerer Vakuumkammern, ist die Dämpfung dieser Effekte weiterhin ein wichtiger Bestandteil der aktuellen Beschleunigerforschung.

Im Rahmen dieser Arbeit wurde der Effekt von der Phasenmodulation der beschleunigenden HF-Spannung auf die Strahldynamik untersucht. Dazu wurde ein “bunch-by-bunch”-Rückkoppelsystem verwendet, um die auftretenden Strahlinstabilitäten in Abhängigkeit der Einstellparameter des Phasenmodulationssystems zu analysieren. An DELTA, einem 1.5-GeV-Elektronenspeicherring, der von der TU Dortmund betrieben wird, stehen beide Optionen zur Verfügung.
Zu diesem Zweck wurde ein numerisches Programm entwickelt, das kollektive Schwingungen der Teilchenpakete unter Einfluss einer phasenmodulierten HF-Spannung untersucht. Die Ergebnisse zeigen, dass die Anwachsraten der Instabilitäten eine quadratische

Abhängigkeit zur Amplitude der Phasenmodulation haben. Zusätzlich wurde eine neue Messmethode entwickelt mit der die Anwachsraten der Strahlinstabilitäten unter Einfluss der Phasenmodulation untersucht werden können. Die experimentellen Ergebnisse zeigen ebenfalls eine quadratische Abhängigkeit.

Anschließend wurden weitere Studien durchgeführt, um den Nutzerbetrieb an DELTA zu verbessern. Es wurde gezeigt, dass die Injektionseffizienz mit dem "bunch-by-bunch"-Rückkoppelsystem erhöht werden kann. Das ermöglichte die Erstellung einer Stabilitätskarte des Strahls, indem die Parameter der Phasenmodulation durchgefahren wurden, sodass optimale Parametersätze definiert werden konnten. Daraufhin wurden zwei neue benutzerfreundliche Applikationen zum DELTA-Kontrollsystem hinzugefügt, um das "bunch-by-bunch"-Rückkoppelsystem im Nutzerbetrieb nutzbar zu machen.

Contents

Abstract iv

Zusammenfassung v

Contents vii

List of Figures xi

List of Tables xiii

Glossary xv

1. Introduction and Motivation 1

2. Particle Beam Dynamics and Coupled-Bunch Instabilities 5

2.1. Particle acceleration 6

2.1.1. Longitudinal Electric Fields in Cylindrical Waveguides 6

2.1.2. Cylindrical Resonators 8

2.1.3. RF Phase Modulation 10

2.2. Basic Particle Dynamics 11

2.2.1. Frenet-Serret Coordinates 11

2.2.2. Momentum Compaction Factor 12

2.2.3. Linear Transverse One-Particle Motion 13

2.2.4. Longitudinal One-Particle Motion and Phase Focusing 14
2.2.5. RF Phase Modulation 17
2.3. Longitudinal Wake Fields and Impedances 21
2.3.1. The Beam Spectrum 21
2.3.2. Wake function and Impedance 25
2.3.3. Wake Matrix 26
2.4. Coupled-Bunch Instabilities 28
2.4.1. Particle Dynamics with Synchrotron Radiation and External Excitations 29
2.4.2. Instability Growth Rate 30
2.4.3. Additional Damping Mechanisms 32

3. The Electron Storage Ring DELTA **33**

3.1. Overview 34
3.2. Phase Modulation at DELTA 35
3.3. Bunch-by-Bunch Feedback System 36
3.3.1. BPM and Hybrid Network 38
3.3.2. Processing Units 39
3.3.3. Amplifiers and Kicker Structures 40

4. Beam Dynamics Simulation **43**

4.1. Concept 44
4.2. Choice of Parameters 47
4.3. First Results and Code Validation 48
4.4. Dependence of Coupled-Bunch Growth Rates on the Modulation Amplitude . 51

5. Experimental Studies 53

5.1. Optimum RF Phase Modulation Frequency 54

5.2. Phase Shift Applied in the Accelerating Cavity 55

5.3. Data Acquisition with the Bunch-by-Bunch Feedback System 60

5.4. Determination of Coupled-Bunch Growth and Damping Rates 62

5.5. Coupled-Bunch Instabilities in the Presence of RF Phase Modulation 65

5.6. Studies to Improve User Operation 72

5.6.1. Improving the Injection Efficiency 72

5.6.2. Mapping the Stability of the Beam 74

6. Summary and Outlook 77

A. Appendix 81

A.1. DELTA Cavity Voltage and Phase 81

A.2. Figures of Merit of the DORIS Cavity at DELTA 83

A.3. The Saturation Method 86

B. Acknowledgements 89

References 91

List of Figures

2.1. Field distribution in a pillbox cavity 9

2.2. Spectrum of a phase-modulated signal 11

2.3. Traveling coordinate system along the orbit 12

2.4. Horizontal phase space and acceptance 14

2.5. Dispersion and phase focusing 15

2.6. Longitudinal phase space and separatrix 18

2.7. Longitudinal phase space with two and three stable fix points 19

2.8. Island formation in the longitudinal phase space due to RF phase modulation 20

2.9. Beam spectra of different single- and multibunch setups 23

2.10. Beam spectrum of four coupled bunches 24

2.11. Schematic of an RF-cavity simplified by an RLC parallel-circuit 26

2.12. Bunch motion in the presence of an external driving force 30

3.1. Sketch of the synchrotron radiation source DELTA 33

3.2. RF phase modulation system at DELTA and its characteristic curve 35

3.3. Overview of the digital bunch-by-bunch feedback at DELTA 37

3.4. Beam position monitor and hybrid network 38

3.5. Photo of the bunch-by-bunch feedback system at DELTA 39

3.6. Sketch of the fast pulsed kicker structures used at DELTA 41

4.1. First simulation results of a single particle. 49

4.2. Growth rate as a function of the beam current 50

4.3. Growth rate as a function of the phase modulation amplitude 52

5.1. Sweep of the RF phase modulation frequency to find the optimal value 54

5.2. Analysis of the measured spectrum of the phase modulation system at DELTA 56

5.3. Measured resonance curve of the DELTA cavity 58

5.4. Phase shift as a function of the control voltage amplitude 59

5.5. Mode analysis of a measurement with the bunch-by-bunch feedback system 61

5.6. Grow damp measurements at DELTA 63

5.7. Grow-damp mode signals for different phase shifts 64

5.8. Functions used to reconstruct the measured grow-damp mode signals 66

5.9. Calibration measurements used for the saturation method 68

5.10. Growth or damping rate τ^{-1} as a function of the phase shift 70

5.11. Analysis of the trend of τ_{sat}^{-1} by a second-order polynomial fit 71

5.12. Injection efficiency increase generated by using bunch-by-bunch feedback . 73

5.13. Combined parameter sweep to achieve a stability map 75

6.1. Comparison of simulation data and measurement data 78

List of Tables

3.1. Basic parameters of the DELTA storage ring 34

4.1. Most important parameters used in the first simulation. 48

Glossary

symbol	description	first occurrence
constants of nature		
$c = 299.792\,\mathrm{Mm\,s^{-1}}$	speed of light	5
$e = 1.602 \times 10^{-19}\,\mathrm{C}$	electron charge	12
$m_\mathrm{e} = 510.998\,\mathrm{keV\,c^{-2}}$	electron mass	30
$\mu_0 = 1.257 \times 10^{-6}\,\mathrm{N\,A^{-2}}$	vacuum permeability	6
parameters that are used in multiple chapters		
A_exc	excitaion amplitude	66
A_m	modulation amplitude	17
$\vec{B}$	magnetic flux density	6
D	downsampling factor	39
$\vec{E}$	elctric field strength	6
$\hat{E}$	electric field amplitude	7
E_z	longitudinal electric field strength	7
E_0	nominal particle energy	12
ΔE	energy deviation per turn	12
ΔE_RF	energy change by the RF voltage	14
ΔE_s	energy deviation due to synchrotron radiation	14
ΔE_WF	energy deviation applied by the wake field	46
f	frequency	7
Δf	bandwidth of a resonant structure	40
f_exc	excitation frequency	64
f_mod	modulation frequency	20
f_μ	mode frequency	64
f_rev	revolution frequency	34
f_RF	master RF frequency	34
f_s	synchrotron frequency	34

symbol	**description**	**first occurrence**
f_{samp}	sampling rate	41
h	harmonic number	15
I	beam current	17
I_{max}	maximum beam current	34
I_{thr}	instability threshold	31
$\mathscr{J}_n$	n-th Bessel function	10
k	wave number	7
k_{c}	cutoff wave number	7
k_{z}	longitudinal wave number	7
L_0	circumference of the storage ring	13
ΔL	trajectory length deviation in one turn	13
$\underline{\boldsymbol{M}}$	wake matrix	28
N_{b}	number of bunches (filled buckets)	31
N_{ppb}	number of particles per bunch	30
n_{t}	number of turns	47
$P\left(f_{\mathrm{s}}\right)$	spectral power at the synchrotron frequency	54
$P_{\Sigma}\left(f_{\mathrm{s}}\right)$	mean spectral power at the synchrotron frequency	54
q	particle charge	6
q_{B}	bunch charge	30
Q_0	quality factor	8
Q_{L}	loaded quality factor	9
Q_{r}	quality factor of the impedance structure	46
R	radius (of a waveguide or cavity)	7
R_{b}	bending radius (dipoles)	13
R_{s}	shunt impedance	9
s	orbit coordinate	11
t	time	7
T_{rev}	revolution time	13
ΔT	time deviation per turn	13
t_{acq}	acquisition time	39
T_{RF}	master RF period time	16
t_{tot}	total time since the last bunch passage	47
$\hat{U}$	amplitude of cavity voltage	10
U_{C}	control voltage	35

symbol	description	first occurrence
$\hat{U}_{\mathrm{C}}$	amplitude of the control voltage U_{DC} (peak to peak)	36
U_{DC}	additional DC input voltage	35
U_{mod}	output signal of the phase modulation system	35
$\hat{U}_{\mathrm{mod}}$	amplitude of U_{mod}	35
U_{RF}	master RF signal	35
v, $\vec{v}$	velocity	6
$\vec{W}(z)$	wake field vector	28
$W_{\parallel}$	longitudinal wake function	25
x	horizontal displacement	12
$x' = dx/ds$	horizontal angle	12
X_{mn}	n-th zero of the m-th Bessel function	8
y	vertical displacement	12
$y' = dy/ds$	vertical angle	12
Y_{max}	saturation value	65
z	longitudinal displacement	12
α	momentum compaction factor	13
γ	Lorentz factor	30
$\delta = \Delta E/E_0$	relative energy deviation	12
δE	energy deviation (coordinate)	44
δt	time deviation (coordinate)	44
ϵ	epsilon factor	18
η	modulation index (max. modulation phase shift)	10
κ	coupling factor	9
μ	mode number	24
σ_{T}	temporal standard deviation (normal distribution)	22
τ^{-1}	combination of all growth and damping rates	29
τ_{b}	beam lifetime	17
τ_{D}^{-1}	damping rate	29
τ_{FB}^{-1}	feedback damping rate	32
τ_{fit}^{-1}	τ^{-1} obtained by the fitting method	63
τ_{G}^{-1}	growth rate	29
τ_{sat}^{-1}	τ^{-1} obtained by the saturation method	69
ϕ	phase shift	10
$\Delta\phi$	phase deviation	15

symbol	description	first occurrence
ϕ_{cav}	phase shift inside the accelerating cavity	59
ϕ_{DC}	constant DC phase shift	35
ϕ_{max}	maximum phase shift achievable	60
ϕ_{meas}	phase shift from the measurement	57
ϕ_{PS}	phase shift of the phase modulation system	36
ϕ_{s}	synchronous phase	15
ϕ_{sim}	phase shift from the simulation	57
$\omega = 2\pi f$	angular frequency	7
$\Delta\omega$	resonance bandwidth	8
ω_{c}	frequency of the control voltage U_{DC}	36
ω_{exc}	excitation frequency	66
ω_{mod}	modulation frequency	10
ω_{μ}	frequency of mode μ	28
ω_{r}	resonant frequency (impedance structure)	46
ω_{res}	resonance frequency	8
ω_{rev}	revolution frequency	15
ω_{RF}	master RF frequency	10
ω_{s}	synchrotron frequency	16
abbreviations, acronyms and definitions		
BESSY II	synchroton light source in Berlin, Germany	2
BESSY VSR	variable pulse length storage ring (upgrade BESSY II)	2
BoDo	Booster Dortmund (booster synchrotron at DELTA)	34
BPM	beam position monitor	38
DC	direct current	35
DELTA	electron storage ring in Dortmund, Germany	3
drive	frequency generator of the bunch-by-bunch feedback system	40
HOM	higher-order mode	2
MALTE	coupled-bunch **M**ulti p**A**rtic**L**e **T**racking cod**E**	43
MAX IV	diffraction-limited storage ring in Lund, Sweden	2
RF	radio frequency	2
Sirius	diffraction-limited storage ring in Campinas, Brazil	2

1. Introduction and Motivation

The generation of synchrotron radiation is of particular importance for modern science because of its unique characteristics and properties. It has a broad spectrum from microwave radiation up to the regime of hard x-ray photons with a high flux density, high brilliance, high stability, a pulsed time structure and can be polarized linearly or circularly. Thus, it is used by scientists of many different branches, e.g., solid-state physics, chemistry, crystallography, biology, materials science, surface analysis, medicine, etc. [1]. Synchrotron radiation is emitted by charged particles under circular acceleration in a magnetic field and used for diffraction and scattering experiments, as well as for spectroscopy and imaging purposes. Since its first observation in 1947 [2], synchrotron radiation has evolved rapidly and today, more than 50 dedicated synchrotron light sources around the world [3] deliver brilliant radiation for an ever growing variety of applications.

The beam intesity of third- and upcoming fourth-generation synchrotron radiation facilities is mainly limited by the occurrence of so-called coupled-bunch instabilities [4, 5]. These effects significantly lower the beam quality, and, therefore, also the quality of the emitted synchrotron radiation, or even lead to particle loss of the stored electron beam [4]. Coupled-bunch instabilities are based on the interaction of the accelerated particles with the vacuum chamber surrounding them. While traveling through the accelerator, the particles generate electromagnetic fields, which can act back on other particles inside the beam. The formation of these so-called wake fields depends on the geometry and the electrical resistance of the vacuum chamber. Especially in resonant structures, where wake fields can be sustained for a long period of time relative to the revolution time of the particles, this effect can have a drastic impact on the particle dynamics [6]. If these wake fields have a frequency component at one of the discrete eigenfrequencies of a bunched particle beam, the beam can be excited resonantly, resulting in bunch oscillations with exponentially increasing amplitude leading to beam blowup or even particle loss up to a full beam breakup.

Current developments of synchrotron light sources invest great efforts to achieve an optimum beam quality even at high beam currents to satisfy the increasing demands of the

users. For this purpose, either the bunch length or the transverse profile of the beam is minimized. An example for minimizing the bunch length is the current development of an upgrade for the BESSY II storage ring in Berlin, Germany [7]. The project is called BESSY VSR (variable pulse-length storage ring [8]) and utilizes superconducting multi-cell cavities with very high quality factors to provide an radio frequency (RF) field which allows to store short and long bunches simultaneously, without lowering the total beam current. The short bunches are planned to be ten times shorter than the bunches of BESSY II, but the usage of superconducting RF structures in a storage ring results in a strong coupling between the electron bunches [9].
Minimizing the transverse profile of the beam is aimed for at various facilities, e.g., MAX IV in Lund, Sweden [10] or Sirius in Campinas, São Paulo State, Brazil [11]. These storage rings use special lattice patterns and insertion devices to decrease the beam profile down to the diffraction limit [12]. Nevertheless, an increased coupling impedance as well as an enhancement of the beam sensitivity against collective effects are expected [5]. In conclusion, both approaches lead to problematically high excitation of coupled-bunch instabilities.
Additionally, for high-luminosity colliders like SuperKEKB [13, 14] (which aims for beam currents of 3.6 A resp. 2.6 A), the suppression of coupled-bunch instabilities is very important as those instabilities present the main limit to the maximum beam current. Therefore, collective effects are being investigated worldwide to achieve a deeper understanding and to find solutions to counteract or prevent them.

A common approach is to avoid the formation of higher-order modes (HOMs) and harmful frequencies in resonant structures, mainly in the cavities used to accelerate the particles, which can give rise to coupled-bunch instabilities. This is done by redesigning the structures and adding, for example, frequency couplers, wave guides or ferrite antennas [15–18]. In another approach, active bunch-by-bunch feedback systems are utilized, which detect and counteract the coupled-bunch motion. Both approaches have their drawbacks. A proper design of highly resonant structures in respect to suppression of harmful frequencies is a very challenging and costly task, especially for superconducting structures. Digital bunch-by-bunch feedback systems, on the other hand, are commercially available nowadays and applicable to almost every machine. Nevertheless, these systems are expensive, the related kicker structures need space in the ring which is limited, and the vacuum needs to be broken to install them. Therefore, this option is not available for every facility. In addition, since feedback systems always need time to detect the particle motion before they can counteract them, they could become too slow for the ever rising coupled-bunch growth rates. Also, the damping strength of these systems is limited due to their kickers with low

quality factors and shunt impedances. The result is that bunch-by-bunch feedback systems may be both too slow and too weak for upcoming storage rings.

The work of this thesis focuses on an alternative approach of stabilizing an electron beam by modulating the phase of the RF field in the accelerating cavity, a technique that was studied in circular accelerators as early as in the 1990's [19–23], but is still not fully understood. The main goal of theses studies was related to the issues of lifetime limitations due to RF noise, the development of slow extraction techniques and the use of parametric feedback for multi-bunch instabilities [24]. RF phase modulation induces a frequency spread to the particle oscillation, leading to a suppression of resonant excitations. The advantages of this approach are a suppression of the excitation of coupled-bunch instabilities instead of reacting to existing instabilities and that an RF phase modulation system is rather low-priced and easily installed. On the other hand, introducing a frequency spread leads to additional intra-bunch motion, a deformation of the longitudinal bunch profile and an increased bunch length and energy spread. This requires a compromise between the beam quality increase due to the absence of coupled-bunch instabilities and the longitudinal beam quality decrease due to RF phase modulation effects. In order to get a deeper understanding of the interaction between RF phase modulation and the suppression of coupled-bunch instabilities, as well as the quantification of this interaction as a function of the modulation parameters, numerical studies have been performed in the framework of this thesis, in conjunction with experimental studies at the DELTA storage ring.

The 1.5 GeV electron storage ring DELTA, operated by the Center for Synchrotron Radiation [25] of the TU Dortmund University, serves as a synchrotron light source with several beam lines and as a research facility for accelerator physics. The first beam was injected in 1996 [26] and it is in continuous operation since 2000 [27]. This machine is also a good example for the development of curing coupled-bunch instabilities, since at DELTA, different approaches were made to characterize and suppress beam instabilities in order to increase the brilliance of the generated synchrotron radiation. In 2004, a cavity prototype, called EU cavity, with additional damping ports was installed to prevent the excitation of instabilities, which could be assigned to HOMs of the previously installed cavity [28–30]. Afterwards, the cavity-induced instabilities were not observable anymore, but other multi-bunch instabilities still persisted, which are presumably created by other resonant structures. The prototype was just temporarily installed and removed after one year of operation. It was replaced by the initial DORIS-type cavity, which was upgraded with ferrite-damping antennas [15]. With this setup, the same instabilities were suppressed as with the EU cavity, while the origin of the continuously existing instabilities is still unknown [31]. To get rid of these insta-

bilities, a remotely controllable RF phase modulation system was installed in 2008 [32]. It suppresses the occurrance of coupled-bunch effects at the cost of bunch lengthening and a deformation of the longitudinal phase space up to a point where each bunch splits up into two sub-bunches. In 2011, a digital bunch-by-bunch feedback system was installed, which is able to eliminate coupled-bunch instabilities without the aforementioned negative effects. Nonetheless, the RF phase modulation is still used during user operation, due to its positive side effect of increasing the beam lifetime by up to 20 % [33]. This effect is more important for the users than the longitudinal beam quality, since there are currently no time-resolved measurements at DELTA. Although, the scope of applicability of the bunch-by-bunch feedback system is thereby limited to being a diagnostic tool, the availability of both systems at the same machine grants the chance of analyzing coupled-bunch motion under the influence of RF phase modulation.

The intent of this work is to analyze and quantify the dependence of the suppression of coupled-bunch instabilities by RF phase modulation as a function of the modulation frequency and the modulation amplitude. In addition, the results of these studies shall be used to reevaluate RF phase modulation parameters applied at DELTA during user operation. For this purpose, an overview on particle acceleration, particle beam dynamics, longitudinal wake fields and coupled-bunch instabilities is given in Chapter 2. Due to the fact that the complex interaction between RF phase modulation and coupled-bunch instabilities cannot be calculated analytically, numerical studies with a particle tracking code, designed specifically for this thesis, are shown in Chapter 4. The results of these calculations are further investigated in detail by experimental studies performed at the DELTA storage ring in Chapter 3. The experiments, presented in Chapter 5, focus on analyzing the RF phase modulation system and its impact on the particles as well as the characterization of coupled-bunch instabilities by analyzing data from the bunch-by-bunch feedback system. Also, both systems are used in a combined measurement to analyze the interaction of both effects. Finally, additional studies are carried out to improve the user operation at DELTA.

2. Particle Beam Dynamics and Coupled-Bunch Instabilities

In this chapter, an overview of particle acceleration, particle dynamics and the principles of coupled-bunch instabilities together with their origin, i.e., wake fields and impedances, is given. The fundamental equations of motion are derived and the most important figures of merit are presented. This thesis focuses on longitudinal motion of ultrarelativistic particles in storage rings. In this setting, the particles travel with a constant velocity approximately at the speed of light c.

The first section introduces cylindrical waveguides and cavities for particle acceleration together with the option of using phase modulation of the electromagnetic wave to load the cavity for special applications.
Section 2.2 presents the coordinate system used in this thesis and touches the topic of longitudinal beam dynamics of a storage ring.
In Section 2.3, the beam spectra of bunched beams are derived as well as the wake fields and impedances of a storage ring. In addition, the formalism of a wake matrix is motivated which is used for the numerical calculations presented in Chapter 4.
The last section concentrates on the equations of longitudinal motion of particles under the influence of wake fields and other external excitations. The instability growth rate is deduced and synchrotron radiation and other damping mechanisms are described.

2.1. Particle acceleration

The effect of electromagnetic fields on a particle with charge q and velocity $\vec{v}$ are described by the Lorentz force

$$\vec{F}_{\mathrm{L}} = q\left(\vec{E} + \vec{v} \times \vec{B}\right)$$

with the electric field strength $\vec{E}$ and the magnetic flux density $\vec{B}$. Since the vector $\vec{v} \times \vec{B}$ is always perpendicular to the propagation direction of the particle, magnetic fields cannot change the energy of the particle, leaving electric fields as the only option for acceleration. For static electrical fields, the final beam energy is limited due to the fact that it is proportional to the maximum voltage that can be achieved, since the particles can only pass it once. The first approach to work around this problem is to use free electromagnetic (EM) waves to achieve much higher beam energies. The direction of propagation of a free EM wave is described by the Pointing vector

$$\vec{S} = \frac{1}{\mu_0} \vec{E} \times \vec{B}$$

with the vacuum permeability μ_0, which shows, that the electric field of free EM-waves is also always perpendicular to its propagation direction. In order to be able to accelerate with EM fields, additional boundary conditions have to be introduced to generate longitudinal electric fields.

2.1.1. Longitudinal Electric Fields in Cylindrical Waveguides

The first idea to generate additional boundary conditions is to use waveguides. Assuming the walls of a waveguide are perfectly conducting, the conditions

$$\vec{n} \times \vec{E} = 0 \quad \text{and} \quad \vec{n} \cdot \vec{B} = 0, \tag{2.1}$$

with the normal vector $\vec{n}$, which is perpendicular to the surface of the walls, must be satisfied, due to the Maxwell equations. The common approach in modern accelerators is to concentrate on cylindrical waveguides for several reasons, e.g., rotationally symmetric EM fields, better surface-to-volume ratio, etc.

The propagation of an EM wave inside a cylindrical evacuated waveguide is described by

the wave equation

$$\Delta\vec{E} - \frac{1}{c^2}\ddot{\vec{E}} = 0,$$

which derives from the Maxwell equations with the Laplace operator Δ. Separating the spatial distribution with the cylinder coordinates (r,θ,z) from the time dependence t with the frequency[1] ω

$$\vec{E}(r,\theta,z,t) = \vec{E}(r,\theta,z)e^{i\omega t}$$

leads to

$$\Delta\vec{E}(r,\theta,z) + k^2\vec{E}(r,\theta,z) = 0 \tag{2.2}$$

with the wave number $k = \omega/c$. Since this chapter focuses on the longitudinal electric field E_z, only the z-component of the field is considered and Eq. (2.2) is reduced to the Helmholtz equation

$$\frac{\partial^2}{\partial_r^2}E_z + \frac{\partial^2}{\partial_\theta^2}E_z + \frac{\partial^2}{\partial_z^2}E_z = -k^2E_z. \tag{2.3}$$

Using the relations $k^2 = k_r^2 + k_\theta^2 + k_z^2$ and $k_c^2 = k_r^2 + k_\theta^2$, Eq. (2.3) can be simplified to [34]

$$\frac{\partial^2}{\partial_z^2}E_z + k_z^2E_z = 0$$

with the solution

$$E_z = \hat{E}e^{ik_zz}.$$

If k_z is complex, the amplitude of a wave traveling through the waveguide decreases exponentially, while it is constant if k_z is real. Therefore, it is possible to define two regimes

$$k_z = \begin{cases} \text{complex} & \text{if} \quad k_c^2 > k^2 \quad \text{(damping)} \\ \text{real} & \text{if} \quad k_c^2 < k^2 \quad \text{(loss-free propagation)} \end{cases}$$

divided by the cutoff wave number k_c [34].

Assuming a cylindrical waveguide with radius R is perfectly conducting, no tangential electric fields can exist at the walls. Solving the eigenvalue problem for this geometry with the boundary condition $E_z(r = R) = 0$ leads to discrete solutions [35]

$$k_c = \frac{X_{mn}}{R} \tag{2.4}$$

[1] In this thesis, f denotes the frequency in terms of cycles per time unit, whereas $\omega = 2\pi f$ marks the angular frequency, i.e., the phase angle per time unit. For simplicity, the word "frequency" is used for both.

with the n-th zero of the m-th Bessel function X_{mn}. Inserting Eq. (2.4) into the dispersion relation $\omega = k \cdot c$ results in

$$\omega = c\sqrt{\left(\frac{X_{mn}}{R}\right)^2 + k_z^2}$$

with the group and phase velocity [36]

$$v_{gr} = \frac{d\omega}{dk_z} = c\frac{k_z}{\sqrt{\left(\frac{X_{mn}}{R}\right)^2 + k_z^2}} < c$$

$$\text{and} \quad v_{ph} = \frac{\omega}{k_z} = c\sqrt{\left(\frac{X_{mn}}{R}\right)^2 \frac{1}{k_z^2} + 1} > c.$$

The fact that the phase velocity is always higher than the speed of light makes accelerating particles with waveguides impossible, since the particles dephase with the accelerating electrical field. While longitudinal electrical fields can be achieved with waveguides, additional boundary conditions are necessary to stabilize the phase.

2.1.2. Cylindrical Resonators

In modern accelerators, additional boundary conditions to lower the phase velocity are introduced by using resonant cavities. In principle, these resonators are waveguides with their entrances and exits closed off by conducting walls at the distance l. Because of the boundary conditions of Eq. (2.1), an electromagnetic wave propagating into the cavity reflects at both ends resulting in a standing wave with the discrete frequencies [34]

$$\omega_{mnp} = c\sqrt{\left(\frac{X_{mn}}{R}\right)^2 + \left(\frac{p\pi}{l}\right)^2} \quad \text{with} \quad p = 0,1,2,3,... \tag{2.5}$$

Standing waves only exist if the resonance condition of Eq. (2.5) is satisfied, thus the cavity behaves like an electrical oscillator with the quality factor

$$Q_0 = \frac{\omega_{res}}{\Delta\omega} \tag{2.6}$$

where ω_{res} is the resonance frequency and $\Delta\omega$ is the bandwidth between the two points at which the amplitude is reduced by -3 dB relative to its maximum.

This means, that the cavity can only be loaded by an electromagnetic wave with a frequency that matches the resonance frequency of the cavity. Additionally, the power transfer de-

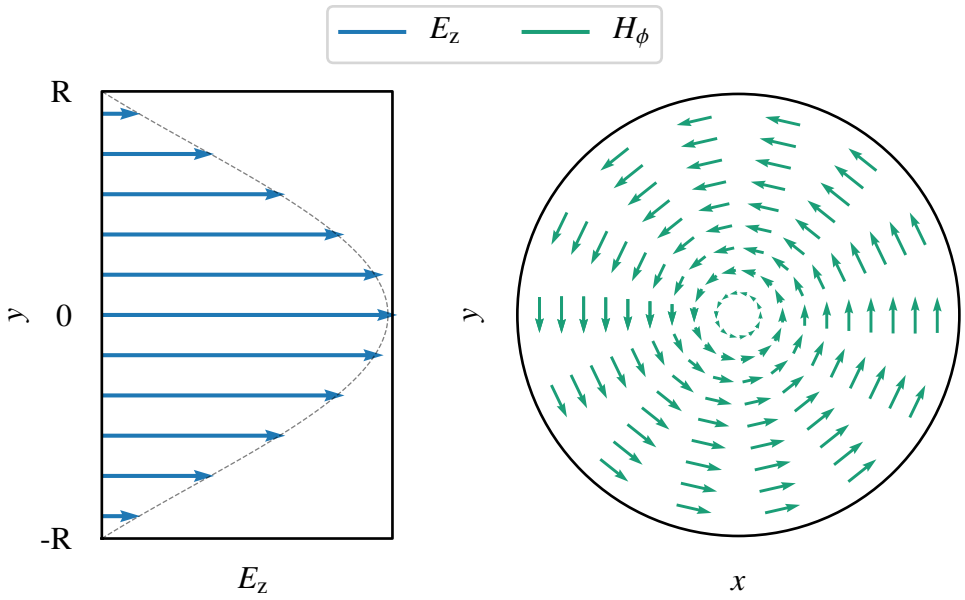

Figure 2.1.: Field distribution in a pillbox-cavity with radius R. **Left:** Longitudinal electrical field E_z as a function of the radius r, which is mainly determined by the Bessel function $\mathcal{J}_0$ (shown by a dashed line). **Right:** Cross section of the cavity. The magnetic field H_ϕ circles around the center. At the beam position ($r = 0$), no magnetic field is present.

pends on the coupling hardware used to load the cavity, which is characterized by the coupling factor κ [6]. This leads to a loaded quality factor

$$Q_L = \frac{Q_0}{1+\kappa}, \tag{2.7}$$

which is generally lower than Q_0.

Another important figure of merit for cavities is the shunt impedance

$$R_s = \frac{|U_{\text{eff}}|^2}{2P} \tag{2.8}$$

which describes the efficiency of producing an effective axial voltage U_{eff} for a given dissipated power P [36]. For a comparison of cavities, the parameter R_s/Q_0 is often used which is independent of material properties and, therefore, gives information about the power efficiency of the cavity geometry [35].

The boundary conditions imposed on the electric and magnetic fields imply that the solutions of Eq. (2.3) form two categories of modes with different eigenvalues. On the one hand, there are transverse magnetic, so-called TM-modes, with longitudinal electric and

transverse magnetic fields. On the other hand, there are transverse electric TE-modes with $E_z = 0$, where the magnetic fields are completely transverse [35]. To accelerate particles, a strong electric field at the beam position ($r = 0$) is desired, that is only given for TM-modes, which are classified by the nomenclature TM_{mnp}. The indices m, n and p are the same as in Eq. (2.5) and represent the number of nodes in the longitudinal, radial and azimuthal plane. The most important mode is the TM_{010}-fundamental mode, which has the highest R_s/Q_0 value. Its electric and magnetic field are shown in Fig. 2.1 and described by

$$E_z = \hat{E}\mathscr{J}_0\left(\frac{X_{01}r}{R}\right)e^{i\omega t} \qquad\qquad B_\theta = -i\frac{\hat{E}}{c}\mathscr{J}_1\left(\frac{X_{01}r}{R}\right)e^{i\omega t}$$

with the first two Bessel functions of the first kind $\mathscr{J}_0$ and $\mathscr{J}_1$.

2.1.3. RF Phase Modulation

The electric fields in a cavity generate a voltage on the beam axis, which usually has the form

$$U(t) = \hat{U}\sin\left(\omega_{RF}t + \phi\right),$$

with the amplitude $\hat{U}$, the frequency ω_{RF} given by the master RF generator and the phase shift ϕ. By applying a time-dependent sinusoidal phase modulation, given by the expression

$$\phi(t) = \eta\sin\left(\omega_{mod}t\right) + \phi_0,$$

with the modulation frequency ω_{mod} and the modulation index η describing the maximum phase shift, the frequency spectrum is fully described by [37]

$$S(\omega) = \pi\hat{U}\sum_{n=-\infty}^{\infty}\mathscr{J}_n(\eta)e^{in\frac{\pi}{2}}\delta(\omega-\omega_{RF}-n\omega_{mod}) \tag{2.9}$$

as shown in Fig. 2.2. In addition to the center frequency ω_{RF}, an infinite number of sidebands occur at

$$\omega_{RF} \pm n\cdot\omega_{mod} \quad \text{with} \quad n = 1,2,3,...$$

with their spectral amplitudes weighted by the Bessel function $\mathscr{J}_n(\eta)$.

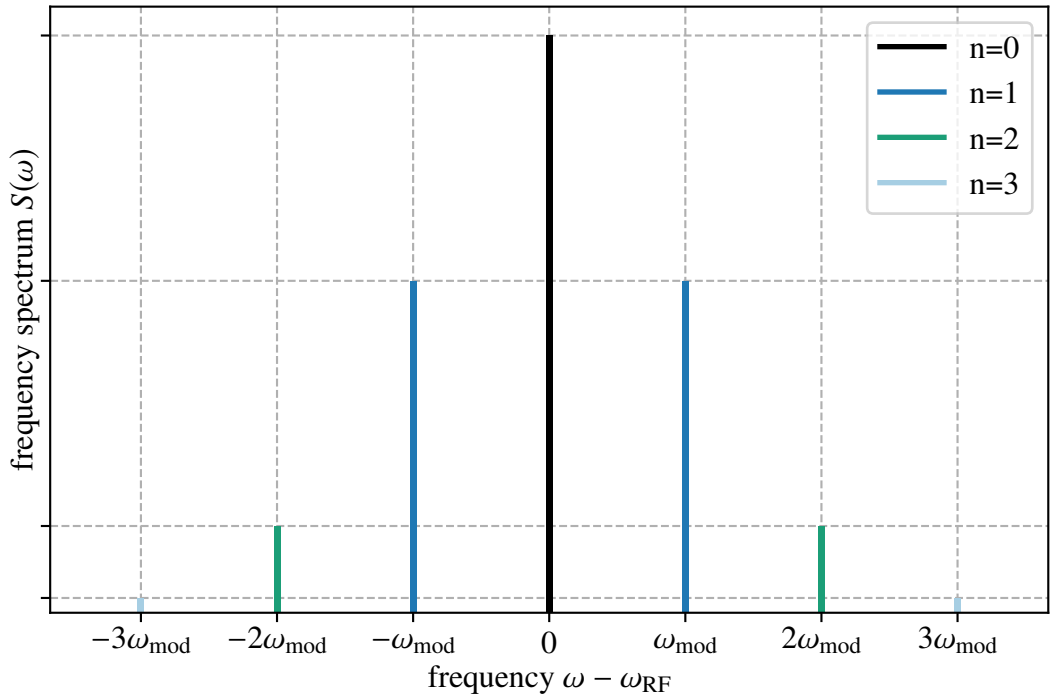

Figure 2.2.: Spectrum of a phase-modulated signal with the modulation frequency ω_{mod} around the center frequency ω_{RF}. Sidebands with $n > 3$ are approximated to be zero.

2.2. Basic Particle Dynamics

The dynamics of particles traveling through a storage ring are mainly defined by interaction with the applied magnetic fields and the accelerating electric field in the cavity. To describe these effects for a specific particle or a bunch of particles, a moving coordinate system is introduced. The velocity of the particles is considered to match the speed of light $v \approx c$, so that relativistic effects have to be taken into account at all times. This results in an oscillation of the particles around their reference position in all three spatial directions, which can be examined separately.

2.2.1. Frenet-Serret Coordinates

To describe the particle motion in a storage ring, a moving coordinate system [6] is used. A particle at the center of the coordinate system, with $x = y = z = 0$, is called reference particle. The path of the reference particle around the ring defines the s-axis and is called orbit.

The Frenet-Serret coordinates build an orthogonal coordinate system following the orbit as shown in Fig. 2.3. The displacements of other particles relative to the reference particle are expressed by the x, y and z coordinates for the horizontal, vertical and longitudinal direction, respectively. In addition, the transverse angles of a particle relative to the orbit are described by $x' = dx/ds$ and $y' = dy/ds$. The coordinate $\delta = \Delta E/E_0$ represents the relative energy deviation from the nominal energy E_0 of the reference particle. Eventually, this leads to a six-dimensional phase space

$$\begin{pmatrix} x \\ x' \\ y \\ y' \\ z \\ \delta \end{pmatrix} = \begin{pmatrix} \text{horizontal displacement} \\ \text{horizontal angle} \\ \text{vertical displacement} \\ \text{vertical angle} \\ \text{longitudinal displacement} \\ \text{relative energy deviation} \end{pmatrix}.$$

2.2.2. Momentum Compaction Factor

Due to the Lorentz force in the presence of magnetic fields, a reference particle with elementary charge e traveling approximately at the speed of light experiences a horizontal acceleration described by

$$\ddot{\vec{x}} = \frac{ec^3 B}{E_0}\vec{e}_x,$$

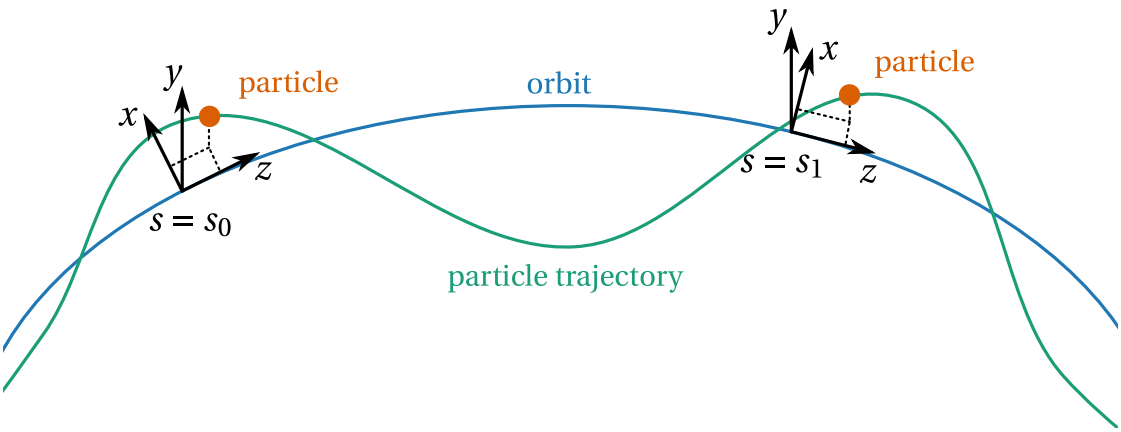

Figure 2.3.: Frenet-Serret coordinates moving along the orbit with the coordinate s. A particle travels along its trajectory with the longitudinal displacement z and the transverse displacements x and y.

depending only on the particle energy E_0 and the magnetic flux density B, which is perpendicular to the particle motion. That leads to an energy-dependent horizontal displacement which is represented by the so-called dispersion function $D(s)$ [6, 34]. Considering that the bending radius of the dipoles $R_\mathrm{b}(s)$ also depends on the position s along the orbit, the length deviation of the trajectory of a particle with $\delta \neq 0$ becomes

$$\Delta L = \delta \oint \frac{D(s)}{R_\mathrm{b}(s)} ds.$$

This means, that the path length of a particle depends on the particles energy and the so-called momentum compaction factor for ultrarelativistic particles

$$\alpha = \frac{d}{d\delta} \frac{\Delta L}{L_0}$$

is defined as the derivation of the normalized path length deviation $\Delta L / L_0$ with the circumference of the ring L_0.

For small energy deviations, it can be shown [34], that the momentum compaction factor can be simplified to

$$\alpha = \frac{\Delta L / L_0}{\delta} = \frac{\Delta T / T_\mathrm{rev}}{\delta} \tag{2.10}$$

with the time deviation ΔT corresponding to ΔL and the revolution time T_rev.

2.2.3. Linear Transverse One-Particle Motion

A single electron traveling through the magnetic structure of a storage ring where all dipoles only influence the horizontal motion experiences linear reversing forces in the quadrupoles with the strength $k(s)$ [34] and performs quasi-harmonic oscillations around the orbit in both transverse planes. Additionally, the bending radius $R_\mathrm{b}(s)$ influences the horizontal motion resulting in the linear equations of motion [6]

$$x''(s) + \left(\frac{1}{R_\mathrm{b}^2(s)} - k(s) \right) x(s) = \frac{\delta}{R_\mathrm{b}(s)} \qquad\qquad y''(s) + k(s)\, y(s) = 0.$$

The trajectory of the particle can be plotted in the transverse phase space, as shown in Fig. 2.4 for the horizontal plane.

The transverse beam cross section is limited by the acceptance, which is defined by the two following effects. The mechanic aperture is given by the vacuum chamber or any obstacle

close to the beam and the dynamic apertureis an effect of non-linear particle dynamics, which further narrows the acceptance (for more details see e.g. [6, 34, 38]). The combination results in the acceptance ellipse shown in Fig. 2.4, which is the largest possible ellipse for stable trajectories in the transverse phase space. All particles with a displacement or angle outside the acceptance ellipse inevitably hit an obstacle resulting in the loss of the particle.

2.2.4. Longitudinal One-Particle Motion and Phase Focusing

Similar to 2.2.3, a single particle performs oscillations around the longitudinal reference position ($z = 0$) as well. The restoring force in this case originates from the accelerating field in the cavity introduced in Section 2.1.1.

An electron traveling at $v \approx c$ around the ring loses the energy ΔE_s due to the emission of synchrotron radiation. The RF voltage in the accelerating cavity applies the energy change ΔE_{RF} depending on the phase at which the particle passes cavity. At the synchronous phase

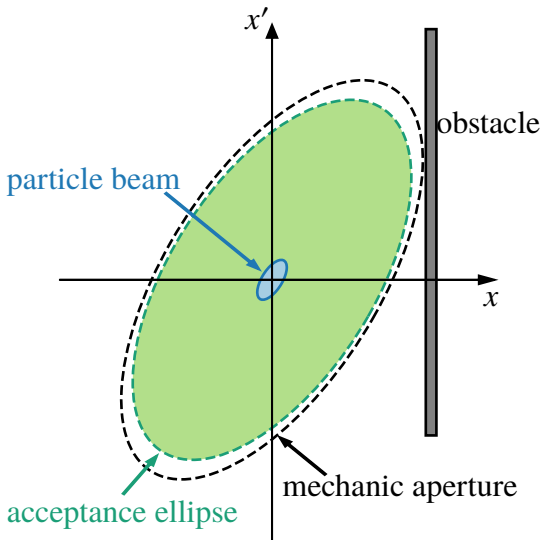

Figure 2.4.: Horizontal phase space of a particle beam in a recirculating accelerator. The particles follow elliptical trajectories forming the area of the beam shown in blue. The mechanic aperture (dashed black) is defined by the obstacle closest to the beam (grey). The acceptance ellipse (green) is further narrowed by non-linear effects (dynamic aperture) and describes the largest possible ellipse for stable trajectories in the transverse phase space (the figure is based on [34]).

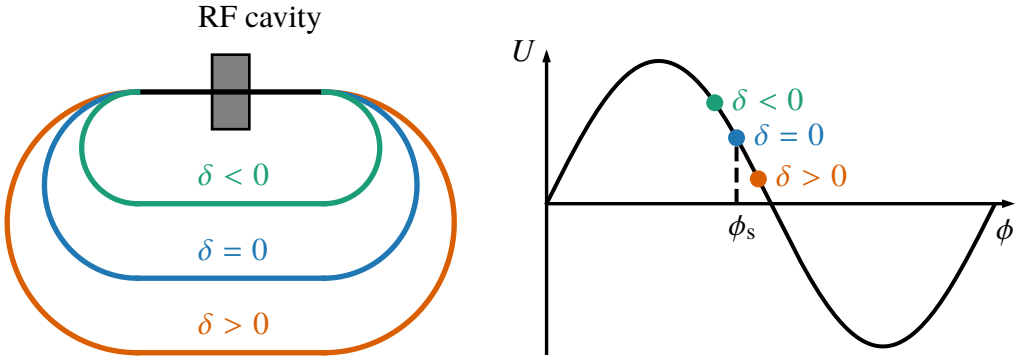

Figure 2.5.: **Left:** Different path length due to energy deviation δ. **Right:** Phase focusing inside the accelerating RF cavity with synchronous phase ϕ_s at $\delta = 0$ (the figure is based on [34]).

ϕ_s, the energy gain in the cavity

$$\Delta E_{RF} = e\hat{U} \sin\left(\phi_s\right) \tag{2.11}$$

and the energy loss due to synchrotron radiation ΔE_s perfectly compensate each other. To ensure this over multiple turns, the RF frequency ω_{RF} must be an integer multiple of the revolution frequency ω_{rev}

$$\omega_{RF} = h \cdot \omega_{rev} \tag{2.12}$$

with the harmonic number h.

For $\alpha > 0$, an ultrarelativistic particle with less energy than the reference particle $\delta_1 < 0$ travels a shorter path through the storage ring, as described by Eq. (2.10) and illustrated in Fig. 2.5. Hence, it will enter the cavity earlier and with a smaller phase $\phi_1 < \phi_s$ than the reference particle which leads to a higher energy gain, as long as $\pi/2 < \phi_s < \pi$ is given. As a result, the absolute value $|\delta_1|$ decreases and the particle catches up with the nominal phase. The opposite happens to a particle with more energy than the reference particle. The particles oscillate around ϕ_s, which is called synchrotron oscillation. Below, the equation of motion of this oscillation is derived for small deviations around the synchronous phase $\Delta\phi$.

The energy change of a particle with charge e in one turn due to radiative energy loss ΔE_s and energy gain in the cavity ΔE_{RF} is

$$E - E_0 = \underbrace{e\hat{U} \sin\left(\phi_s + \Delta\phi\right)}_{\Delta E_{RF}} - \Delta E_s. \tag{2.13}$$

By rearranging Eq. (2.10) to

$$\Delta T = \alpha T_{\mathrm{rev}} \delta$$

and using the RF period $T_{\mathrm{RF}} = T_{\mathrm{rev}}/h$ and

$$\Delta\phi = 2\pi \frac{\Delta T}{T_{\mathrm{RF}}} = \omega_{\mathrm{RF}} \Delta T,$$

the change of the RF phase in the same turn is

$$\Delta\phi = \omega_{\mathrm{RF}} \alpha T_{\mathrm{rev}} \delta. \tag{2.14}$$

Since the synchrotron oscillation period is long compared to the revolution period, a first-order approximation is sufficient, meaning that the phase difference $\Delta\phi$ changes linearly between two revolutions. Thus, the time derivative can be simplified by dividing by T_{rev}, which leads to

$$\Delta\dot{\phi}(t) = \omega_{\mathrm{RF}} \alpha \frac{\Delta E(t)}{E_0}. \tag{2.15}$$

The same assumption is valid for ΔE giving

$$\Delta\dot{E}(t) = \frac{e\hat{U}}{T_{\mathrm{rev}}} \sin\left(\phi_{\mathrm{s}} + \Delta\phi(t)\right) - \frac{\Delta E_{\mathrm{s}}}{T_{\mathrm{rev}}},$$

where the sine function can be approximated for small phase shifts $\Delta\phi << \phi_{\mathrm{s}}$ to

$$\sin\left(\phi_{\mathrm{s}} + \Delta\phi(t)\right) \approx \sin\left(\phi_{\mathrm{s}}\right) + \Delta\phi(t) \cos\left(\phi_{\mathrm{s}}\right).$$

The time derivation of $\Delta\dot{E}$ is therefore

$$\Delta\ddot{E}(t) = \frac{e\hat{U}}{T_{\mathrm{rev}}} \Delta\dot{\phi}(t) \cos\left(\phi_{\mathrm{s}}\right) \tag{2.16}$$

and inserting Eq. (2.15) results in

$$\Delta\ddot{E}(t) = \frac{e\hat{U}\omega_{\mathrm{RF}}\alpha}{T_{\mathrm{rev}}E_0} \cos\left(\phi_{\mathrm{s}}\right) \Delta E(t), \tag{2.17}$$

which describes a harmonic oscillator with the so-called synchrotron frequency

$$\omega_{\mathrm{s}} = \sqrt{\frac{e\hat{U}\omega_{\mathrm{RF}}\alpha}{T_{\mathrm{rev}}E_0} \cos\left(\phi_{\mathrm{s}}\right)}. \tag{2.18}$$

In the previous sections, the phase oscillation or, equivalently, the energy oscillation was only calculated for sufficiently small amplitudes. In this regime, the RF voltage can be approximated to be linear due to the linearity of the sine function for small phase deviations $\Delta\phi$. However, for large amplitudes, the particles behave non-linearly due to the sinusoidal shape of the RF voltage. For very large amplitudes they may even escape from the stable region of the RF potential leading to particle losses. The separatrix defines the boundary between the stable and unstable regions in the longitudinal phase space via the separatrix equation for $\alpha > 0$ [34]

$$\Delta E = \pm\sqrt{-\frac{e\hat{U}E_0}{\pi h\alpha}\left[\cos\left(\phi_\mathrm{s}+\Delta\phi\right)+\cos\left(\phi_\mathrm{s}\right)+\left(2\phi_\mathrm{s}+\Delta\phi-\pi\right)\sin\left(\phi_\mathrm{s}\right)\right]} \tag{2.19}$$

with the constraint for the synchronous phase $\pi/2 < \phi_\mathrm{s} < 3\pi/2$ and the momentum compaction factor being $\alpha > 0$. The longitudinal phase space is plotted in Fig. 2.6 and shows a series of stable regions in the RF potential with a phase separation of 2π. All particles outside these regions are lost, while the particles inside undergo synchrotron oscillations with stable trajectories. A storage ring has h such regions where electrons can be stored, which are also called RF buckets.

Due to several effects, like particle collisions with residual gas atoms, intra bunch scattering or occasional large energy losses through synchrotron radiation, particles leave the separatrix (longitudinal) or the acceptance (transverse) and the beam current becomes a function of time

$$I(t) = I_0 \exp\left\{-\frac{t}{\tau_\mathrm{b}(t)}\right\}$$

with the beam lifetime $\tau_\mathrm{b}(t)$.

2.2.5. RF Phase Modulation

The potential generated by the accelerating RF, in which the particles oscillate with the synchrotron frequency ω_s, can be described by the Hamiltonian formalism. Considering RF phase modulation, the Hamiltonian

$$\begin{aligned} H\left(\delta,\phi,t\right) = {} & \frac{\omega_\mathrm{s}\delta^2}{2} + \omega_\mathrm{s}\tan\overline{\phi}_\mathrm{s}\left[\sin\phi\cos\left(A_\mathrm{m}\sin\left(\omega_\mathrm{mod}t\right)\right)+\cos\phi\sin\left(A_\mathrm{m}\sin\left(\omega_\mathrm{mod}t\right)\right)\right] \\ & -\omega_\mathrm{s}\cos\phi\cos\left(A_\mathrm{m}\sin\left(\omega_\mathrm{mod}t\right)\right)+\omega_\mathrm{s}\sin\phi\sin\left(A_\mathrm{m}\sin\left(\omega_\mathrm{mod}t\right)\right)-\omega_\mathrm{s}\tan\overline{\phi}_\mathrm{s} \end{aligned}$$

is derived, as done in [21, 24, 39–41], with $\overline{\phi}_\mathrm{s} = \pi - \phi_\mathrm{s}$ and the modulation amplitude A_m.

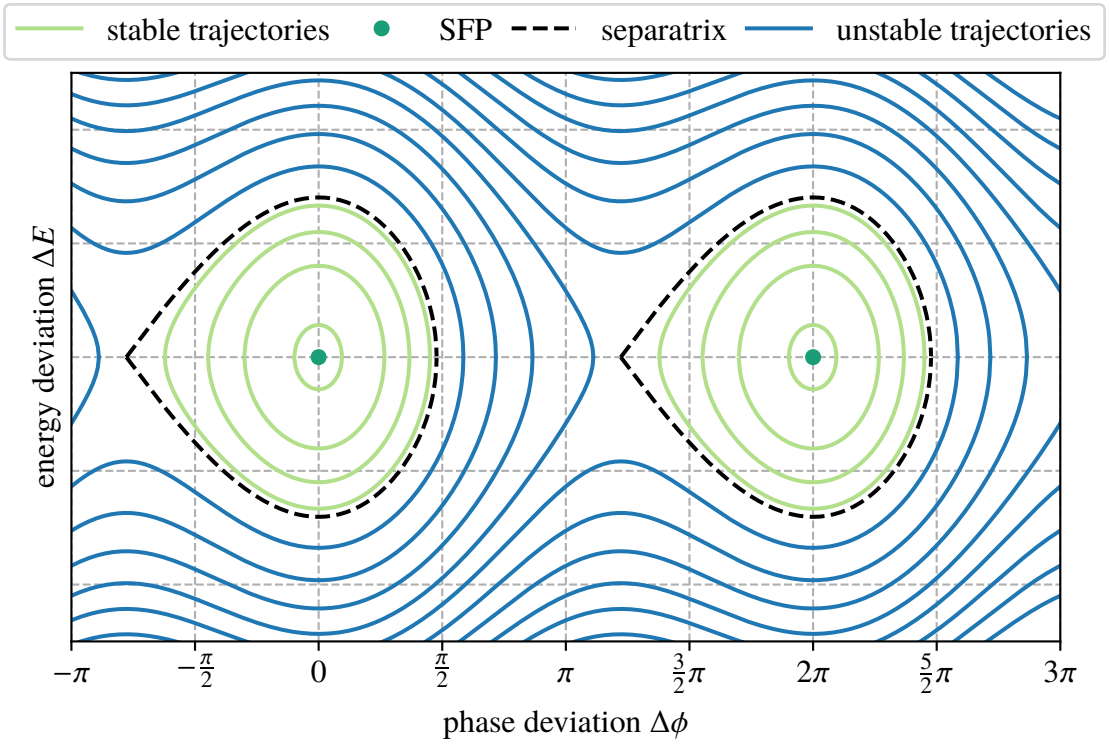

Figure 2.6.: Particle motion in an accelerating RF field at a synchronous phase $\phi_s = 20\,\text{deg}$. The separatrix (dashed black) represents the phase space contour separating the stable trajectories (green), in which particles perform synchrotron oscillations around the stable fix points (SFP), from the unstable regions (blue).

To be able to calculate the stable and unstable fix points in the phase-modulated RF potential, the time-averaged Hamiltonian K

$$\langle K \rangle_t = \left(\omega_s - \frac{\omega_{mod}}{2}\right) J - \frac{\omega_s J^2}{16} + \frac{\omega_s \epsilon J}{4} \cos\left(2\psi\right)$$

where $\epsilon = A_m \tan\overline{\phi}_s$ is derived for the second integer harmonic with $\omega_{mod} = 2{\cdot}\omega_s$ (the reason for this specialization is discussed later in this thesis). For this purpose, the transformation

$$\delta = -\sqrt{2J}\sin\left(\psi + \omega_{mod}\, t/2 + \pi/4\right)$$
$$\phi = \sqrt{2J}\cos\left(\psi + \omega_{mod}\, t/2 + \pi/4\right)$$

is used to achieve the action-angle coordinates (J,ψ), which describe the trajectories of the particles in the phase space near the second-harmonic resonance in a reference frame which rotates at half of the modulation frequency [24].

While the potential without RF phase modulation has only one stable fix point (SFP) and

no unstable fix points (UFP) in each bucket, as seen in Fig. 2.6, the fix points of the system with RF phase modulation at the second integer harmonic are the solutions of

$$\frac{dJ}{dt} = -\frac{\partial K}{\partial t} = 0 \quad \text{and} \quad \frac{d\psi}{dt} = \frac{\partial K}{\partial J} = 0.$$

The fix points are given by

$$J_{\mathrm{SFP}} = \begin{cases} 8\left(1 - \frac{\omega_{\mathrm{mod}}}{2\omega_{\mathrm{s}}}\right) + 2\epsilon, & \omega_{\mathrm{mod}} \leq (2+\epsilon/2)\,\omega_{\mathrm{s}} \\ 0, & \omega_{\mathrm{mod}} > (2+\epsilon/2)\,\omega_{\mathrm{s}} \end{cases}$$

$$J_{\mathrm{UFP}} = \begin{cases} 8\left(1 - \frac{\omega_{\mathrm{mod}}}{2\omega_{\mathrm{s}}}\right) - 2\epsilon, & \omega_{\mathrm{mod}} \leq (2-\epsilon/2)\,\omega_{\mathrm{s}} \\ 0, & \omega_{\mathrm{mod}} > (2-\epsilon/2)\,\omega_{\mathrm{s}} \end{cases}$$

corresponding to the angles $\psi_{\mathrm{SFP}} = 0,\ \pi$ and $\psi_{\mathrm{UFP}} = \pi/2,\ 3/2\pi$. This means, that for $\omega_{\mathrm{mod}} > (2+\epsilon/2)\,\omega_{\mathrm{s}}$ only one stable fix point exists. For $\omega_{\mathrm{mod}} \leq (2+\epsilon/2)\,\omega_{\mathrm{s}}$, three stable and

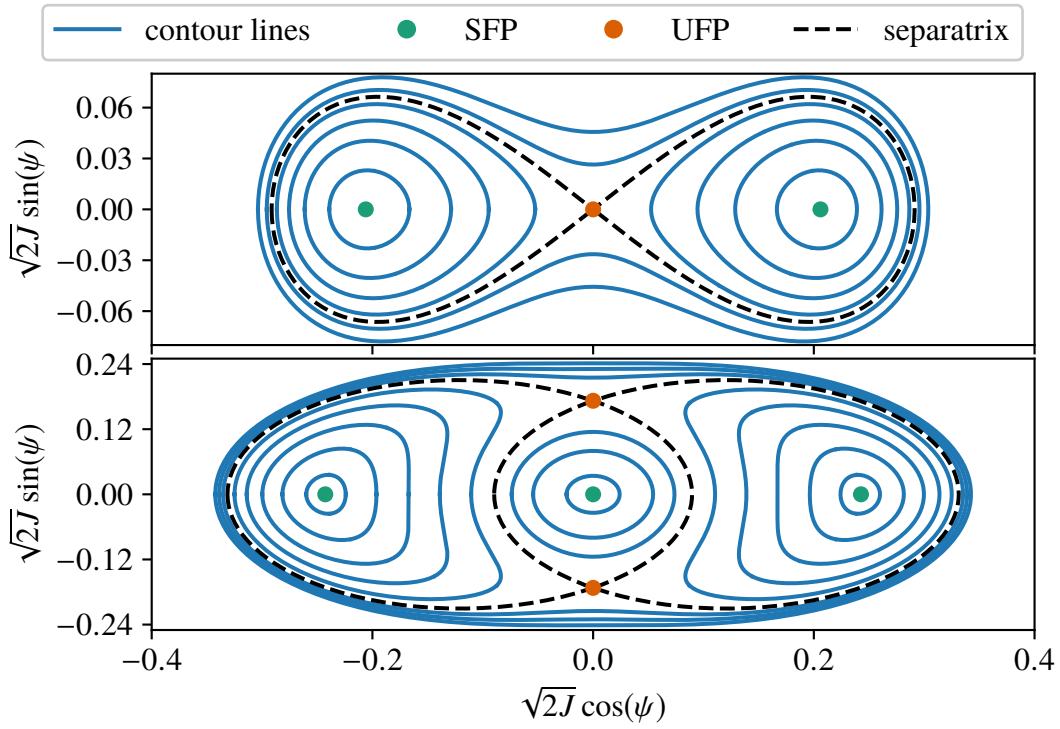

Figure 2.7.: Constant-energy contour lines (blue) in the longitudinal phase space in the regime of two stable islands (top) and three stable islands (bottom). The stable fix points (SFP) are marked with green dots and the unstable fix points (UFP) are shown by orange dots. The island-separatrix of each stable fix point is highlighted by a dashed black line.

two unstable fix points can be found and in the regime $(2+\epsilon/2)\,\omega_s < \omega_{mod} \leq (2+\epsilon/2)\,\omega_s$ two stable fix points exist together with one unstable fix point [24, 41]. The phase spaces for two and three stable fix points, which are also called islands because of their appearance in the phase space, are shown in Fig. 2.7. Two or even three sub-bunches can be present inside one RF bucket at the same time. The particles oscillate around a stable fix point with a revolution frequency $\omega_{SR}(\hat{\phi})$ depending on their phase amplitude $(\hat{\phi})$ with respect to that point [24]. The contours separating the different regimes depend on the modulation amplitude A_m and modulation frequency f_{mod} and are called bifurcation edges.

Taking the energy loss due to synchrotron radiation into account, the modulation ampli-

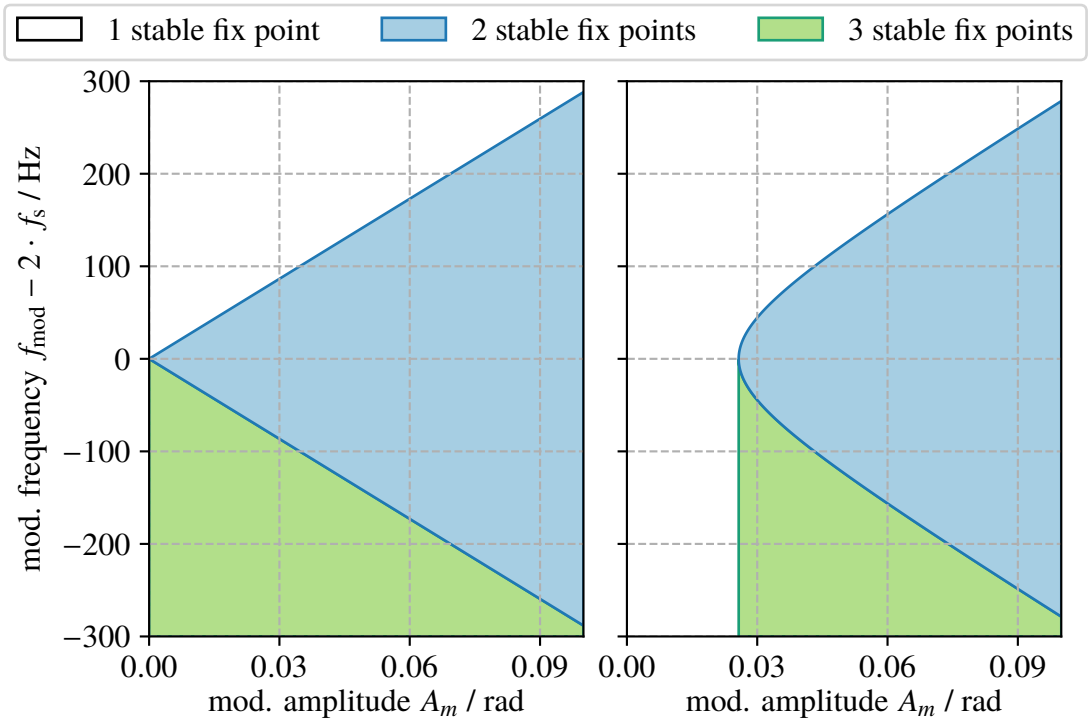

Figure 2.8.: Island formation in the longitudinal phase space as a function of the modulation amplitude A_m and modulation frequency f_{mod}. Left: Without emission of synchrotron radiation, two bifurcation edges distinguish the regime where two SFPs exist in the longitudinal phase space (blue) from the regime where only one SFP is present (white) and the regime where three SFPs occur (green). Right: The emission of synchrotron radiation deforms the bifurcation edges and shifts the regime of two SFPs to higher amplitudes. This shift adds a threshold for the modulation amplitude below which no island formation is observed (the figure is based on [41]).

tude changes to [24]

$$A_{\mathrm{m,eff}} = \sqrt{A_{\mathrm{m}}^2 - \left(\frac{4\gamma_{\mathrm{d}}}{\left|\tan\phi_{\mathrm{s}}\right|\omega_{\mathrm{s}}}\right)^2}$$

with the radiation damping time γ_{d}. This effect deforms the bifurcation edges and shifts the regime of two stable fix points to higher modulation amplitudes, as shown in Fig. 2.8. Additionally, this adds a threshold for the modulation amplitude. If A_{m} is below the threshold, no island formation is observed in the phase space.

2.3. Longitudinal Wake Fields and Impedances

When a charged relativistic particle moves through free space, it carries an electromagnetic field, which is Lorentz contracted into a thin disk, perpendicular to the motion of the particle. Placing the particle in a perfectly conducting vacuum chamber, all electric field lines terminate transversely on surface charges inside the wall of the chamber inducing a mirror current traveling synchronously with the particle. If the vacuum chamber has a finite resistivity or if it is not perfectly smooth, the mirror current falls behind or is scattered at the edge of a discontinuity. This leads to electromagnetic fields remaining in the vacuum chamber induced by the particle, which can influence other particles passing them. Since the particles travel close to the speed of light, there can be no field ahead of the particle generating it, which is why they are called wake fields [42].

If the frequency of the wake field matches one of the eigenfrequencies of the beam, the wake field is able to resonantly excite the beam giving rise to instabilities. To describe this phenomenon, the frequency spectrum of a bunched beam as well as the spectrum of potentially occurring wake fields are derived below. Afterwards, the equations of motion of a wake field inside a resonant structure are deduced.

2.3.1. The Beam Spectrum

The beam spectrum, i.e., the signal of the beam as a function of frequency, is deduced by a Fourier transform of the the beam current in the form

$$J(\omega) = \int_{-\infty}^{\infty} j\,(t)\, e^{i\omega t}\, dt,$$

with the corresponding inverse Fourier transform

$$j(t) = \frac{1}{2\pi} \int_{-\infty}^{\infty} J(\omega) e^{-i\omega t} d\omega$$

resulting in the current as a function of time, measured at a fixed position of the ring.

A pointlike charge traveling through a circular accelerator has a current distribution

$$j(t) = \sum_{n=-\infty}^{\infty} \delta(t - nT_{\mathrm{rev}}) \quad \text{with} \quad n \in \mathbb{Z}$$

described by a Dirac comb with equidistant peaks at multiples of the revolution time T_{rev}, where $\delta(t)$ means the Dirac delta function [43]. The Fourier transform of a Dirac comb results also in a Dirac comb. In this case, this results in equidistant peaks in the frequency spectrum at multiples of the revolution frequency ω_{rev} (see [4, 44] for details).

In reality, the bunches are not pointlike but can be approximated by a Gaussian shape with the standard deviation σ_{T} leading to a convolution of a Gaussian function with the Dirac comb in the time domain

$$j(t) = \frac{1}{\sqrt{2\pi\sigma_{\mathrm{T}}^2}} \sum_{n=-\infty}^{\infty} \int_{\infty}^{\infty} \delta(t' - nT_{\mathrm{rev}}) \exp\left\{-\frac{(t-t')^2}{2\sigma_{\mathrm{T}}^2}\right\} dt'.$$

According to the convolution theorem [45], Fourier-transforming a convolution of two functions results in a multiplication of these functions in the frequency domain leading to

$$J(\omega) = \omega_{\mathrm{rev}} \exp\left\{-\omega^2 \sigma_{\mathrm{T}}^2/2\right\} \sum_{n=-\infty}^{\infty} \delta(\omega - n\omega_{\mathrm{rev}})$$

where peaks at higher frequencies are suppressed, as shown in Fig. 2.9.

Assuming storage rings are filled with h bunches at multiples of the RF time T_{RF} with slightly different bunch charges. The non-uniform filling leads to spurious peaks in the spectrum at multiples of ω_{rev} in addition to the peaks at multiples of ω_{RF} as shown in Fig. 2.9.

Taking the longitudinal synchrotron motion of the bunches into account, the Dirac comb in the time domain

$$j(t) = \sum_{n=-\infty}^{\infty} \delta\left(t - nT_{\mathrm{rev}} - \eta \cos\left(\omega_{\mathrm{s}} nT_{\mathrm{rev}}\right)\right)$$

is phase modulated with the synchrotron frequency ω_{s}. Similar to Section 2.1.3, this leads

to sidebands in the spectrum determined by the n-th Bessel function $\mathscr{J}_\eta$. For a Dirac comb, these sidebands increase linearly with the frequency [4] resulting in a spectrum

$$J(\omega) = \omega_{\mathrm{rev}} \sum_{n=-\infty}^{\infty} \sum_{p=-\infty}^{\infty} i^{-p} \mathscr{J}_n\left(\eta\left[n\omega_{\mathrm{rev}} + p\omega_{\mathrm{s}}\right]\right) \delta\left(\omega - n\omega_{\mathrm{rev}} - p\omega_{\mathrm{s}}\right)$$

illustrated in Fig. 2.9.

In a storage ring, the bunches are a system of h coupled oscillators due to wake fields. This

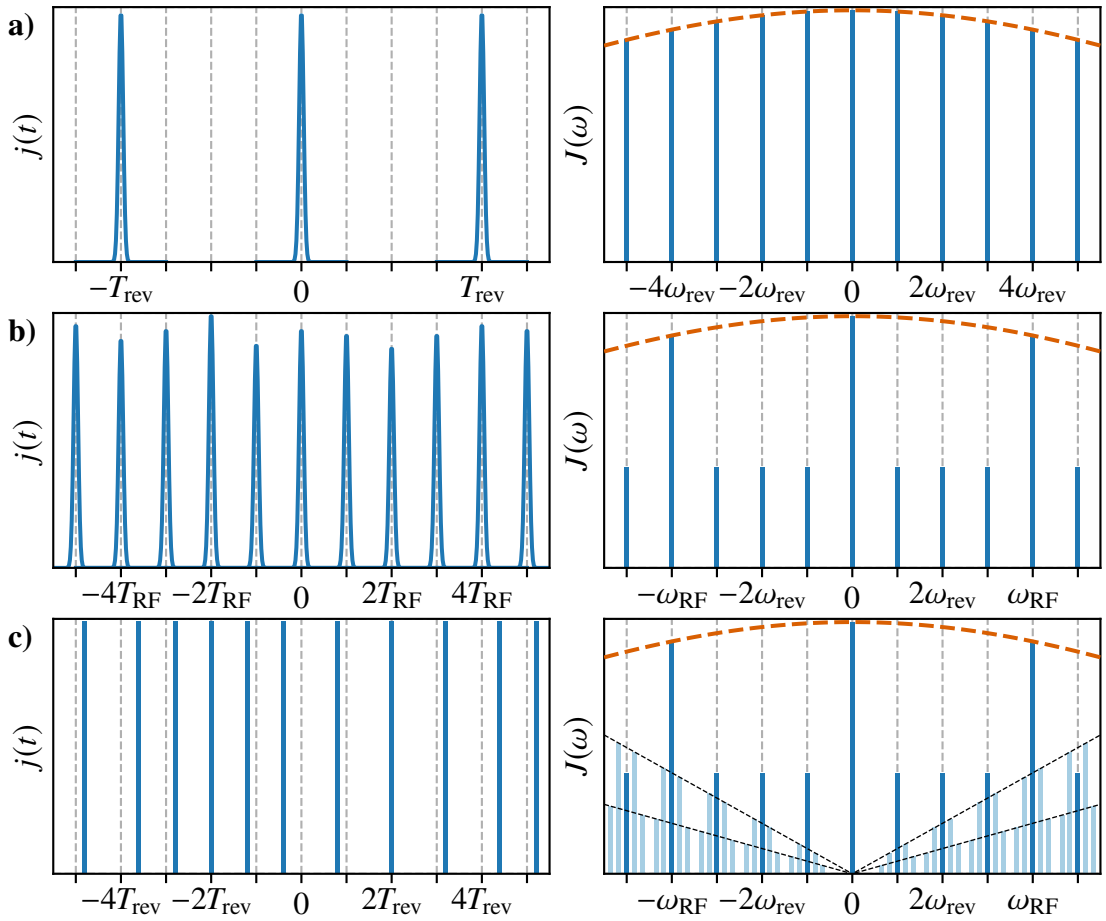

Figure 2.9.: **a)** Beam current of a Gaussian-shaped single bunch circulating around the ring in time and frequency domain. **b)** A bunch train of h bunches with slightly different bunch charges leads to spurious peaks in the spectrum at multiples of ω_{rev}. **c)** Single bunches perform synchrotron oscillations (shown as Dirac peaks for better visibility) around their nominal position resulting in sidebands in the spectrum which increase linearly with the frequency. The dashed orange line indicates the suppression of higher frequency components due to the finite bunch length (the figure is based on [4]).

system has h eigenmodes $\mu \in [0; h-1]$ each characterized by the phase shift per bucket

$$\Delta\phi = \frac{2\pi\mu}{h}, \tag{2.20}$$

while each individual bunch still oscillates with the synchrotron frequency. With the time difference from bunch to bunch $\Delta t = T_{\mathrm{rev}}/h$, Eq. (2.20) can be written as

$$\frac{\Delta\phi}{\Delta t} = \frac{2\pi\mu}{h}\frac{h}{T_{\mathrm{rev}}} = \mu\omega_{\mathrm{rev}}$$

resulting in a frequency shift of the peaks in the beam spectrum by this value, which leads to the beam spectrum for small oscillation amplitudes [46]

$$J(\omega) = \sum_{n=-\infty}^{\infty} \delta\left(\omega - n\omega_{\mathrm{RF}}\right) - i\frac{\omega\eta}{2}\delta\left(\omega - n\omega_{\mathrm{RF}} + \mu\omega_{\mathrm{rev}} + \omega_{\mathrm{s}}\right), \tag{2.21}$$

presented in Fig. 2.10.

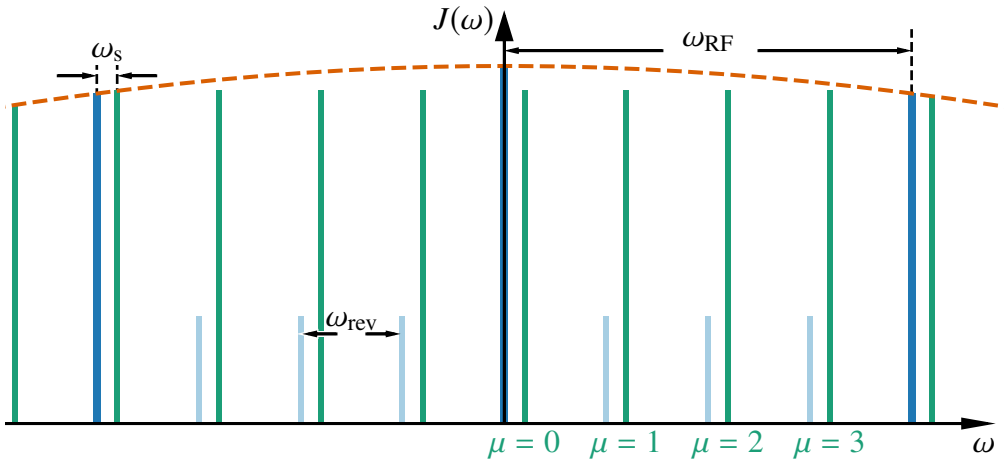

Figure 2.10.: Beam spectrum of $h = 4$ coupled bunches. The corresponding eigenmodes μ (green) create sidebands next to the RF peaks (blue) and the revolution harmonics (light blue) with a distance of the synchrotron frequency ω_{s}, given by Eq. (2.21). The dashed orange line indicates the suppression of higher frequency components due to the finite bunch length.

2.3.2. Wake function and Impedance

A particle with the charge q_1 traveling through an accelerator interacts electromagnetically with the vacuum chamber. Consequently, wake fields are induced acting back on the beam. A distinction is made between short-range wake fields and long-range wake fields, which are mostly generated in cavity-like structures with a high quality factor Q_0. Since this thesis focuses on longitudinal beam dynamics, only narrow-band, long-range wake fields, created by higher-order modes of the accelerating cavity [6] are considered in the following.

Considering a second particle q_2 following the first particle at a distance d, it interacts with the wake fields generated by q_1 and experiences a force $\vec{F}_1$. This can introduce a motion coupling of all particle inside the beam. In a storage ring, these wake fields can persist long enough that a particle may interact with its own wake field from previous turns.

The longitudinal wake function $W_\parallel$ is defined as the integral of the longitudinal component of the force $\vec{F}_1$ over the distance of interest $D \geq d$ and is given by

$$W_\parallel(z) = -\frac{1}{q_1 q_2}\int_D \vec{F_{1,\parallel}}\, dz = \frac{1}{q_1 q_2}\int_D q_1 E_z(z)\, dz = \frac{1}{q_2}\int_D E_z(t)\, dt$$

with the longitudinal electric field strength $E_z(z)$ of the source particle [44]. The longitudinal wake function can be interpreted as the energy loss ΔU per unit charge of the second particle

$$W_\parallel = -\frac{\Delta U}{q_1 q_2}.$$

To be able to study the frequency dependence of the wake function, a Fourier transform is used to define the so-called wake impedance

$$Z_\parallel(\omega) = \int_{-\infty}^{\infty} W_\parallel(t)\, e^{i\omega t} dt.$$

In the case of an extended charge distribution $j(t)$, the wake potential

$$V_\parallel(t) = \int_{-\infty}^{\infty} W_\parallel\left(t'\right) \cdot j\left(t - t'\right) dt'$$

is defined as a convolution of $W_\parallel(t)$ and $j(t)$ [47], which leads to a multiplication in the frequency domain

$$\tilde{V}_\parallel = Z_\parallel(\omega) \cdot J(\omega).$$

Knowledge of the wake impedance of the accelerator and the beam spectrum allows to calculate the frequency-dependent voltage induced by the wake fields.

2.3.3. Wake Matrix

For numerical calculations, it is advantageous to use a matrix formalism, based on [48], for the wake field at any position behind the charge q_1 with the charge vector $\vec{q}_1 = (q,0)^{\mathrm{T}}$ which is introduced below.

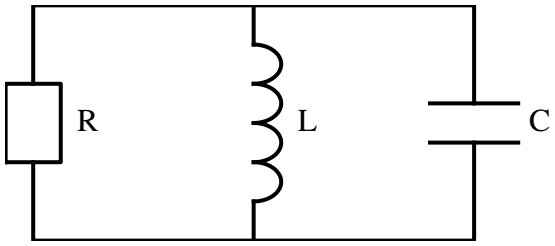

Figure 2.11.: Schematic of an RF-cavity simplified by an RLC parallel-circuit with a resistance R, an inductance L and a capacitor C.

Any cavity can be sketched by an RLC parallel-circuit with a resistance R, an inductance L and a capacitor C, as shown in Fig. 2.11. Due to Kirchhoff's current law, the total current

$$\sum_{\mathrm{k}} I_{\mathrm{k}} = I_{\mathrm{R}} + I_{\mathrm{L}} + I_{\mathrm{C}} = 0$$

vanishes and with

$$\frac{dI(t)}{dt} = \frac{1}{R}\frac{dU}{dt} + \frac{U}{L} + C\frac{d^2U}{dt^2} = 0$$

the differential equation

$$\frac{d^2U}{dt^2} + 2\chi\frac{dU}{dt} + \omega_{\mathrm{RLC}}^2 U = 0$$

is established with the resonance frequency $\omega_{\mathrm{RLC}} = 1/\sqrt{LC}$ and the attenuation $\chi = 1/2RC$. Solving this equation with the so-called natural angular frequency $\omega_{\mathrm{n}} = \sqrt{\omega_{\mathrm{RLC}}^2 - \chi^2}$ leads to [49]

$$U(t) = e^{-\chi t}\left[A_1 \cos(\omega_{\mathrm{n}} t) + B_1 \sin(\omega_{\mathrm{n}} t)\right]$$

with its derivative

$$\frac{dU}{dt} = e^{-\chi t}\left\{\cos(\omega_{\mathrm{n}} t)\left[\omega_{\mathrm{n}} B_1 - \chi A_1\right] + \sin(\omega_{\mathrm{n}} t)\left[-\alpha B_1 - \omega_{\mathrm{n}} A_1\right]\right\}. \tag{2.22}$$

Using the formula for the current in the inductance

$$I_{\mathrm{L}}(t) = \int \frac{U(t)}{t} dt,$$

a second differential equation with the ansatz

$$I_{\mathrm{L}}(t) = e^{-\chi t} \left[A_2 \cos(\omega_{\mathrm{n}} t) + B_2 \sin(\omega_{\mathrm{n}} t) \right]$$

is established together with its derivative

$$\frac{dI}{dt} = e^{-\chi t} \left\{ \cos(\omega_{\mathrm{n}} t) \left[-\chi A_2 + \omega_{\mathrm{n}} B_2 \right] + \sin(\omega_{\mathrm{n}} t) \left[-\chi B_2 - \omega_{\mathrm{n}} A_2 \right] \right\}. \tag{2.23}$$

With the initial values $U(t=0) = U_0$ and $I_{\mathrm{L}}(t=0) = I_0$, the variables

$$A_1 = U_0 \quad \text{and} \quad A_2 = I_0$$

is determined directly. Additionally, by using Eq. (2.22) and Kirchhoff's law

$$C\frac{dU}{dt} = -I_{\mathrm{L}} - \frac{U}{R},$$

with $t = 0$, the parameter B_1 is determined to

$$B_1 = -\frac{\omega}{2Q_{\mathrm{RLC}}\omega_{\mathrm{n}}} U_0 - \frac{R\omega}{Q_{\mathrm{RLC}}\omega_{\mathrm{n}}} I_0,$$

with the quality factor of the RLC-circuit Q_{RLC}.

Eventually, Eq. (2.23) is used at $t = 0$ together with the voltage of the inductance

$$U(t) = L\frac{d}{dt} I_{\mathrm{L}}(t)$$

to obtain

$$B_2 = \frac{Q_{\mathrm{RLC}}\omega}{R\omega_{\mathrm{n}}} U_0 + \frac{\omega}{2Q_{\mathrm{RLC}}\omega_{\mathrm{n}}} I_0.$$

The resistance of the RLC-circuit R represents the shunt impedance R_{s} of an impedance or a cavity, defined in Eq. (2.8), and the quality factor Q_{RLC} of the RLC-circuit represents the quality factor of the corresponding impedance or cavity Q_0, introduced in Eq. (2.6). Substituting these values and using the parameters A_1, A_2, B_1 and B_2, the differential equations

can be rewritten as

$$\begin{pmatrix} U \\ I_\mathrm{L} \end{pmatrix}_\mathrm{k} = \underline{\boldsymbol{M}}(t) \begin{pmatrix} U \\ I_\mathrm{L} \end{pmatrix}_\mathrm{k-1} \tag{2.24}$$

with $\underline{\boldsymbol{M}}(t)$ being the 2×2 wake matrix

$$\underline{\boldsymbol{M}}(t) = e^{-\chi t} \begin{pmatrix} \cos(\omega_\mathrm{n} t) - \frac{\omega}{2Q_0\omega_\mathrm{n}} \sin(\omega_\mathrm{n} t) & -\frac{R_\mathrm{s}\omega}{Q_0\omega_\mathrm{n}} \sin(\omega_\mathrm{n} t) \\ \frac{\omega Q_0}{R_\mathrm{s}\omega_\mathrm{n}} \sin(\omega_\mathrm{n} t) & \cos(\omega_\mathrm{n} t) + \frac{\omega}{2Q_0\omega_\mathrm{n}} \sin(\omega_\mathrm{n} t) \end{pmatrix}. \tag{2.25}$$

With $z = ct$, the wake matrix is used to calculate the wake field generated at the frequency ω_r by the charge q_1 at the position z_1, which is given by

$$\vec{W}(z) = \frac{R_\mathrm{s}\omega_\mathrm{r}}{Q_0} \underline{\boldsymbol{M}}(z - z_1)\, \vec{q}_1,$$

with the charge vector $\vec{q}_1 = (q,0)^\mathrm{T}$, which is linearly dependent on the cavity parameter R_s/Q_0 introduced in Section 2.1.2.

It should be noted, that the length of the wake field is determined by the damping term $e^{-\chi t}$. With the quality factor of a parallel RLC-circuit $Q_0 = RC\omega$ [50], the damping term can be expressed as $e^{-\omega/2Q_0}$, meaning that the length of the wake is proportional to the quality factor. This is particularly important for higher-order modes (HOMs) of the accelerating cavity in which the quality factor can adopt values high enough to keep the wake field length well above the accelerator circumference L_0.

2.4. Coupled-Bunch Instabilities

The bunches of a particle beam are coupled by frequency-dependent wake fields and oscillate in modes of specific frequencies ω_μ like coupled harmonic oscillators. The range of the wake fields trapped in a resonant structure depends on the quality factor Q_0 of the structure, while the coupling strength is also dependent on the shunt impedance R_s.

If a narrow-band impedance $Z(\omega)$, with a high Q_0 and therefore long-range wake fields, has a significant value at one of the beam-mode frequencies ω_μ, the beam can be excited resonantly at this frequency leading to exponential growth of the longitudinal motion, called coupled-bunch instability.

Furthermore, additional effects occur in a real storage ring (e.g., Landau damping), which

damp the oscillation amplitude, counteracting the excition of coupled-bunch instabilities.

2.4.1. Particle Dynamics with Synchrotron Radiation and External Excitations

In general, the motion of a charged particle in an electron storage ring can be described by a damped harmonic oscillator following the equation of motion

$$\ddot{z}(t) + 2\tau_{\mathrm{D}}^{-1}\dot{z}(t) + \omega_{\mathrm{s}}^2 z(t) = 0$$

with the longitudinal coordinate z, the synchrotron frequency ω_{s} and the damping rate τ_{D}^{-1}. A solution of this equation for $\omega_{\mathrm{s}} >> \tau_{\mathrm{D}}^{-1}$ is a damped sinusoidal oscillation [51]

$$x(t) = ke^{-t/\tau_{\mathrm{D}}} \sin\left(\omega_{\mathrm{s}} t + \phi\right), \tag{2.26}$$

which is mainly characterized by synchrotron radiation, since the energy loss of the particle by emitting synchrotron radiation photons leads to damping of its motion in all directions.

External excitations, e.g., from wake field effects, add a driving force $F(t)$ to the equation of motion

$$\ddot{z}(t) + 2\tau_{\mathrm{D}}^{-1}\dot{z}(t) + \omega_{\mathrm{s}}^2 z(t) = F(t).$$

If $F(t)$ is sinusoidal with ω_s and the amplitude proportional to the bunch oscillation amplitude, this equation becomes

$$\ddot{z}(t) + 2\tau^{-1}\dot{z}(t) + \omega_{\mathrm{s}}^2 z(t) = 0 \tag{2.27}$$

with $\tau^{-1} = \tau_{\mathrm{D}}^{-1} - \tau_{\mathrm{G}}^{-1}$ and the growth rate τ_{G}^{-1}.

In analogy to Eq. (2.26) for $\omega_{\mathrm{s}} >> \tau^{-1}$, the solution of the equation of motion is given by

$$x(t) = ke^{-t/\tau} \sin\left(\omega_{\mathrm{s}} t + \phi\right). \tag{2.28}$$

If $\tau_{\mathrm{G}}^{-1} > \tau_{\mathrm{D}}^{-1}$, respectively if $\tau^{-1} < 0$, the oscillation amplitude decays, if $\tau^{-1} > 0$ it grows exponentially, as shown in Fig. 2.12.

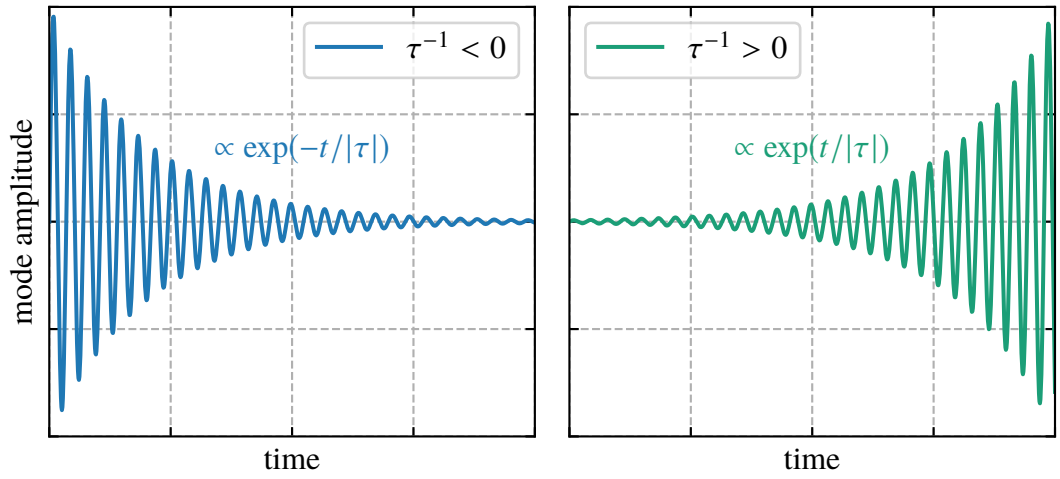

Figure 2.12.: Bunch motion in the presence of an external driving force with growth rate τ_{G}^{-1} and synchrotron radiation damping with the damping rate τ_{D}^{-1}. If $\tau^{-1} = \tau_{\mathrm{D}}^{-1} - \tau_{\mathrm{G}}^{-1} < 0$, the oscillation decays over time, as shown on the left-hand side (blue). If $\tau^{-1} > 0$, it grows exponentially, as shown in the right-hand side (green).

2.4.2. Instability Growth Rate

To illustrate the basic mechanisms of longitudinal coupled-bunch instabilities, the beam is simplified to consist only of one point-like bunch, which carries the full bunch charge $q_{\mathrm{B}} = eN_{\mathrm{ppb}}$ with N_{ppb} particles per bunch. It experiences a linear focusing force, i.e., phase focusing, and the effects of a multi-turn wake field generated by an impedance source. In this case, the longitudinal equation of motion with the longitudinal coordinate z is described by [52]

$$\ddot{z} + \omega_{\mathrm{s}}^2 z = \frac{N_{\mathrm{ppb}} e^2 \alpha}{m_{\mathrm{e}} \gamma L_0} \sum_{n=0}^{\infty} W_{\parallel}\left(z(t) - z(t - nT_{\mathrm{rev}}) - nL_0\right),$$

with the electron mass m_{e} and the Lorentz factor $\gamma = E_0 m_{\mathrm{e}}^{-1} c^{-2}$. Assuming small deviations of the wake function, which is generally given for long-range wake fields, the wake function can be linearized to

$$W_{\parallel}\left(z(t) - z(t - nT_{\mathrm{rev}}) - nL_0\right) \approx W_{\parallel}(nL_0) + W_{\parallel}'(nL_0) \cdot \left[z(t) - z(t - nT_{\mathrm{rev}})\right].$$

The constant term $W_{\parallel}(nL_0)$ only contributes a constant phase shift that compensates for the energy loss introduced by wake fields and is, thus, not important for beam dynamics and will be neglected in the following. The dynamic part proportional to

$z(t) - z(t - nT_{\mathrm{rev}}) \approx nT_{\mathrm{rev}} dz/dt$, instead, is a friction-like term which can either damp the oscillation or give rise to an instability.

Introducing the mode frequency ω_μ and changing to the frequency domain yields [44]

$$\omega_\mu^2 - \omega_{\mathrm{s}}^2 = -i \frac{N_{\mathrm{ppb}} e^2 \alpha}{m_{\mathrm{e}} \gamma L_0^2} \sum_{n=-\infty}^{\infty} n\omega_{\mathrm{rev}} Z_\parallel (n\omega_{\mathrm{rev}}) - \left(n\omega_{\mathrm{rev}} + \omega_\mu\right) Z_\parallel \left(n\omega_{\mathrm{rev}} + \omega_\mu\right). \tag{2.29}$$

Assuming that the wake field only results in small deviations of ω_μ from the nominal synchrotron frequency ω_{s}, the mode frequency can be replaced by the synchrotron frequency on the right hand side of Eq. (2.29).
This results in the complex frequency deviation [44, 46, 52, 53]

$$\Delta\omega_\mu = -i \frac{N_{\mathrm{ppb}} e^2 \alpha}{2\omega_{\mathrm{s}} m_{\mathrm{e}} \gamma L_0^2} \sum_{n=-\infty}^{\infty} n\omega_{\mathrm{rev}} Z_\parallel (n\omega_{\mathrm{rev}}) - (n\omega_{\mathrm{rev}} + \omega_{\mathrm{s}}) Z_\parallel (n\omega_{\mathrm{rev}} + \omega_{\mathrm{s}}).$$

The real part of $\Delta\omega_\mu$ describes the perturbed synchrotron oscillation frequency of the collective beam motion, i.e., the frequency shift

$$\mathrm{Re}(\Delta\omega_\mu) = \frac{N_{\mathrm{ppb}} e^2 \alpha}{2\omega_{\mathrm{s}} m_{\mathrm{e}} \gamma L_0^2} \sum_{n=-\infty}^{\infty} n\omega_{\mathrm{rev}} \mathrm{Im}\left(Z_\parallel (n\omega_{\mathrm{rev}})\right) - (n\omega_{\mathrm{rev}} + \omega_{\mathrm{s}}) \mathrm{Im}\left(Z_\parallel (n\omega_{\mathrm{rev}} + \omega_{\mathrm{s}})\right)$$

while the imaginary part of $\Delta\omega_\mu$ is the instability growth rate

$$\mathrm{Im}(\Delta\omega_\mu) = \tau_{\mathrm{G}}^{-1} = \frac{e N_{\mathrm{ppb}} e \alpha}{2\omega_{\mathrm{s}} \gamma m_{\mathrm{e}} L_0} \sum_{n=-\infty}^{\infty} (n\omega_{\mathrm{rev}} + \omega_{\mathrm{s}}) \mathrm{Re}\left[Z_\parallel (n\omega_{\mathrm{rev}} + \omega_{\mathrm{s}})\right]. \tag{2.30}$$

In analogy, for N_{b} bunches the growth rate for multibunch mode μ is given by

$$\tau_{\mathrm{G},\mu}^{-1} = \frac{e I \alpha}{2\omega_{\mathrm{s}} \gamma m_{\mathrm{e}} c^2 T_{\mathrm{rev}}} \sum_{n=-\infty}^{\infty} \left(n N_{\mathrm{b}} \omega_{\mathrm{rev}} + \mu\omega_{\mathrm{rev}} + \omega_{\mathrm{s}}\right) \mathrm{Re}\left[Z_\parallel \left(n N_{\mathrm{b}} \omega_{\mathrm{rev}} + \mu\omega_{\mathrm{rev}} + \omega_{\mathrm{s}}\right)\right] \tag{2.31}$$

with $L_0 = cT_{\mathrm{rev}}$ and the beam current $I = N_{\mathrm{b}} N_{\mathrm{ppb}} e / T_{\mathrm{rev}}$.

The fact, that the growth rate $\tau_{\mathrm{G},\mu}^{-1}$ is proportional to the current I, while the damping rate τ_{D}^{-1} is constant, leads to a so-called instability threshold I_{thr}. While $I < I_{\mathrm{thr}}$ the beam remains stable, whereas coupled-bunch instabilities are excited when $I > I_{\mathrm{thr}}$.

2.4.3. Additional Damping Mechanisms

In order to suppress coupled-bunch instabilities to increase the beam quality and the instability current threshold, two different approaches are used and briefly described below.

The first possibility are bunch-by-bunch feedback systems, which are explained in more detail in Chapter 3.3. Such a feedback system basically detects the frequency, phase and amplitude of a coupled-bunch instability and actively damps the oscillations of each single bunch. Since the bunch oscillation is sinusoidal, the turn-by-turn position of a bunch measured at a given position is a sampled sinusoid signal. The force applied by the feedback with fast electromagnets, called feedback kickers, is proportional to the derivative of the bunch oscillation and can be generated by shifting the sampled signal of the position of the bunch by a phase shift of $\pi/2$. This adds an additional damping term τ_{FB}^{-1} to the factor τ^{-1} from Eq. (2.27) resulting in

$$\tau^{-1} = \tau_{\mathrm{D}}^{-1} - \tau_{\mathrm{G}}^{-1} + \tau_{\mathrm{FB}}^{-1}.$$

To completely damp the bunch oscillation, the condition $\tau^{-1} < 0$ must be satisfied again.

The second option is Landau damping [54], which has its origin in a synchrotron frequency spread of the particles in the beam. To describe this complex effect, an impedance is considered driving the beam at a specific frequency ω_μ, similar to a driving force of a harmonic oscillator. A bunch, consisting of N_{ppb} particles oscillating with the same frequency ω_μ is resonantly excited by the impedance resulting in exponentially growing oscillation amplitudes of all particles. Adding a synchrotron frequency spread to the particles inside the bunch leads to a smaller excitation of the whole ensemble due to the fact that some oscillators have their resonance frequency shifted away from the driving frequency. The higher the frequency deviation $\Delta\omega$ from ω_μ, the lower the excitation of the particle. In sum, this leads to a suppression of the coupled-bunch motion (see e.g. [21, 44, 55]). This means, that this effect does not add additional damping, but still stabilizes the beam by suppressing the excitation of coupled-bunch instabilities[56].

Landau damping can be induced by RF-phase modulation, which increases the synchrotron frequency spread. With this method, the stability of the beam is increased by suppressing the excitation of coupled-bunch instabilities before they emerge, instead of reacting with additional damping. However, the beam quality suffers from using RF phase modulation due to the increased bunch length and energy spread, as shown in Section 2.2.5.

3. The Electron Storage Ring DELTA

Experimental studies analyzing the interaction of coupled-bunch instabilities and RF phase modulation were performed at the 1.5 GeV electron storage ring DELTA[1], operated by the TU Dortmund University and used as a synchrotron light source. In this chapter, an overview of the most important components, systems and diagnostic tools of DELTA is given together with its basic parameters.

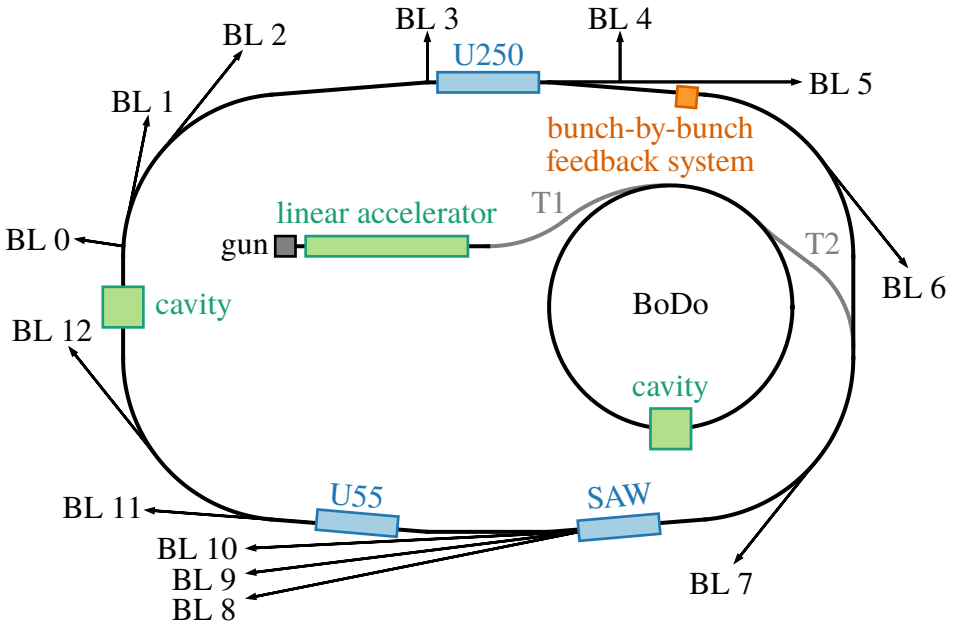

Figure 3.1.: Sketch of the synchrotron radiation source DELTA. Electrons from the gun are accelerated in the linear accelerator and the RF cavities implemented in the booster BoDo (green). Three insertion devices (blue) provide high-intensity radiation, while most of the other beam lines (BL) use synchrotron light from bending magnets. A bunch-by-bunch feedback system is installed to counteract coupled-bunch instabilites (orange).

[1] "**D**ortmunder **EL**ek**T**ronen Speicherring **A**nlage" (electron storage ring facility in Dortmund)

Table 3.1.: Basic parameters of the DELTA storage ring [59, 60].

Parameter	Symbol	Value
circumference	L_0	115.2 m
nominal beam energy	E_0	1.5 GeV
maximum beam current	$I_{\max}$	130 mA
momentum compaction factor	α	4.9×10^{-3}
harmonic number	h	192
revolution frequency	f_{rev}	2.6 MHz
master RF frequency	f_{RF}	499.817 MHz
synchrotron frequency	f_{s}	(15.2 - 16.4) kHz
bunch length (FWHM)	σ_{T}	100 ps
cavity shunt impedance	R_{s}	3 MΩ
cavity power	P_{c}	25 kW
bending radius (dipoles)	R_{b}	3.3 m

3.1. Overview

At DELTA, a 90 keV thermoelectric gun emits electrons which are accelerated to 70 MeV in a linear accelerator. Afterwards, they reach their final energy of 1.5 GeV in a booster-synchrotron called BoDo[2]. This allows a full-energy injection into the storage ring, executed with several kickers and a static injection-bump, where the electrons are stored for several hours. A sketch of the DELTA storage ring is shown in Fig. 3.1. In order to compensate the energy loss of the beam due to synchrotron radiation, DELTA has a 500 MHz DORIS-type cavity [57]. With the main DELTA parameters, summarized in Table 3.1, the amplitude of the voltage powering the cavity is $\hat{U} \approx 387\,\mathrm{kV}$ with a synchronous phase of $\overline{\phi}_{\mathrm{s}} \approx 20.3\,\mathrm{deg}$[3].

To reduce trapped-ion effects [58] during user operation, only 144 of the $h = 192$ buckets are filled with electrons accumulating a current up to $I_{\max} = 130\,\mathrm{mA}$. Between injections, several beam lines provide synchrotron radiation to the experimental stations. In addition to beam lines supplied with synchrotron radiation from bending magnets, DELTA is equipped with three insertion devices, a permanent-magnet undulator (U55), an electromagnetic undulator (U250) and a superconducting wiggler (SAW).

[2] Booster Dortmund
[3] The detailed calculations are presented in the Appendix A.1.

3.2. Phase Modulation at DELTA

After the sporadic occurrence of longitudinal coupled-bunch instabilities leading to beam losses or partial beam losses, an RF phase modulation system was implemented in 2008 [32]. It mainly consists of a digital phase shifter [61] and a dual current-feedback amplifier [62]. The system is used to modulate the 500 MHz master-RF-signal before it is amplified by a klystron.

For this purpose, the master-RF-signal U_{RF} is sent to the phase modulation system together with a control voltage U_{C}, as illustrated in Fig. 3.2, resulting in a modulated output signal U_{mod} supplying the RF-cavity after amplification. The phase shift applied to the input signal follows the characteristic curve shown on the right side of Fig. 3.2 and depends only on the control voltage U_{C}. At DELTA, a DC input voltage of $U_{\mathrm{DC}} = 9\,\mathrm{V}$ is added to U_{C} leading to an output signal

$$U_{\mathrm{mod}}\left(U_{\mathrm{C}}=0\right) = \hat{U}_{\mathrm{mod}} \sin\left(\omega_{\mathrm{RF}} t + \phi_{\mathrm{DC}}\right),$$

with the amplitude $\hat{U}_{\mathrm{mod}}$.

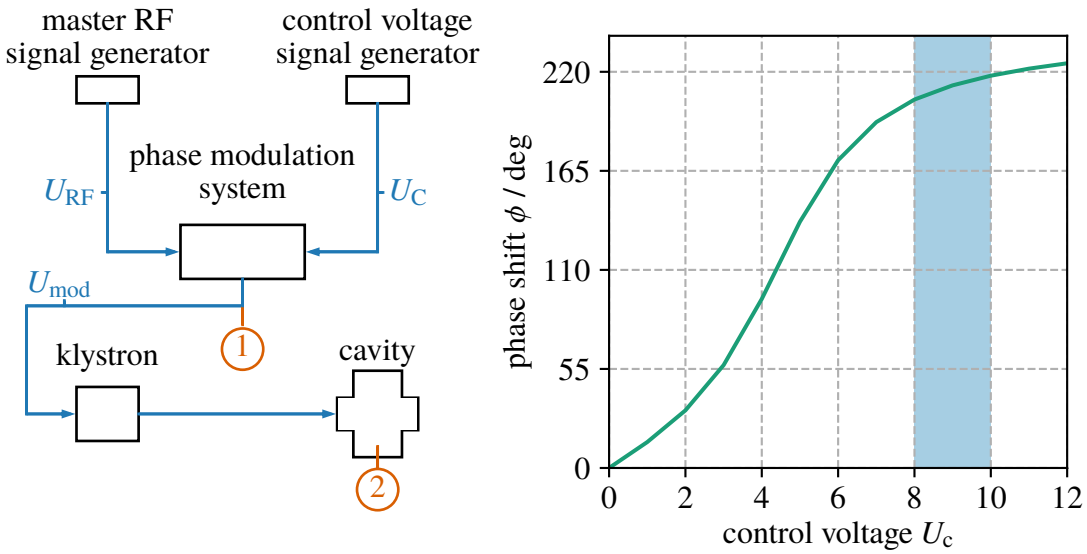

Figure 3.2.: **Left:** Schematic of the phase modulation system tuned by the control voltage U_{C}. An RF-signal is produced by the master RF signal generator, modulated by the phase shifter, amplified by the klystron and sent to the cavity. The orange marks show pickup probes used to measure the phase shift of the modulation system (1) and inside the cavity (2), as further discussed in Chapter 5.2. **Right:** Characteristic curve of the phase modulation system used at approximately 500 MHz [61]. The highlighted area is the voltage range operated at DELTA [32].

Additionally, a sine signal provided by a signal generator [63] is used as the control voltage

$$U_\mathrm{C} = \hat{U}_\mathrm{C} \sin\left(\omega_\mathrm{c} t\right)$$

with the amplitude $\hat{U}_\mathrm{C}$ and the frequency $\omega_\mathrm{c} = \omega_\mathrm{mod}$. For historical reasons, $\hat{U}_\mathrm{C}$ is specified as the peak-to-peak amplitude [32]. The control panel of the phase modulation system in the DELTA control room is also set to peak-to-peak amplitudes. Therefore, the values for $\hat{U}_\mathrm{C}$ are specified for peak-to-peak amplitudes to prevent cofusion, but $\hat{U}_\mathrm{C}$ is referred to as amplitude in the following for simplicity. The maximum value for $\hat{U}_\mathrm{C}$ is 6 V [32, 61]. However, only the range $\hat{U}_\mathrm{C} \in [0,3]\,\mathrm{V}$ is analyzed in this thesis, because of low signal-to-noise ratios for high values of $\hat{U}_\mathrm{C}$ (see Chapter 5.4 and 5.5). Using U_C, the output changes to

$$U_\mathrm{mod} = \hat{U}_\mathrm{mod} \sin\left(\omega_\mathrm{RF} t + \phi\left(\hat{U}_\mathrm{C}\right) \sin\left(\omega_\mathrm{mod} t\right)\right), \tag{3.1}$$

with the phase shift $\phi\left(\hat{U}_\mathrm{C}\right)$ only depending on the amplitude of the control voltage $\hat{U}_\mathrm{C}$. In addition, the phase shift inside the cavity ϕ is expected to be lower than the phase shift of the phase modulation system ϕ_PS due to the finite bandwidth of the cavity. The cavity bandwidth is usually described by the quality factor

$$Q_0 = \frac{\omega_\mathrm{res}}{\Delta\omega}$$

with the resonance frequency ω_res and the bandwidth $\Delta\omega$ between the two -3 dB-points, where the spectral power is at 50 % of the maximum value at ω_res.

During user operation, ω_mod is usually set to a frequency slightly below twice the synchrotron frequency ω_s and $\hat{U}_\mathrm{C}$ is set between 400 mV and 1000 mV. Unfortunately, this gives no information about the phase shift applied to the beam. With the RF phase modulation running, the coupled-bunch instability sidebands vanish and the unwanted beam losses are stopped. As a side effect, a beam lifetime increase of about 20 % is observed at the cost of beam quality [32].

3.3. Bunch-by-Bunch Feedback System

The most important diagnostic tool for this thesis is the digital bunch-by-bunch feedback system [46]. It is capable of detecting the longitudinal, horizontal and vertical position of every bunch relative to its reference coordinates. With the position data of every bunch at

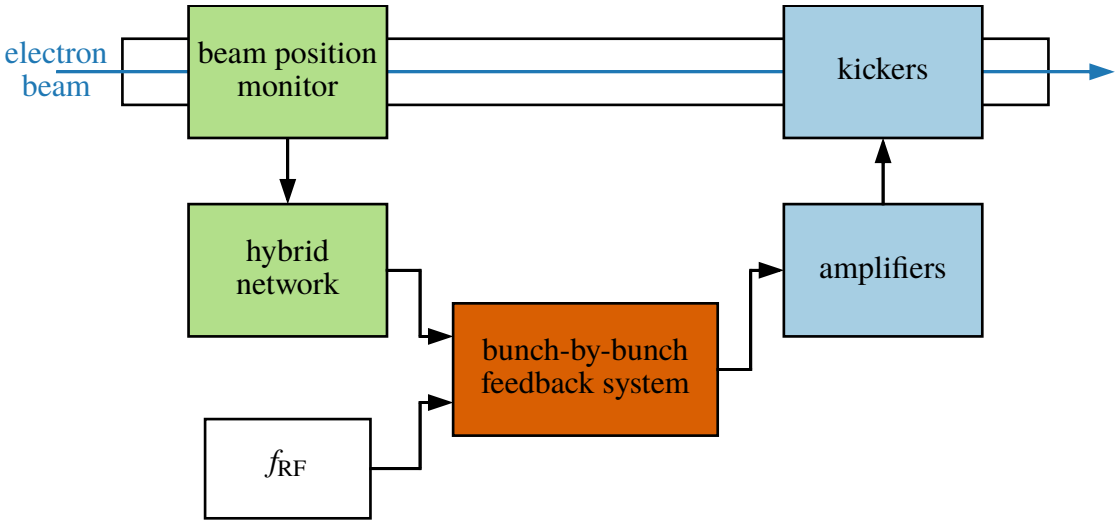

Figure 3.3.: Overview of the digital bunch-by-bunch feedback at DELTA. The signals from a beam position monitor are sent via a hybrid network to the bunch-by-bunch feedback system together with the master RF signal. The feedback system calculates output signals, which are first amplified and then applied to the beam by fast-pulsed kickers.

every turn, bunch-by-bunch modes can be measured as shown in Section 5.3.

In addition to its diagnostic capabilities, the system can be used to act back on the beam to damp, or excite coupled-bunch oscillations. With an inbuilt signal generator, even arbitrary signals can be sent to the beam to excite specific resonances.

The bunch-by-bunch feedback system used at DELTA is a commercial system by Dimtel, Inc. [64]. The design for the kickers applying the output signal to the beam are adapted from the feedback systems used at BESSY II [47, 65]. Very similar kickers are also in use at several other storage rings [51]. An overview of the main components of the bunch-by-bunch feedback is shown in Fig. 3.3. A beam position monitor and a hybrid network, illustrated in detail in Section 3.3.1, are used to detect the transverse and longitudinal position of every bunch at every turn. This data is evaluated by the processing units of the feedback system, presented in Section 3.3.2. In addition, output signals are calculated to compensate the bunch motions and sent via amplifiers to pulsed kickers, which are shown in Section 3.3.3.

3.3.1. BPM and Hybrid Network

To detect the horizontal, vertical and longitudinal position of every bunch, a so-called beam position monitor (BPM) is used. It consists of four pickup electrodes surrounding the beam, as shown on the left hand side of Fig. 3.4. Whenever a bunch passes the BPM, its electromagnetic field induces a voltage inside the pickup electrodes with a signal strength depending on the distance between bunch and pickup. In order to separate the coordinates of the bunch, the signals are processed into three dedicated signals.

For this purpose, a "Dimtel Hybrid Network" [64], illustrated in the right hand side of Fig. 3.4, provides the sum signal Σ and the differential signals ΔX and ΔY, while the diagonal difference output signal Q is terminated with 50 Ω. For the longitudinal plane, the sum of all pickup signals is used. With the amplitude of this signal being proportional to the beam current, it does not depend on the transverse position of the beam. However, the signal gives information about the time when the bunch passes the BPM. The longitudinal position of the bunch is given by the phase deviation with respect to the synchronous RF phase. To measure the vertical position, the hybrid network subtracts the sum of the pickup signals C and D from the sum of the signals A and B to generate the ΔY signal (see Fig. 3.4). The horizontal ΔX-signal is created by subtracting signals A and D from B and C.

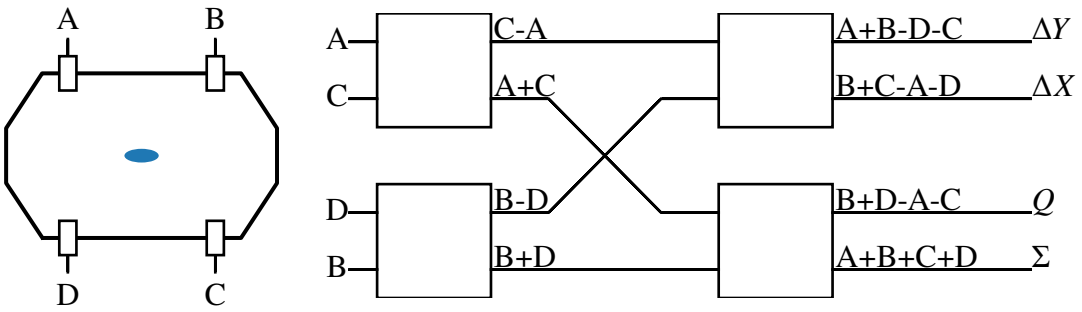

Figure 3.4.: **Left:** Sketch of a beam position monitor with four pickup electrodes surrounding the beam. **Right:** Block diagram of a Dimtel Hybrid Network [64]. Each hybrid module has a sum and a difference output. In the configuration used here, they provide a sum signal of all four pickups Σ, two differential signal ΔX and ΔY for both transverse coordinates and a diagonal difference output Q.

Figure 3.5.: Photo of the bunch-by-bunch feedback system units and the corresponding amplifiers at DELTA. **Left:** From top to bottom, the clock and trigger unit, the combined front-/backend unit and the three FPGA-based gigasample-processors. **Right:** The three amplifiers (longitudinal at the top, transverse below) send the output signals of the feedback system to fast-pulsed kicker structures.

3.3.2. Processing Units

The core part of the bunch-by-bunch feedback system consists of one combined front-/back-end unit and three identical signal processing units for the three planes. The signals from the hybrid network are sent to the front-end unit, where they are stretched by a two-cycle comb filter and mixed with a 1.5 GHz reference signal, which is an upconverted signal from the master RF oscillator [64]. A photo of the feedback units and amplifiers used at DELTA are shown in Fig. 3.5.

After preprocessing, the dedicated signals are transferred to the corresponding processing units, where they are digitized by 12-bit analog-to-digital converters (ADCs) with a 500 MHz sampling rate phase-locked to the RF master oscillator. By default, one sample per revolution per bunch is taken by the FPGA-based gigasample processors. The beam signal is also separated into 192 channels, one for each RF bucket.

Each unit is equipped with static memory capable of storing 65 536 data points in each of the 192 channels. With the revolution time of DELTA of $T_{\mathrm{rev}} = 384\,\mathrm{ns}$, this leads to a maximum data acquisition time of $t_{\mathrm{acq}} = 25.2\,\mathrm{ms}$, if one data point is taken per bunch per turn. This time can be prolonged by downsampling a factor D, i.e., data points are only taken in every D-th turn for every bunch, at the cost of loss of information in the unobserved

revolutions.

In addition to the diagnostic capabilities, each processing unit produces an output signal to compensate coupled-bunch motion of the electron beam [46]. While coupled-bunch modes are characterized by the phase advance between the bunches, each bunch oscillates with the synchrotron frequency ω_s. The functionality of bunch-by-bunch feedback systems is to damp coupled-bunch instabilities by damping the oscillation of every single bunch. For this purpose, the output signal has to be proportional to the derivative of the bunch oscillations [51]. In each channel, the turn-by-turn samples of a given bunch are processed by a n-tap finite impulse response (FIR) filter, where n is an integer number usually set to $n = 24$ at DELTA, suppressing the DC component and phase shifting the sinusoidal input signal by $\pi/2$. In addition, the phase advance between the BPM and the position at which the output signal is applied to the beam has to be taken into account.

The output signal is converted back to an analog signal by a digital-to-analog converter (DAC), amplified and sent to fast-pulsed kickers, presented in the next chapter, which apply small "kicks" every turn to the bunch to compensate its oscillation. Since these kicks should always reduce the oscillation amplitude, this process is called negative feedback. It is also possible to excite existing coupled-bunch modes by positive feedback. In this case, the output signal is additionally phase-shifted by π, which increases the amplitude of the bunch oscillation enhancing coupled-bunch instabilities. In the longitudinal plane, the signal is sent from the DAC back to the back-end module where it is upconverted to 1.5 GHz, using a phase mixer and a bandpass filter, before it is forwarded to the amplifier. This is necessary, since the longitudinal kicker cavity used at DELTA operates at this frequency.

Furthermore, each unit has a built-in numerically controlled oscillator, called drive, which serves as a frequency generator. It can be used to create an RF signal with fixed amplitude, frequency and phase, which can be applied individually or in addition to the output signal.

3.3.3. Amplifiers and Kicker Structures

The output signals of the transverse processing units as well as the upconverted longitudinal output signal from the back-end module are transferred to amplifiers. In the longitudinal plane, a high-frequency amplifier [66] with a bandwidth Δf of 1 to 2 GHz and a gain of 59 dB is used. For the transverse plane, two identical amplifiers are used with an operation bandwidth of 10 kHz to 250 MHz and a gain of 50 dB [67].

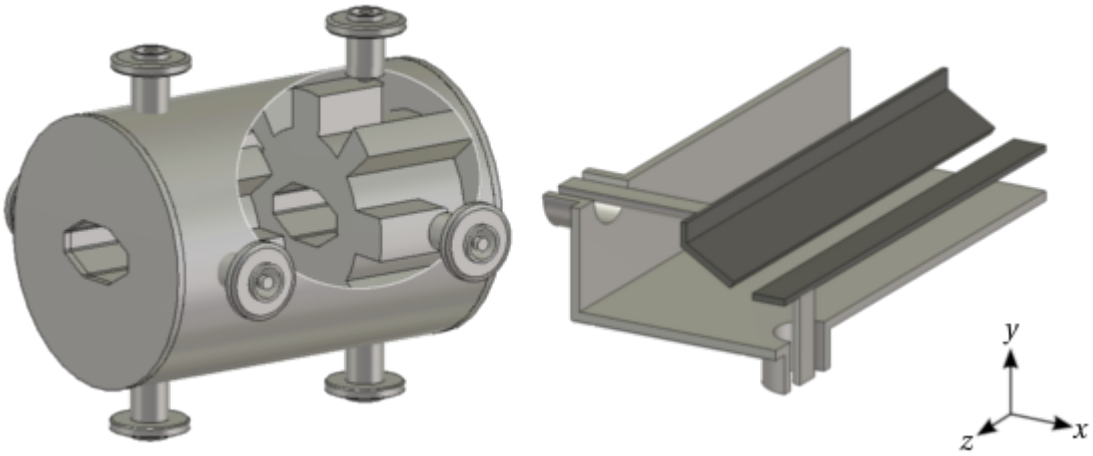

Figure 3.6.: Sketch of the fast-pulsed kicker structures used for the bunch-by-bunch feedback system at DELTA. **Left:** Overdamped cavity-like kicker for the longitudinal plane. **Right:** 1/8 of the combined stripline kicker for the transverse planes [69].

After amplification, the signals are sent to kickers to apply the signals to the electron beam. The kickers used at DELTA are mainly unmodified versions of the kickers used at BESSY-II [47, 65], making tapering the structures to the DELTA vacuum chamber necessary.

For the horizontal and vertical plane, a combined stripline kicker for both planes is used as shown in the right hand side of Fig. 3.6. It utilizes four electrodes with a length of 30 cm, which are shaped according to the DELTA vacuum chamber. With a sampling rate of $f_{\mathrm{samp}} = 500\,\mathrm{MHz}$ given by the RF frequency, the bandwidth of the kicker structure has to be $\Delta f \leq f_{\mathrm{samp}}/2$ in order to be able to distinguish the bunches and kick every bunch separately. This requirement is described by the Nyquist-Shannon sampling theorem [68]. The transverse stripline kicker used at DELTA operates in the baseband from 0 MHz to 250 MHz satisfying the bandwidth requirement. The horizontal and vertical shunt impedances are different due to the geometry of the DELTA vacuum chamber. The distance between the horizontal electrodes is approximately twice the distance of the horizontal electrodes resulting in a vertical shunt impedance which is approximately twice as high as the horizontal shunt impedance [65, 69]. Although the kicker has two electrodes for each plane, only one horizontal and one vertical electrode is powered, which is sufficient becuase the transverse coupled-bunch instabilities occurring at DELTA have vanishingly small growth rates.

For the longitudinal plane, a different kind of kicker magnet is used. In 1995, a cavity-like kicker structure was developed at DAΦNE [70] with a higher longitudinal shunt impedance

than longitudinal stripline kickers. The cavity-like kicker used at DELTA is depicted in the left-hand side of Fig. 3.6 and has a resonance frequency of 1.5 GHz. Just like the transverse kickers, the bandwidth of the longitudinal kicker has to be $\Delta f \leq 250\,\mathrm{MHz}$, which sets the boundary condition, according to Eq. (2.6), that the quality factor of the cavity has to be $Q_0 \leq 6$. This is assured by strongly loading the "pillbox"-cavity in the middle of the structure with ridged waveguides at both ends. That way, the quality factor of the cavity is reduced to $Q_0 \approx 5.6$ with a shunt impedance of $R_{\mathrm{s},\parallel} \approx 1\,\mathrm{k}\Omega$ [65], which is about twice as high as the shunt impedance of a comparable stripline kicker [70]. The ridged waveguides are also used to couple the output signal of the back-end unit into the cavity.

4. Beam Dynamics Simulation

The complex dynamics of coupled-bunch effects in the presence of RF phase modulation cannot be calculated analytically. For this reason, numerical calculations are used to achieve first impressions on the particle dynamic and expectations for the subsequent measurements.

The common approach to simulate coupled-bunch instabilities caused by long-range wake fields generated in highly resonant structures is to simplify the particle bunches to rigid macro-particles [9, 46, 48, 71, 72] carrying the full bunch charge $q_B = N_{ppb} \cdot e$, as already assumed in Section 2.4.2. Although numerical results from this approach are generally in good agreement with measurements, it cannot be used in the presence of RF phase modulation. In this case, many particles per bunch are required to induce Landau damping to the beam and suppress the excitation of coupled-bunch instabilities. To analyze RF phase modulation, on the other hand, several tracking codes are available, which focus on the effects on the longitudinal phase space [21, 24, 40, 41]. To be able to track multiple particles over ten thousands of turns, these codes consider all particles independently (in contrast to the previous approach where the particles are coupled by wake fields). This is a valid assumption in the absence of wake field effects and allows to calculate the interaction of the particles with the RF field by matrix operations. The huge advantages of using matrix operations are that these procedures are generally very performant, they calculate the interaction of all particles at the same time and can be optimized by parallelization techniques. Unfortunately, this assumption is not valid when wake field effects are taken into account. In this case, the particles are coupled and the dynamics of every particle depends on the wake fields generated by the previous particles. Simply calculating all particles one after another in every turn is also no option, since that would require an enormous computing effort and time.

The solution is to combine both approaches. For this purpose, the Python tracking code MALTE [1] has been developed, based on the MuSiC code presented in [48]. MALTE utilizes

[1] coupled-bunch **M**ulti p**A**rtic**L**e **T**racking cod**E**

state-of-the-art libraries, e.g. the *scipy ecosystem* [73], to track particles through a virtual recirculating accelerator with a phase-modulated RF field in the accelerating cavity and evaluates wake-field and coupled-bunch effects at every turn as presented below.

The general idea of MALTE is to keep the simulation as simple as possible and to reduce the computation time. Its concept is discussed in Section 4.1, while Section 4.2 focuses on the simulation parameters. Section 4.3 shows a first study analyzing the growth rate of a coupled-bunch instability as a function of the beam current, which also serves as a validation of the code. In Section 4.4, the growth rate is analyzed as a function of the modulation amplitude.

4.1. Concept

In order to reduce the complexity of MALTE, the optics of the investigated storage ring is represented by the momentum compaction factor. Thus, most components (like magnets, drift spaces, etc.) do not have to be taken into account reducing the calculation effort drastically.

This leaves the accelerating cavity as the only component, which is taken into account separately. When the particles pass the cavity, they experience a focusing effect introduced in Section 2.2.4, i.e., the energy of each particle is changed depending on its longitudinal position within the bunch. Instead of taking the whole impedance spectrum of the cavity into account, a passive cavity-like structure is added at the position of the cavity, called impedance structure in the following, representing a harmful higher-order mode (HOM) of the cavity. Whenever a particle passes the impedance structure, it stores a part of its energy in the structure exciting wake fields, which can give rise to coupled-bunch instabilities.

The particle beam is generated by h equidistant RF buckets. These buckets can be filled arbitrarily with N_b bunches. All particles are created with a random time deviation δt and energy deviation δE with respect to the reference particle of the bucket with $\delta t = \delta E = 0$. For both, energy and time, Gaussian distributions with standard deviations σ_T and σ_E are used. In addition, an artificial temporal phase-space boundary is used as a termination criterion to handle parameter sets that lead to unstable or unrealistic solutions. If the time coordinate of a particle exceeds half the time between two bunches $T_\mathrm{RF}/2$, it overlaps with particles of the adjacent bunch and the termination criterion is met.

In order to adequately represent the influence of RF phase modulation, a sufficiently large

quantity of particles per bunch is needed in the numerical simulation. First-order coupled-bunch interactions, on the other hand, do not depend on intra-bunch motion, which, hence, can be neglected as discussed later in the thesis. While it is necessary to calculate phase-focusing effects for every single particle, the interaction inside the impedance structure is calculated only for the center of mass of each bunch and the resulting energy change is applied to all particles within the bunch. In addition, for phase-focusing effects, all particles are considered independently, reducing the calculation effort to one matrix operation per bunch for each phase-space coordinate. That is not possible for wake field effects, since the interaction of a bunch with the wake field depends on the bunches previously interacted with it. To further improve the performance of MALTE, synchrotron radiation effects are neglected completely, which is possible since neither coupled-bunch growth rates nor RF phase modulation effects are influenced by synchrotron radiation[2].

A particle with charge q_0 traveling through the storage ring experiences three interactions during each turn as presented below.

Firstly, the particle passes an accelerating cavity with a length[3] $l_c = 0$. Since synchrotron radiation effects are neglected, the particle is not accelerated, but instead, the synchronous phase (the phase of the reference particle) is set to $\phi_s = \pi$. According to Section 2.2.4, the particle is phase focused due to

$$\Delta E = \Delta E_{RF} = q_0 \hat{U} \sin\left(\omega_{RF}\delta t + \phi_0\right) \tag{4.1}$$

with the energy loss due to synchrotron radiation $\Delta E_s = 0$. If phase modulation is taken into account, this changes to

$$\frac{\Delta E}{q_0} = \hat{U} \sin\left(\omega_{RF}\delta t + \eta \sin\left(\omega_{mod}\delta t\right) + \phi_0\right),$$

according to Section 2.1.3 with the modulation amplitude η and the modulation frequency ω_{mod}.

Secondly, while passing the ring, the phase of every particle is changed based on its energy deviation and the momentum compaction factor defined in Eq. (2.10). For ultrarelativistic particles, it can be shown that [34]

$$\frac{\Delta L}{L_0} \approx \frac{\Delta T}{T_{rev}}$$

[2] Synchrotron radiation damping determines whether the beam is stable or not depending on the relation of τ_D^{-1} and τ_G^{-1}, but the growth rate itself does not depend on synchrotron radiation.

[3] Thin-lens approximation can be used here, since all particles travel at $v \approx c$.

and, thus, Eq. (2.10) can be rearranged to

$$\Delta T = \alpha \frac{L_0}{c} \frac{\Delta E}{E_0} \tag{4.2}$$

with $T_{\mathrm{rev}} = L_0/c$.

The third interaction happens in the narrow-band impedance structure characterized by its quality factor Q_r, its shunt impedance R_s and its resonance frequency ω_r. It is responsible for wake-field and potential coupled-bunch effects, so that the whole bunch has to be taken into account. Since intra-bunch motion is neglected, the center of mass of the bunch is calculated by the mean of δt of all particles inside the bunch. When this macro particle with charge $q_\mathrm{B} = N_\mathrm{ppb} \cdot q_0$ passes the unloaded structure, it stores a part of its energy in the structure which is equal to

$$\Delta E = -\frac{e}{E_0}\left(q_\mathrm{B} \frac{R_\mathrm{s}\omega_\mathrm{r}}{2Q_\mathrm{r}}\right)$$

with the nominal energy E_0 due to the fundamental theorem of beam loading [74]. The impedance structure basically behaves like an RLC resonance circuit which was analyzed in Section 2.3.3. The wake field generated by the first bunch with the initial "charge vector" $\vec{q}_0 = \left(q_\mathrm{B},0\right)^T$ at the time t_0 is taken into account by using the wake matrix $\underline{\boldsymbol{M}}$ to calculate the charge vector

$$\vec{q}_1(t_1) = \underline{\boldsymbol{M}}(t_1 - t_0)\,\vec{q}_0 + \begin{pmatrix} q_\mathrm{B} \\ 0 \end{pmatrix}$$

of a second bunch passing the structure at $t_1 > t_0$, which is proportional to the value of the wake field [48]. This bunch interacts with the wake field within and experiences an energy change according to

$$\Delta E_\mathrm{WF} = e\frac{R_\mathrm{s}\omega_\mathrm{r}}{Q_\mathrm{r}E_0}\left(\frac{q_\mathrm{B}}{2} + \left[\underline{\boldsymbol{M}}(t_1 - t_0)\,\vec{q}_0\right]_1\right)$$

which is applied to all particles inside the bunch, where the notation $\left[\underline{\boldsymbol{M}}(t)\,\vec{q}\right]_1$ means the first element of the matrix.

In conclusion, the phase-space coordinates δE_n and δt_n of turn n are calculated depending on the current charge vector $\vec{q}_n$ and the coordinates of the previous turn leading to

$$\begin{aligned}
\Delta E_\mathrm{WF} &= e\frac{R_\mathrm{s}\omega_\mathrm{r}}{Q_\mathrm{r}E_0}\left(\frac{q_\mathrm{B}}{2} + \left[\underline{\boldsymbol{M}}(t_\mathrm{tot})\,\vec{q_{n-1}}\right]_1\right) \\
\delta E_{n,p} &= \Delta E_{n-1,p} + \hat{U}\sin\left(\omega_\mathrm{RF}\delta t_{n-1,p} + \eta\sin\left(\omega_\mathrm{mod}\delta t_{n-1,p}\right) + \phi_0\right) - \Delta E_\mathrm{WF} \\
\delta t_{n,p} &= \delta t_{n-1,p} + \frac{\alpha L_0 c}{E_0}\delta E_{n,p}
\end{aligned}$$

for every particle p with the total time t_{tot} since the last bunch passed the structure. In addition, the charge vector $\vec{q}_n$ is recalculated for every bunch together with t_{tot}. Since the particles can be considered independent for the second and third interaction, both calculations are performed in one matrix operation each.

4.2. Choice of Parameters

Because the computational resources are limited, only a reasonable subset of parameter intervals and boundary conditions were considered. The goal of the numerical calculations is consequently to make qualitative assessments rather than providing absolute values comparable to measurement data. For this reason, the simulation parameters are mainly chosen to serve the performance and stability of MALTE instead of representative values of a real storage ring. Nevertheless, most of them are still based on the values of the DELTA parameters, as can be seen in Tab. 4.1.

As mentioned before, synchrotron radiation effects are neglected and, thus, the reference particle should not be accelerated in the cavity, the synchronous phase is set to $\phi_{\mathrm{s}} = \pi$. The modulation frequency f_{mod} has to be determined for the virtual ring, since it depends on the synchrotron frequency. At DELTA, the modulation frequency during user operation is usually set to slightly below twice the synchrotron frequency. This value is used in the calculations, but will be further investigated in Chapter 5.5. For this purpose, a simulation was done with neither RF phase modulation nor wake field effects to determine the synchrotron frequency of the virtual ring and define f_{mod}.

Even though MALTE is capable of using arbitrary fill patterns, only one bucket was filled in the following calculations due to limited memory capacity and to decrease the runtime. This way, only one coupled oscillator exists setting the investigated coupled-bunch mode to the fundamental mode with $\mu = 0$. In addition, this requires long-range wake fields and, thus, a high quality factor of the impedance structure.

To meet these requirements, Q_{r} and R_{s} should be chosen as high as possible within a reasonable range. For a higher-order mode of a normal conducting cavity, like the DELTA cavity, a quality factor of the order of magnitude of $Q_{\mathrm{r}} \approx 1 \times 10^5$ and a shunt impedance around $R_{\mathrm{s}} \approx 5 \times 10^6\,\Omega$ are reasonable. This also helps to improve the performance of MALTE, since high values of Q_{r} and R_{s} lead to high growth rates τ_{G}^{-1} values and, therefore, to fast-rising phase-space coordinates limiting the necessary number of turns n_{t}. T

Table 4.1.: Most important parameters used in the first simulation.

Parameter	Symbol	Value
cavity voltage	$\hat{U}$	350 kV
RF frequency	f_{RF}	500 MHz
harmonic number	h	192
ring length	L_0	115.4 m
momentum compaction factor	α	4.9×10^{-3}
synchronous phase	ϕ_{s}	π
number of particles per bunch	N_{ppb}	10000
number of bunches	N_{b}	1
mode number	μ	0
quality factor (impedance structure)	Q_{r}	1×10^5
shunt impedance (impedance structure)	R_{s}	5 MΩ
initial bunch length	σ_{T}	1 ps
initial energy spread	σ_{E}	1×10^{-10} eV
Number of turns	n_{t}	20000

In addition, the occupied phase-space volume is expected to grow during the calculations due to the excitation of coupled-bunch instabilities. In order to be able to calculate a large number of turns without meeting the termination criterion for δt, presented in Chapter 4.1, the initial value for the bunch length $\sigma_{\mathrm{T}} = 1$ ps and the energy spread $\sigma_{\mathrm{E}} = 1 \times 10^{-10}$ eV are chosen to be relatively small compared to the values of DELTA.

The long range of the wake fields due to the high quality factor in combination with the short bunch length justifies the first-order approximation of one-particle bunches when calculating wake field effects, since the bunch length is short compared to the wavelength of the wake field. While the bunch passes the impedance structure, the wake field inside the bunch can be approximated to be constant and thus rendering the need to recalculate the wake field for every single particle superfluous.

4.3. First Results and Code Validation

As a first study, one bunch with $N_{\mathrm{ppb}} = 10000$ is tracked through the ring with RF phase modulation disabled (modulation amplitude $\eta = 0$) for $n_{\mathrm{t}} = 20000$ turns. The main parameters used for this simulation are shown in Table 4.1. The phase space trajectory of one particle, as well as the rms-value of δE and the δt-coordinate of the center of mass of the bunch are plotted as a function of the turns in Fig. 4.1 together with the value of

the wake field inside the impedance structure. Both phase-space coordinates grow exponentially due to wake fields stimulating coupled-bunch instabilities. The wake field in the impedance structure also contains all information about the excited coupled-bunch modes and grows in the same way (given by the first element of the "charge vector" $\vec{q}_n$).

To investigate coupled-bunch effects, the growth rate τ_{G}^{-1}, introduced in Section 2.4.1 and 2.4.2, has to be determined. For this purpose, an exponential function in the form

$$f(x) = \exp\{b(x+a)\} + c$$

is fitted to the envelope of the wake field with the fit parameters a, b and c.

With the ability to track particles through a virtual storage ring and successfully determine

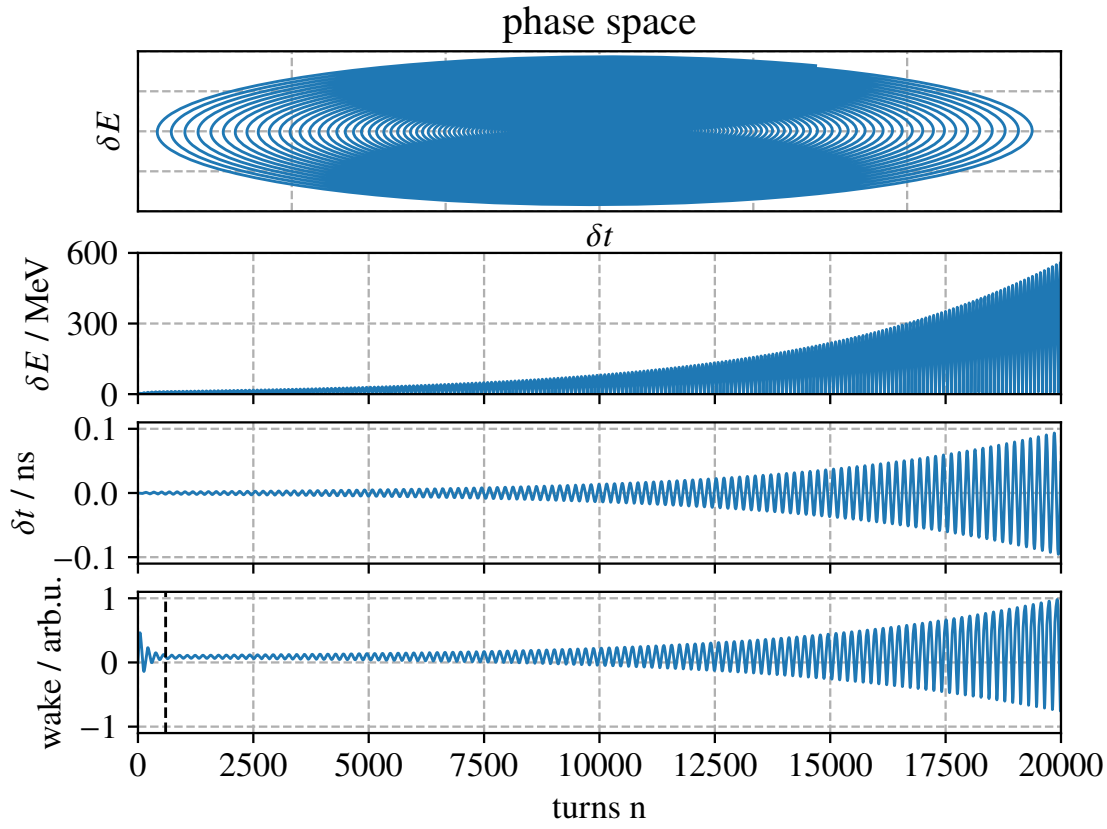

Figure 4.1.: Exemplary results of $N_{\mathrm{ppb}} = 10\,000$ particles tracked through the ring over $n_{\mathrm{t}} = 20\,000$ turns without RF phase modulation. The phase space trajectory of a single particle is shown. Additionally, the rms value of the δE-coordinate as well as the δt-coordinate of the center of mass of the bunch are shown separately as a function of the turn number. The value of the wake field inside the impedance structure shows a transient effect at the beginning, which is cut off to prevent it from distorting exponential fits (highlighted by a dashed black line).

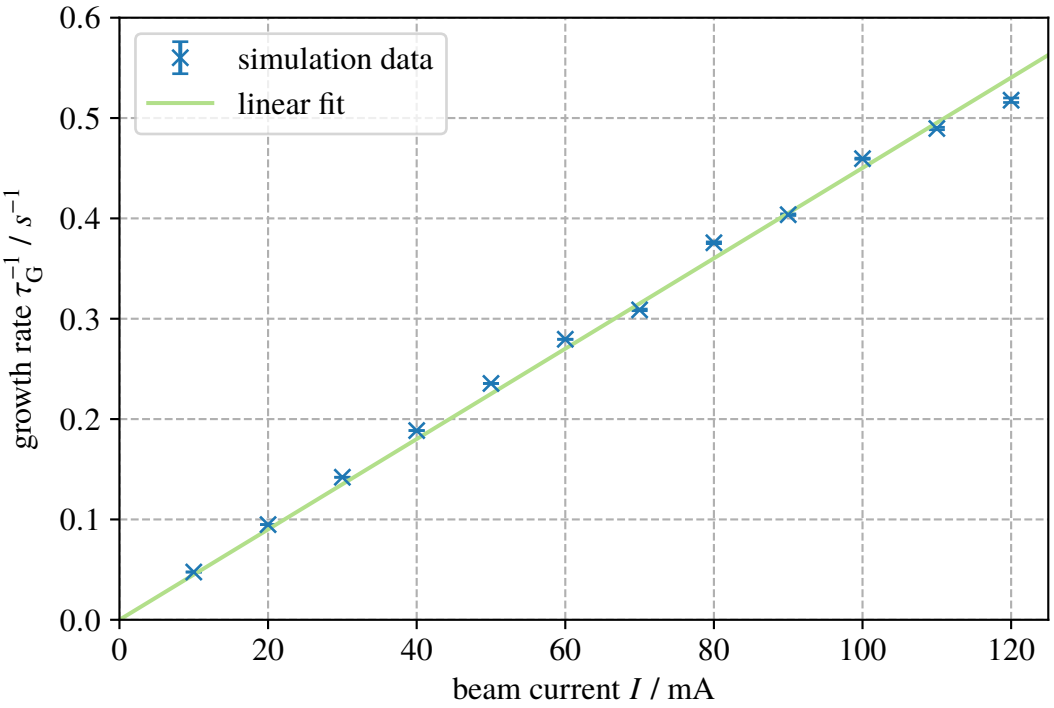

Figure 4.2.: Growth rate τ_G^{-1} as a function of the beam current I (blue markers with vertical error bars). The error bars represent the standard deviation of the individual exponential fits. A linear fit (green line) highlights the linear dependence of τ_G^{-1} on I.

coupled-bunch growth rates, a second study is done analyzing τ_G^{-1} as a function of the beam current I without RF phase modulation. This is also used to validate MALTE, since the dependence of τ_G^{-1} on I is well known by analytical calculations (see Section 2.4.2).

In reality, the beam current is changed by injecting more electrons into the ring. However, this could lead to excessive calculation times in the simulation. Therefore, the beam current is changed in the simulation by altering the charge of every particle q, keeping N_{ppb} constant.

The beam current is swept from $I_0 = 10\,\mathrm{mA}$ to $I_{\mathrm{max}} = 120\,\mathrm{mA}$ and the instability growth rate is determined in every step, as shown in Fig. 4.2. Linear regression is used to fit a first-order polynomial function in the form

$$f(I) = a \cdot I$$

with the fit parameter

$$a = (4.503 \pm 0.042) \times 10^{-3}\,\mathrm{s}^{-1}\,\mathrm{mA}^{-1}$$

to the data. The results are in good agreement with the proportional relation between growth rate τ_G^{-1} and beam current I, as expected from Eq. (2.30). That validates that MALTE provides realistic results and can be used for further studies.

4.4. Dependence of Coupled-Bunch Growth Rates on the Modulation Amplitude

Investigating the interaction of RF phase modulation and coupled-bunch instabilities, the most interesting correlation is the dependence of the growth rate τ_G^{-1} on the modulation amplitude η. The tracking code MALTE is used to analyze this correlation as follows [75].

To determine the growth rate, exponential functions are fitted to the rms value of δE, to the mean of δt and to the value of wake field (given by the first element of $\vec{q}_n$), as already mentioned in Chapter 4.3. The results of the three fits are basically the same, while the wake field turns out to be the most robust choice, especially in the presence of RF phase modulation. This can be understood by the fact, that the wake field is gathered by the first element of the charge vector $\vec{q}_n$. Considering the analogy to an RLC-circuit described by Eq. (2.24), the first entry contains no information about the phase, which is stored in the second entry. While the exponential growth of the phase-space coordinates is distorted by the phase modulation, the wake field is almost unperturbed by this effect. For this reason, the wake field is used for determining the growth rate.

One particle bunch with $N_{\mathrm{ppb}} = 10\,000$ is tracked over $n_t = 20\,000$ turns with the parameters listed in Table 4.1. The beam current is chosen to be $I = 110\,\mathrm{mA}$ to maximize τ_G^{-1} in order to achieve good exponential fits. This is especially important for high modulation amplitudes since, according to Section 2.4.3, the growth rates decreases when η increases. The synchrotron frequency was acquired by evaluating the oscillation frequency of the phase space coordinates and has a value of $f_s = 15.3\,\mathrm{kHz}$.

Repeating this simulation with identical start parameters for different modulation amplitudes from $\eta_0 = 0\,\mathrm{deg}$ to $\eta_{\max} = 3\,\mathrm{deg}$ in steps of $0.2\,\mathrm{deg}$ yields exponentially growing results

similar to Fig. 4.1. The results are shown in Fig. 4.3.

Eventually, an elementary function shall be assigned that describes the relation between η and τ_G^{-1}. A reasonable function with a low number of parameters is a parabola with its maximum at the vanishing modulation amplitude and two free parameters. In this case, the second-order polynomial function

$$\tau_G^{-1}(\eta) = a \cdot \eta^2 + b$$

is chosen with the least-square values

$$a = (-2.227 \pm 0.010) \times 10^{-2}\,\mathrm{ms}^{-1}\,\mathrm{deg}^{-2}$$
$$b = (4.942 \pm 0.004) \times 10^{-1}\,\mathrm{ms}^{-1}.$$

These results are tested further in experimental studies at the DELTA storage ring as shown in the following chapter.

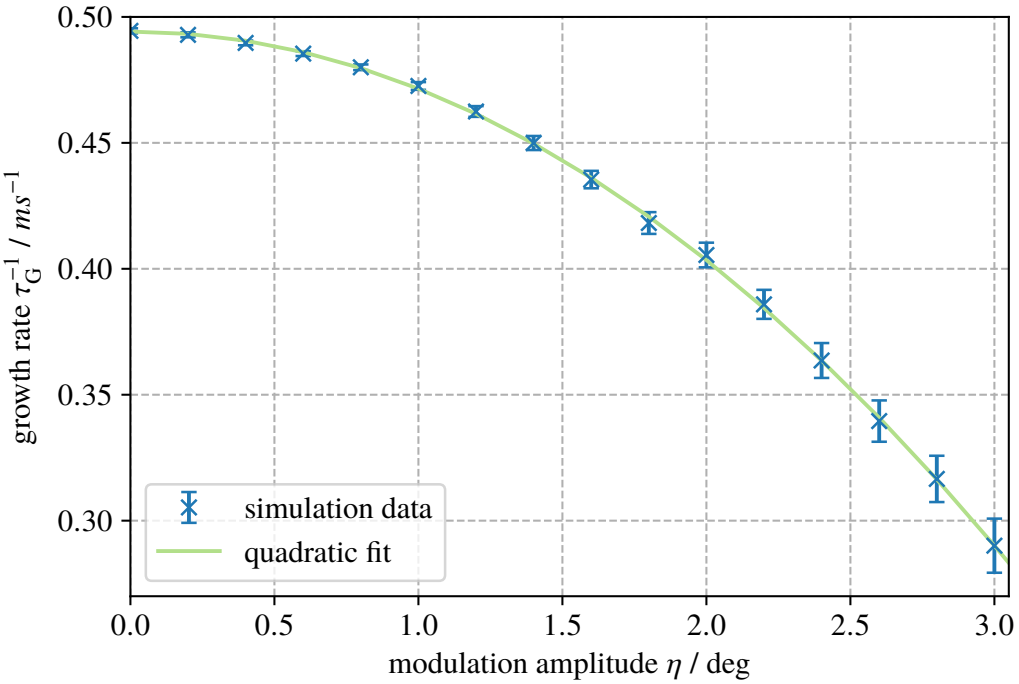

Figure 4.3.: Growth rate as a function of the phase modulation amplitude (blue markers with vertical error bars). A second-order polynomial function is fitted to the data (green).

5. Experimental Studies

In order to analyze the interaction of coupled-bunch instabilities and RF phase modulation, the growth rates of coupled-bunch modes as a function of the modulation amplitude were measured and compared to the simulation results of Chapter 4.4. For this purpose, the phase shift applied to the beam in the accelerating cavity due to RF phase modulation has to be known, as well as the modulation frequency. At DELTA, the modulation frequency is directly tunable, but the modulation amplitude is set via an input voltage U_C at the phase modulation system (see Chapter 3) without precise information about the phase-shift applied to beam. Therefore, measurements were done to obtain the phase shift inside the cavity as a function of the input voltage U_C, which are presented in Section 5.2.

In addition, the bunch-by-bunch feedback system is used to measure the turn-by-turn bunch oscillation, shown in Section 5.3, which can be used to determine coupled-bunch growth rates. For this purpose, a well-known method has been commissioned and thoroughly tested at DELTA [76] which is described in Section 5.4.

Unfortunately, this measurement method is not applicable in the presence of RF phase modulation with high modulation amplitudes, as shown in Chapter 5.4. Hence, a new method has been developed and is presented in Section 5.5. It is used to analyze coupled-bunch growth rates as a function of the modulation amplitude as described in Section 5.5.

At last, additional studies are shown in Section 5.6, which were made to improve the user operation at DELTA with the knowledge gained by the previous measurements.

5.1. Optimum RF Phase Modulation Frequency

Before performing additional studies with RF phase modulation, the optimum modulation frequency has to be found to maximize the investigated effects. For this purpose, the bunch-by-bunch feedback system is used to measure the strength of beam instabilities as follows.

When a longitudinal instability occurs, each bunch starts to oscillate with the synchrotron frequency f_s leading to an increase of the spectral power $P(f_s)$ in the single-bunch spectrum. With the bunch-by-bunch feedback system, the longitudinal bunch positions of all bunches are collected individually once per revolution. Applying a fast Fourier transform at each bunch individually, the collected data yields the single-bunch spectra. By adding up the single-bunch spectra of all bunches, the resulting mean spectral power at the synchrotron frequency $P_\Sigma(f_s)$ is an indicator for the strength of the beam instability [46]. Although all information about the mode number is lost this way, the results are sufficient to

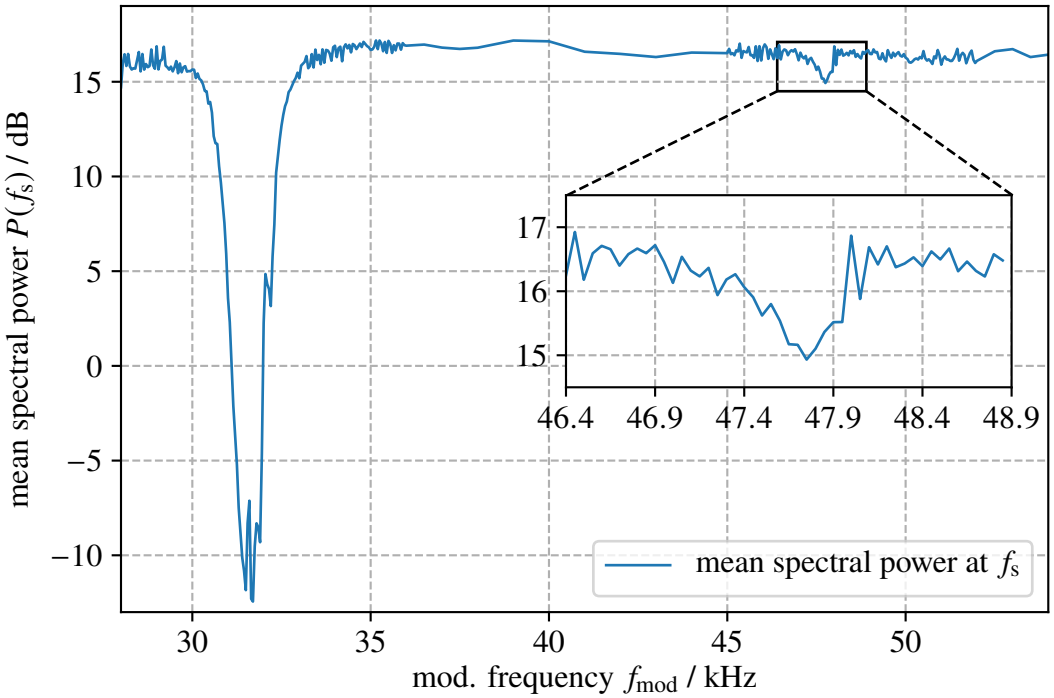

Figure 5.1.: Spectral power $P_\Sigma(f_s)$ at the synchrotron frequency $f_s = 16.05\,\text{kHz}$ as a function of the modulation frequency f_{mod}. The suppression of coupled-bunch instabilities is maximized at $f_2 = 31.60\,\text{kHz}$. The effect is also partly visible at $f_3 = 47.75\,\text{kHz}$ as highlighted by the zoomed section around that frequency.

detect the optimum modulation frequency.

To investigate this, the input voltage is set to $\hat{U}_C = 1.5\,\mathrm{V}$ and the modulation frequency f_{mod} is swept from 28 kHz to 54 kHz. In each step, the mean spectral power $P_\Sigma(f_s)$ at $f_s = 16.05\,\mathrm{kHz}$ is acquired as described before. The results in Fig. 5.1 show two local minima. The deepest minimum is at $f_2 = 31.60\,\mathrm{kHz}$, which is slightly below twice the synchrotron frequency showing that the effect of RF phase modulation maximizes at slightly below the second integer harmonic, as already shown at other accelerators (e.g. [24, 55]). In addition, the modulation frequency can also be set to $f_3 = 47.75\,\mathrm{kHz}$, i.e., slightly below three times the synchrotron frequency, like at other facilities (e.g. [39, 77]), but the effect is significantly smaller at DELTA [78].

Conspicuously, the right-hand slope is sharper than the left-hand side, specifically at the third harmonic. A possible explanation for this asymmetry will be discussed in Section 5.6.2.

5.2. Phase Shift Applied in the Accelerating Cavity

As shown in Section 3.2, the phase modulation system at DELTA is tuned by a control voltage $U_C = \hat{U}_C \sin(\omega_{mod} t)$. While ω_{mod} is the modulation frequency, its amplitude $\hat{U}_C$ is transformed to the modulation amplitude $\eta(\hat{U}_C)$ by the phase shifter module leading to

$$U_{mod} = \hat{U}_{mod} \sin\left(\omega_{RF} t + \eta(\hat{U}_C) \sin(\omega_{mod} t) + \phi_{DC}\right), \tag{5.1}$$

with the modulation signal U_{mod} and its amplitude $\hat{U}_{mod}$ as introduced in Eq. (3.1). To determine the phase shift applied to the beam as a function of U_C, measurements were performed with a spectrum analyzer [79] in two steps. Firstly, the output signal of the phase modulation system was investigated. Afterwards, the signal inside the cavity was measured with a pickup probe. Both probe positions are highlighted in Fig. 3.2.

As seen in Section 2.1.3, the phase shift of a phase-modulated sinusoidal signal can be determined by measuring the amplitudes of the sidebands of the spectrum and comparing them with spectra calculated with Bessel functions. For this purpose, spectra with a given phase shift η were calculated using Eq. (2.9) and fitted to the measurement data with η being the only fit parameter, since ω_{mod} and ω_{RF} are known. This way, the phase shift applied to the beam in the measurement were determined.

In the experiment, several spectra were measured for different input voltage amplitudes $\hat{U}_C$

and the Bessel function method was used in every iteration to determine η. An exemplary spectrum is shown in Fig. 5.2 together with the calculated sideband amplitudes for the best fitting value of η. The measured sidebands are asymmetric and the higher-order sidebands are significantly larger than the calculated ones. The reason for these differences is the way how the phase modulation system operates. Looking at the characteristic curve of the system, shown in Fig. 3.2, it can be seen, that the operating range is not linear which makes the modulation not perfectly sinusoidal. In this case, it is not accurate to use Bessel functions to determine the modulation amplitude.

To obtain a better model, the output signal of the phase modulator is considered to be

$$U_{\mathrm{mod}} = \hat{U}_{\mathrm{mod}} \sin\left(\omega_{\mathrm{RF}} t + \phi_{\mathrm{PS}}\left(U_{\mathrm{C}}\right)\right)$$

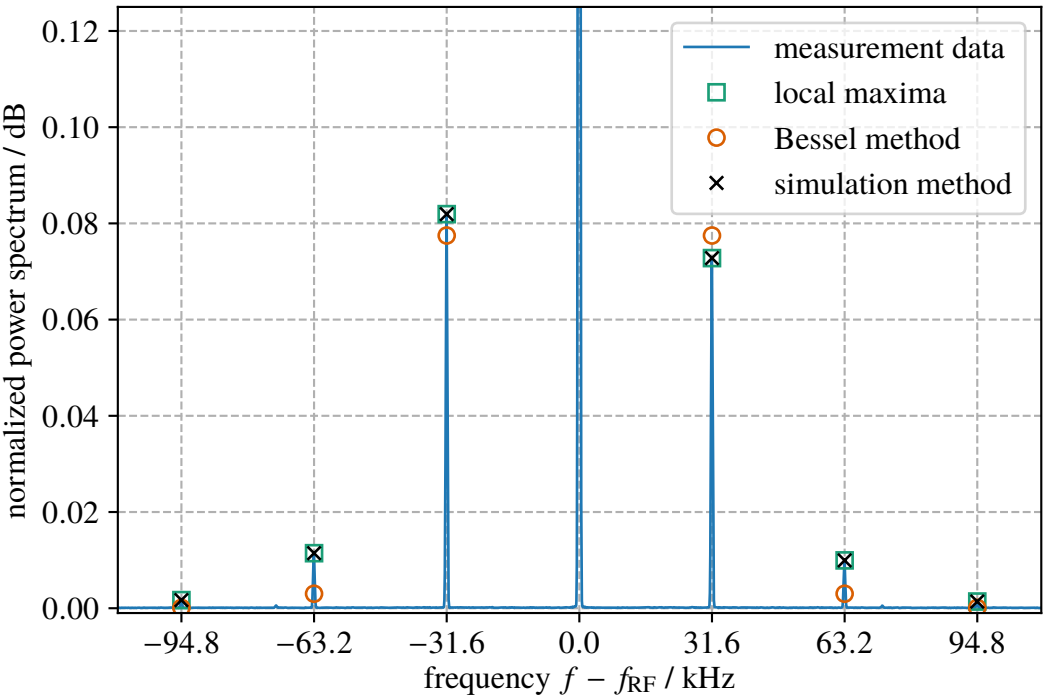

Figure 5.2.: Measured spectrum of the output of the phase shift module in comparison with the calculated sidebands using Bessel functions (see Eq. (2.9)) and the simulated sidebands with a nonlinear phase shift. The spectrum is normalized such that the maximum of the center frequency has a value of 1 dB. For this measurement, the amplitude of the control voltage was set to $\hat{U}_{\mathrm{C}} = 1.5\,\mathrm{V}$ and the modulation frequency was $f_{\mathrm{mod}} = 31.6\,\mathrm{kHz}$.

with the phase shift ϕ_{PS} applied by the phase modulation system depending on

$$U_{\mathrm{C}} = \hat{U}_{\mathrm{C}} \sin\left(\omega_{\mathrm{mod}} t\right) + U_{\mathrm{DC}} \tag{5.2}$$

instead of just on the amplitude $\hat{U}_{\mathrm{C}}$. To evaluate the measured data with this assumption, a numerical simulation was developed to calculate frequency spectra generated by the phase modulation system. For this purpose, the characteristic curve of the phase modulation system [79] is interpolated by cubic splines giving a continuous function of the phase shift ϕ_{sim} (see Fig. 3.2) depending on Eq. (5.2). With this function, a 500 MHz carrier-signal can be modulated with arbitrary modulation amplitude and frequency. Using a fast Fourier transformation generates the spectrum, which is subtracted from the measured spectrum and the sum of squared residuals $\Delta\Gamma$ is calculated. To find the phase shift of the measurement ϕ_{meas}, ϕ_{sim} is altered until the minimum of $\Delta\Gamma$ is found, so that $\phi_{\mathrm{sim}} \approx \phi_{\mathrm{meas}}$.

The sideband amplitudes gathered by this method are also shown in Fig. 5.2 for the exemplary spectrum. Both, the asymmetry and the larger values of the higher-order sidebands are reproduced by the simulation. The modulation amplitude η, which equals the maximum phase shift (see Section 2.1.3), can, thus, be determined appropriately.

In addition, because of the finite bandwidth of the accelerating cavity, the phase shift inside the cavity is expected to be smaller than the phase shift at the output of the phase modulation system, as mentioned in Chapter 3.2. To determine the reduction of the phase shift by the cavity, the quality factor of the cavity is also measured with the RF phase modulation system. This method has the advantage over conventional measurement methods with vector network analyzers (see appendix A.2), that it can be used while the accelerator is in operation and without breaking the vacuum.

The modulation frequency was swept from 0 kHz to 35 kHz with $\hat{U}_{\mathrm{C}} = 1.5\,\mathrm{V}$ and the spectrum analyzer was used to measure the spectra at the pickup probe inside the cavity. The amplitude of the first sideband on both sides of ω_{RF} of each spectrum is plotted against the modulation frequency resulting in the resonance curve of the cavity as shown in Fig. 5.3. A Cauchy distribution of the form

$$F(f) = \frac{A}{1 + \left(2Q_{\mathrm{L}}\left(f - f_{\mathrm{RF}}\right)/f_{\mathrm{RF}}\right)^2} + u$$

is fitted to the data with the Amplitude A, the center frequency f_{RF}, the loaded quality factor

Q_L and the background offset u resulting in the fit parameters

$$\begin{aligned} A &= (0.778 \pm 0.012)\,\mathrm{dB} \\ f_{RF} &= (499.8168 \pm 0.0001)\,\mathrm{MHz} \\ Q_L &= 11\,286 \pm 258 \\ u &= (0.211 \pm 0.013)\,\mathrm{dB}. \end{aligned}$$

The cavity was designed to have a quality factor of $Q_0 = 36\,000$ with a coupling factor of $\kappa = 2.0$ [80–82]. This results in a loaded quality factor $Q_L = 12\,000$ according to Eq. (2.7). These values are additionally verified in a conventional measurement presented in appendix A.2 and are in good agreement with the results gathered with the phase modulation system.

The dependence of the phase shift at the output of the phase modulation system ϕ_{PS} as well

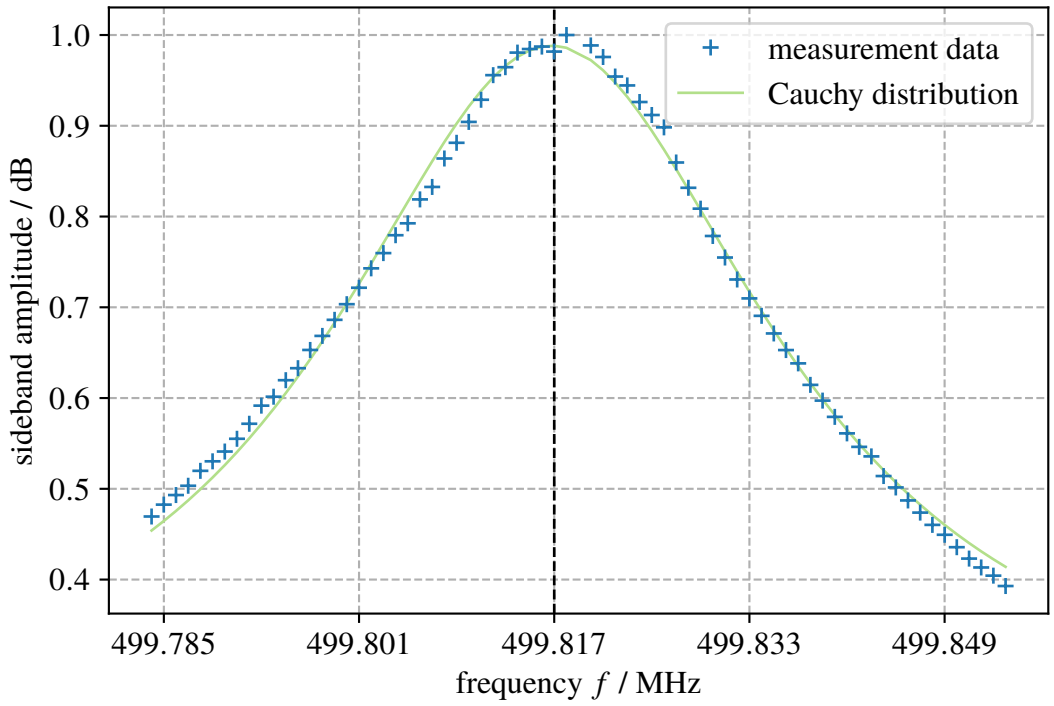

Figure 5.3.: Resonance curve of the DORIS-type cavity installed at DELTA centered at $f_s = 499.817\,\mathrm{MHz}$, measured by altering the modulation frequency with $\hat{U}_C = 1.5\,\mathrm{V}$. Each blue marker represents the amplitude of a sideband in the corresponding measured spectrum. A Cauchy distribution is fitted to the measured data (solid green).

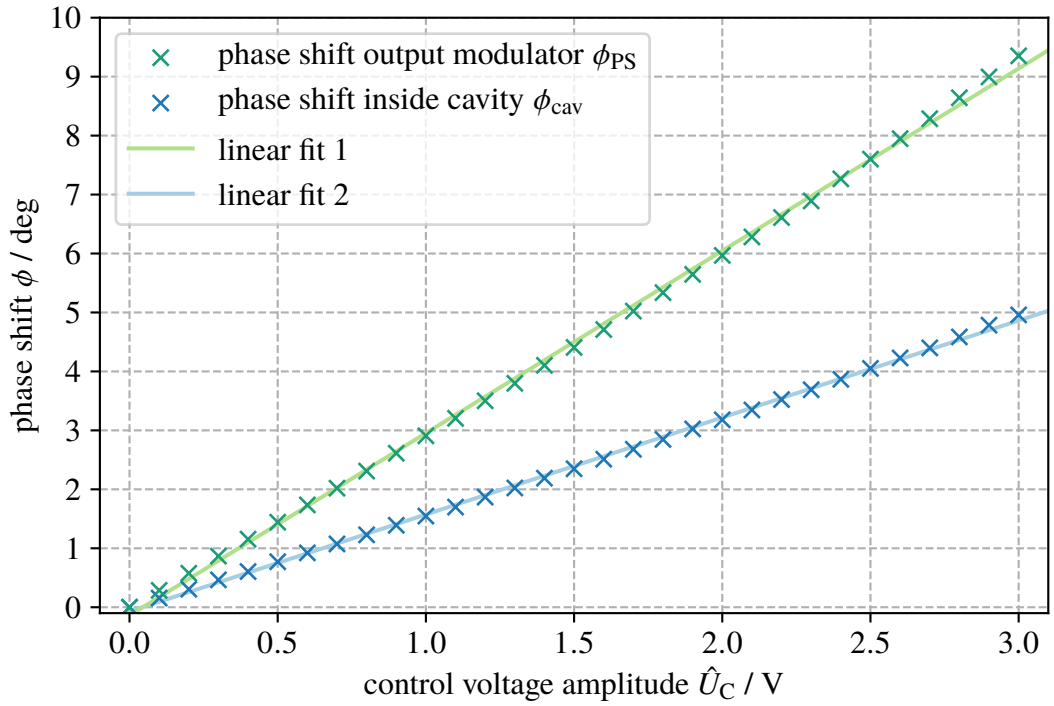

Figure 5.4.: Phase shift as a function of the control voltage amplitude $\hat{U}_C$ at the output of the phase modulation system (blue) and inside the accelerating cavity (black) together with corresponding linear fits.

as at the pickup probe in the accelerating cavity ϕ_{cav} on the input voltage amplitude $\hat{U}_C$ was analyzed by sweeping $\hat{U}_C$ from 0 V to 3 V in steps of 0.1 V. The modulation frequency was set to its optimum value $f_{mod} = 31.6\,\text{kHz}$. The results are shown in Fig. 5.4. A linear function in the form

$$\Phi_i\left(\hat{U}_C\right) = a_i \cdot \hat{U}_C + b_i$$

with the fit parameters

$$a_{PS} = (3.09 \pm 0.02)\,\text{deg/V} \qquad b_{PS} = (-0.14 \pm 0.03)\,\text{deg}$$
$$a_{cav} = (1.64 \pm 0.01)\,\text{deg/V} \qquad b_{cav} = (-0.07 \pm 0.02)\,\text{deg}$$

is used to highlight the linear dependence of the phase shifts on $\hat{U}_C$.

The phase shift in the cavity is constantly smaller than ϕ_{PS} by a factor of $a_{cav}/a_{PS} = 0.53$. With the measured quality factor of the cavity, the reduction factor at $f_s = 31.6\,\text{kHz}$ is $\phi_{cav}/\phi_{PS} = 0.47$, which is in good agreement with the previous results. The small discrepancy can be understood by the fact that the phase modulation system has a finite band-

width as well, which narrows the measured resonance curve of the cavity leading to a smaller bandwidth $\Delta\omega$ and, hence, to a smaller damping factor.

Additionally, the maximum phase shift applied to the electron beam at DELTA in the monitored regime $\hat{U}_C \in [0,3]\,\mathrm{V}$ is determined to be $\phi_{max} \approx 4.91\,\mathrm{deg}$. During user operation, the input voltage is usually set to 0.7 V which equals a phase shift of $\phi_{user} \approx 1.08\,\mathrm{deg}$.

5.3. Data Acquisition with the Bunch-by-Bunch Feedback System

To be able to evaluate coupled-bunch instability growth rates, the bunch-by-bunch feedback system is used to acquire the turn-by-turn data of all bunches separately, as described in Chapter 3.3. Since this thesis focuses on longitudinal beam dynamics, only the longitudinal processor unit of the system is used for all measurements.

The Dimtel bunch-by-bunch feedback system comes with a data acquisition tool that stores the longitudinal position of every bunch for roughly 65 000 turns. To characterize coupled-bunch instabilities, it is useful to convert the data to the even-fill eigenmode basis (EFEM[1]), resulting in h signals for the different oscillating modes of the beam [64]. For this purpose, a bandpass filter is used at the synchrotron frequency to improve the signal-to-noise ratio. Afterwards, the mode spectrum is calculated based on the scheme described in [46, 83–85]. First, the analytic signal for each bunch is derived by a Hilbert transformation of the form

$$\mathrm{H}\{x(t)\}(t) = \frac{1}{\pi}\int_{-\infty}^{\infty}\frac{x(\tau)}{t-\tau}d\tau.$$

The analytic signal $u(t)$ is defined as

$$u(t) = x(t) + i\,\mathrm{H}\{x(t)\}(t)$$

and describes the envelope, or instantaneous amplitude, of the oscillation signal [86]. For a given oscillation coordinate of bunch k

$$x_n^k = a_n^k \cos\left(2\pi n D\nu + \phi_n^k\right),$$

[1] Even filling pattern means, that it has rotational symmetry. For N_b filled bunches and h buckets, rotating the fill pattern by h/N_b buckets leaves the same buckets filled [83].

with magnitude a_n^k, phase ϕ_n^k, the sample number n, downsampling factor D and longitudinal tune ν, the analytic signal

$$u_n^k = a_n^k \exp\left\{i\left(2\pi n D\nu + \phi_n^k\right)\right\}$$

is derived. By using discrete Fourier transformations of the sequence of analytic signals at each sample, the modal phase space coordinate U_n^μ of the μ-th EFEM at sample n is given by

$$U_n^\mu = A_n^\mu \exp\left\{i\left(2\pi n D\nu + \phi_n^\mu\right)\right\} = \sum_{k=0}^{G-1} u_n^k \exp\left\{-i\frac{2\pi\mu k}{G}\right\}$$

with G being the ratio of the harmonic number to the bunch spacing, A_n^μ being the magnitude and ϕ_n^μ being the normalized angle. The absolute value of U_n^μ represents the envelope of the mode amplitudes. If the bunch filling is not even, the calculated eigenmodes of the beam are linear combinations of EFEMs.

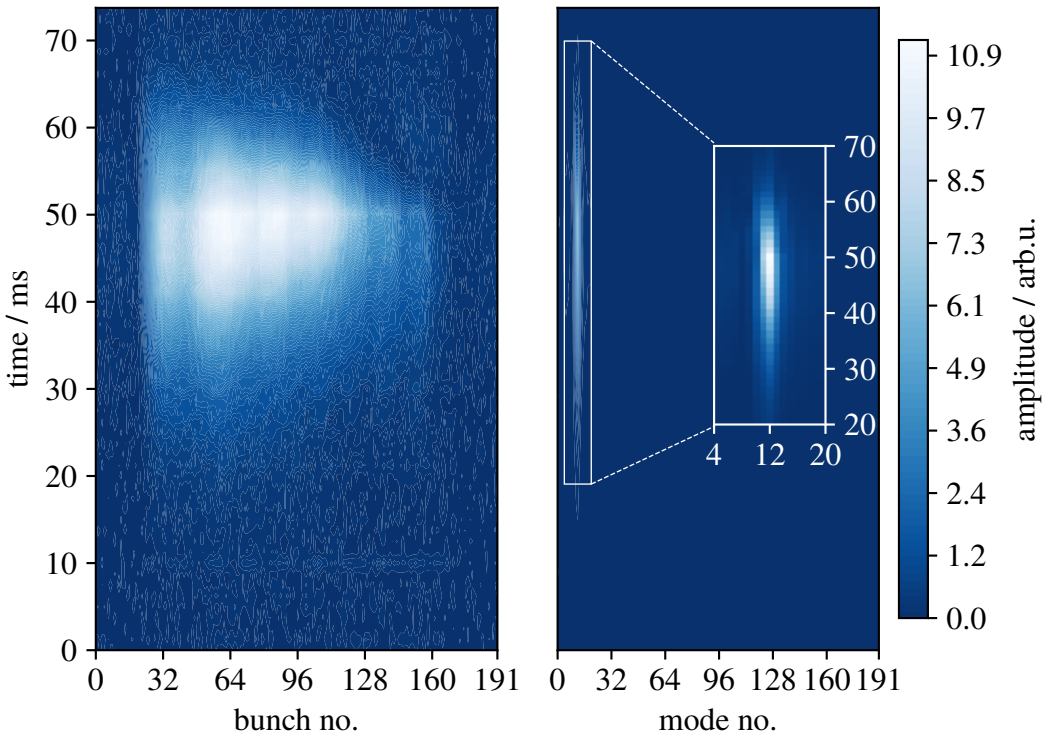

Figure 5.5.: Output of the data acquisition tools provided by Dimtel [64]. **Left:** Envelope of longitudinal position signal of all 192 bunches. **Right:** Corresponding signal of the 192 coupled-bunch modes of the beam. While mode $\mu = 12$ is the most dominant mode, the modes next to it are present due to an uneven fill pattern. To highlight that, the modes 4 to 20 are additionally shown in a zoomed section.

The envelope of the oscillation signal as well as the mode amplitudes, given by $\left|U_n^\mu\right|$, are shown in Fig. 5.5. For this exemplary measurement, 144 buckets were filled at DELTA with a beam current $I \approx 75\,\mathrm{mA}$. Coupled-bunch instabilities arise and vanish during the measurement, leading to the growth and afterwards the damping of the oscillation magnitude of all bunches. On the right hand, side the transient behavior of each mode is shown. Although only mode $\mu = 12$ is responsible for the bunch oscillations, the adjacent modes are also present in the data, which is caused by the uneven fill pattern and therefore an artifact of the EFEM approximation.

5.4. Determination of Coupled-Bunch Growth and Damping Rates

A method to measure growth and damping rates of coupled-bunch modes has been commissioned and thoroughly tested at DELTA without RF phase modulation [46]. For this approach, the bunch-by-bunch feedback system is used to acquire the data as described in the previous chapter.

For an acquisition time of $t_{\mathrm{acq}} = 100\,\mathrm{ms}$, the longitudinal center-of-mass position of every bunch was recorded and the data was converted to the even-fill-eigenmode basis. To analyze coupled-bunch growth and damping rates, so-called grow-damp measurements were performed. For these measurements, the bunch-by-bunch feedback system was used to excite and/or damp the beam to achieve a beam signal, which starts growing and damps down afterwards, as shown in Fig. 5.5, or vice versa. This also includes measurements, in which the data acquisition window does not contain the whole process. For example, if the data acquisition stops at the maximum oscillation amplitude, only a growing signal is seen in the data. Generally, two types of grow-damp measurements were performed depending on the beam current as follows.

If the beam current I is lower than the instability threshold I_{thr} (see Section 2.4.1), the damping rate due to synchrotron radiation τ_{D}^{-1} is higher than the highest coupled-bunch growth rate τ_{G}^{-1} and the electron beam is stable with $\tau^{-1} < 0$, according to Chapter 2.4. In this case, the bunch-by-bunch feedback was used to excite the beam by positive feedback for a period of time t_{g}, called growth time. Afterwards, the excitation was turned off and the excited oscillations damped down due to synchrotron radiation damping. Using positive feedback gives rise to the most dominant coupled-bunch mode, which usually is

mode $\mu = 12$ at DELTA. For studying other modes, the built-in frequency generator of the bunch-by-bunch feedback system (drive) can be used to excite one specific mode with the corresponding frequency [87]. Either way, the electron beam starts damping down exponentially according to Eq. (2.28) at $t \geq t_g$. The factor $\tau_{fit}^{-1} = \tau^{-1}$ was evaluated via fitting an exponential function to the mode signal during the damping period. An example of such a measurement including the exponential fit is shown in the left hand side of Fig. 5.6.

For beam currents higher than the instability threshold $I > I_{thr}$, coupled-bunch instabilities rise due to excitation by wake field effects leading to $\tau^{-1} > 0$. In this case, the bunch-by-bunch feedback system is used to damp the beam using negative feedback. At the start of the measurement, the bunch-by-bunch feedback was turned off for a period of time t_{off} and the most dominant mode started to rise exponentially. The factor τ_{fit}^{-1} was also determined by exponential fitting, but this time on the rising slope (see the right hand side of Fig. 5.6).

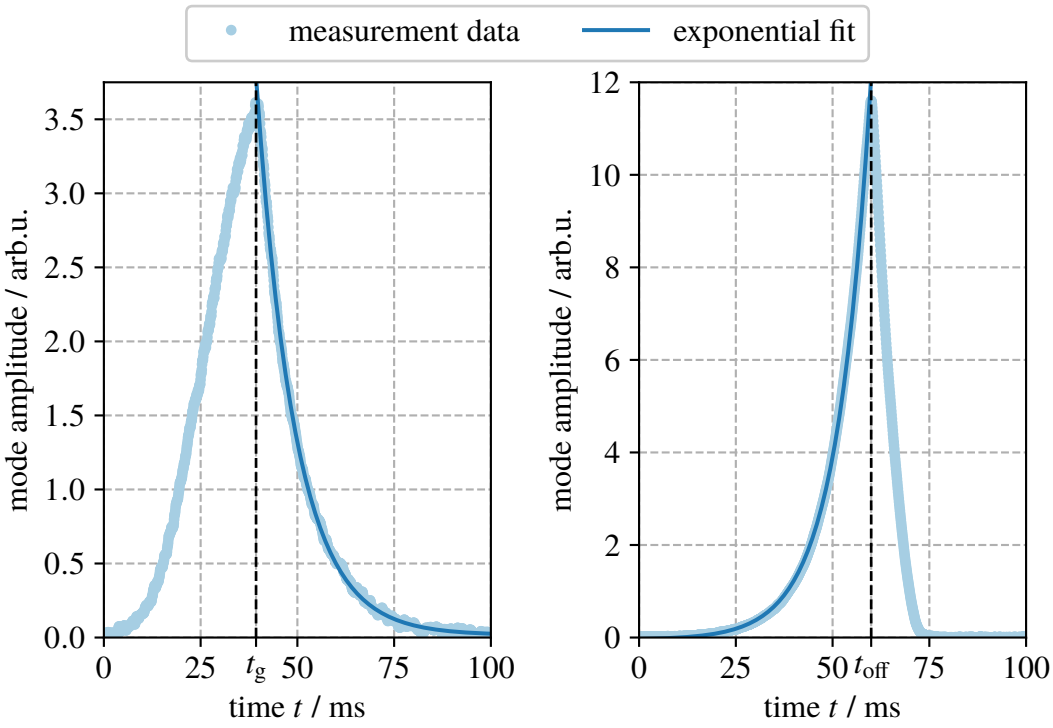

Figure 5.6.: Grow-damp measurements at DELTA. **Left:** The beam current I is below the instability threshold I_{thr}. Positive feedback was applied from $t = 0$ to $t = t_g$ to excite the beam. Afterwards the feedback was turned off and the beam damped down. The factor τ_{fit}^{-1} was determined by fitting an exponential function to the damping part. **Right:** The beam current is well above the instability threshold. This time, the feedback was turned off from $t = 0$ to $t = t_{off}$ and the factor τ_{fit}^{-1} was determined by fitting an exponential function to the growing part.

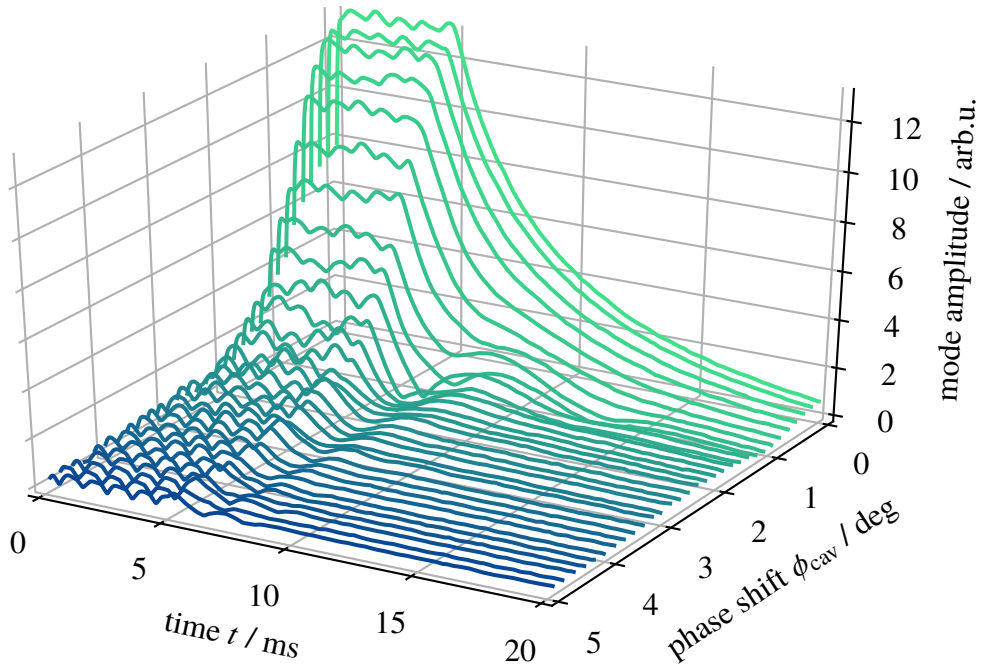

Figure 5.7.: Grow-damp mode signals of mode $\mu = 12$ at approximately 40 mA for different phase shifts ϕ_{cav}. Only the mode signals for phase shifts $\phi_{cav} < 0.7$ deg decrease exponentially.

If the signal reaches saturation, the data used for fitting has to be cut before the inflection point. Alternatively, the time t_{off} can be chosen small enough to prevent the mode from growing into saturation as in Fig. 5.5. Studying other modes than the most dominant mode $\mu = 12$ is more complicated below the instability threshold, but achievable by pre-exciting the particular mode with the drive generator, as presented in [46, 87].

To test whether these techniques are applicable in the presence of RF phase modulation at DELTA, several grow-damp measurements for mode $\mu = 12$ were performed for different modulation amplitudes. The beam current was set to $I \approx 40\,\text{mA}$, which is well below the instability threshold [76], so that the first type of grow-damp measurements is used. The synchrotron frequency during the measurement was $f_s = 15.9\,\text{kHz}$. To make sure, that only mode $\mu = 12$ is excited, the drive generator was used to excite the beam with the frequency corresponding to this mode, which is given by

$$f_\mu = \mu f_{rev} + f_s$$

according to Eq. (2.21) with $f_{exc} = f_{12} = 0 \cdot f_{RF} + 12 \cdot f_{rev} + f_s = 31.266\,\text{MHz}$. The modulation

amplitude was swept from $\hat{U}_{\mathrm{C},0} = 0\,\mathrm{V}$ to $\hat{U}_{\mathrm{C,max}} = 3\,\mathrm{V}$ in 30 steps, which equals a phase shift applied to the beam of ϕ_{cav} from 0 deg to 4.91 deg.

The results are shown in Fig. 5.7. While the saturation values in the excitation regime decrease with ϕ_{cav}, the shape of the signals changes in the damping regime for higher phase shifts. This effect can be explained by the fact that RF phase modulation adds an oscillation to the center-of-mass motion of the bunch. The bunch-by-bunch feedback only measures the center-of-mass motion and, thus, detects a convolution of the oscillation arising from RF phase modulation and the exponential damping described by τ^{-1}. This convolution can be seen in the data, especially for phase shift $\phi_{\mathrm{cav}} \gtrapprox 0.7$. Using exponential curves to fit this kind of data is inappropriate [88], i.e., coupled-bunch growth rates cannot be studied in the presence of RF phase modulation with this method, since τ^{-1} cannot be acquired. For this reason, an alternative approach was developed and is presented in the next chapter.

5.5. Investigation of Coupled-Bunch Instabilities in the Presence of RF Phase Modulation

The previous section showed, that the common method utilizing exponential fits cannot be used to determine the growth rate τ^{-1} for high modulation amplitudes. On the other hand, the saturation value Y_{max} of the investigated coupled-bunch mode is inversely related to the modulation amplitude. This effect can be used to determine τ^{-1} below the instability threshold, if the correlation between τ^{-1} and Y_{max} is known. For this purpose, a new method, called the saturation method, was developed using this correlation.

The saturation value Y_{max} represents the equilibrium of the excitation by the frequency generator of the bunch-by-bunch feedback system, synchrotron radiation damping and the growth or damping rate of the potentially occurring coupled-bunch mode. By changing solely RF phase modulation parameters, the excitation parameters as well as synchrotron radiation damping remain untouched, meaning that a change of Y_{max} corresponds to a change of the mode strength. It is important to note, that the common method provides only the factor τ^{-1}, which is a summation of the damping rate due to synchrotron radiation and the growth or damping rate of the mode. This factor is still sufficient to characterize coupled-bunch modes as long as the absolute value is not relevant (for example for trends, parameter sweep, etc.), since the synchrotron radiation damping rate is just a constant offset. This leads to the goal of finding a valid description for the relation between Y_{max} and

τ^{-1}. For this purpose, the measured mode signal $Y(\omega)$ is reconstructed mathematically as follows[2].

In signal processing, the output signal is the result of the convolution of the input signal with the impulse response of the system [68]. In the equilibrium state, the input signal

$$a(t) = A_{\text{exc}} \cdot e^{i\omega_{\text{exc}} t}$$

is the excitation signal of the drive generator of the longitudinal bunch-by-bunch feedback system. The impulse response of the beam is a damped oscillation

$$x(t) = \begin{cases} 0 & \text{for} \quad t < 0 \\ -ie^{\psi t} & \text{for} \quad t \geq 0 \end{cases}$$

with $\psi = i\omega_1 - \tau^{-1}$, the oscillation frequency ω_1 and the rate $\tau^{-1} \geq 0$. Both signals are shown in Fig. 5.8.

The convolution of both signals can be achieved by multiplying the corresponding Fourier

[2] The detailed calculations can be found in the Appendix A.3.

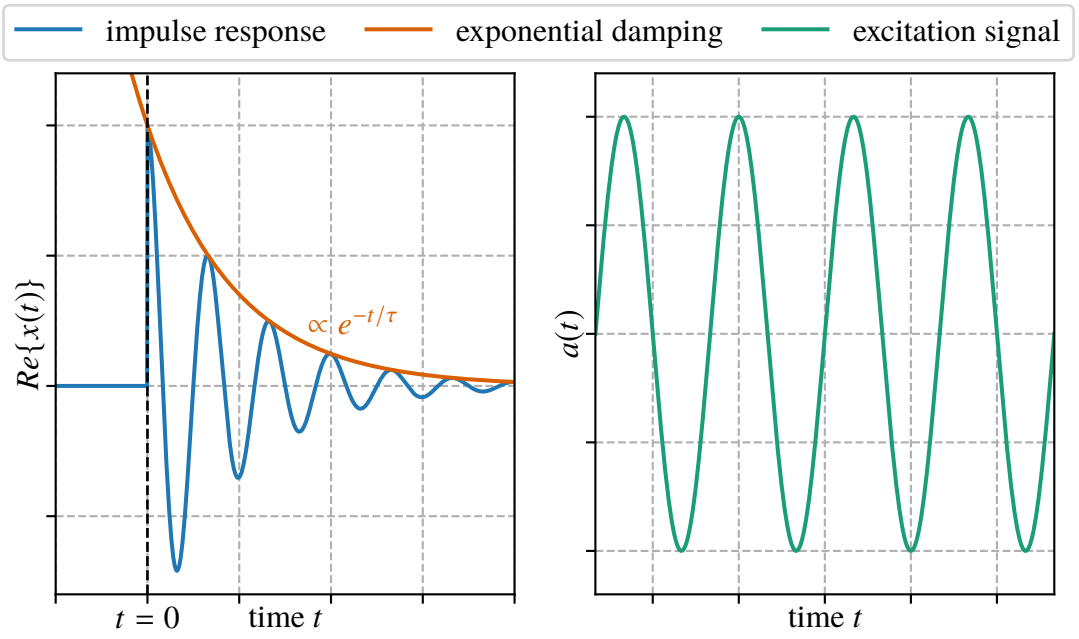

Figure 5.8.: Functions used to reconstruct the measured grow-damp mode signals. **Left:** Damped oscillation signal of a coupled-bunch mode with its amplitude decreasing exponentially. **Right:** Oscillating excitation signal.

transforms. For this purpose, $a(t)$ is Fourier transformed providing

$$A(\omega) = 2\pi A_{\mathrm{exc}}$$

for $\omega = \omega_{\mathrm{exc}}$. Additionally, the Fourier transform of $x(t)$ yields

$$X(\omega) = \frac{1}{\omega_1 - \omega + i\tau^{-1}}$$

and multiplying $A(\omega)$ and $X(\omega)$ results in the (measured) output signal

$$Y(\omega = \omega_{\mathrm{exc}}) = \frac{2\pi A_{\mathrm{exc}}}{\omega_1 - \omega_{\mathrm{exc}} + i\tau^{-1}}.$$

During all measurements, the excitation frequency ω_{exc} was set to the oscillation frequency of the observed coupled-bunch mode ω_1. The observed coupled-bunch mode with $\mu = 12$ has the oscillation frequency ω_{12}, which leads to

$$Y(\omega_{12}) = \frac{2\pi A_{\mathrm{exc}}}{i\tau^{-1}}$$

with the amplitude

$$|Y(\omega_{12})| = Y_{\mathrm{max}} = \frac{2\pi A_{\mathrm{exc}}}{\tau^{-1}}, \tag{5.3}$$

which equals the saturation value of the measurements and only depends on the excitation amplitude A_{exc} and the factor τ^{-1}. That means, if the excitation strength A_{exc} is known, the factor τ^{-1} can be determined by measuring the saturation value Y_{max} [88].

For experimentally investigating the interaction between RF phase modulation and coupled-bunch instabilities, the DELTA storage ring was filled with a bunch train of 144 bunches at a beam current of $I \approx 40\,\mathrm{mA}$. Although higher beam currents are generally more suitable for these studies, since the growth rates are higher, this value for the beam current was chosen nevertheless for two reasons. Firstly, the saturation method developed in the framework of this thesis (see Chapter 5.5) is only applicable below the instability threshold. With a threshold at DELTA of $I_{\mathrm{thr}} \approx 50\,\mathrm{mA}$ [46], this requirement is well satisfied. Secondly, while studying coupled-bunch growth rates as a function of the modulation amplitude, the change of beam current has to be taken into account, since the growth rate is proportional to I (see Eq. (2.30)). However, at such a low beam current, the beam lifetime was more than 20 h. The current was monitored during all measurement and even in the longest parameter sweep, its deviation was less than 1 %. Thus, the beam current is considered to be

constant in the following.

At first, a calibration measurement was performed to determine A_{exc}, which is necessary to use the saturation method. For this purpose, the saturation value Y_{max} as well as τ^{-1} were obtained for the same data set to be able to calculate A_{exc} based on Eq. (5.3). This was done by a grow-damp measurement without RF phase modulation, where τ^{-1} can be successfully evaluated by fitting an exponential curve to the damping signal. During this measurement, the beam was excited for several seconds by the drive generator of the longitudinal bunch-by-bunch feedback system. With a synchrotron frequency of $f_{\mathrm{s}} = 15.9\,\mathrm{kHz}$, the excitation frequency was set to $f_{\mathrm{exc}} = 31\,266\,\mathrm{kHz}$, so that the applied drive signal was at the frequency of mode $\mu = 12$ to make sure that only this mode was excited. The long excitation time was chosen to ensure that the beam was in an equilibrium state. Afterwards, two sets of data were taken. For the first data set, the beam was permanently excited by the

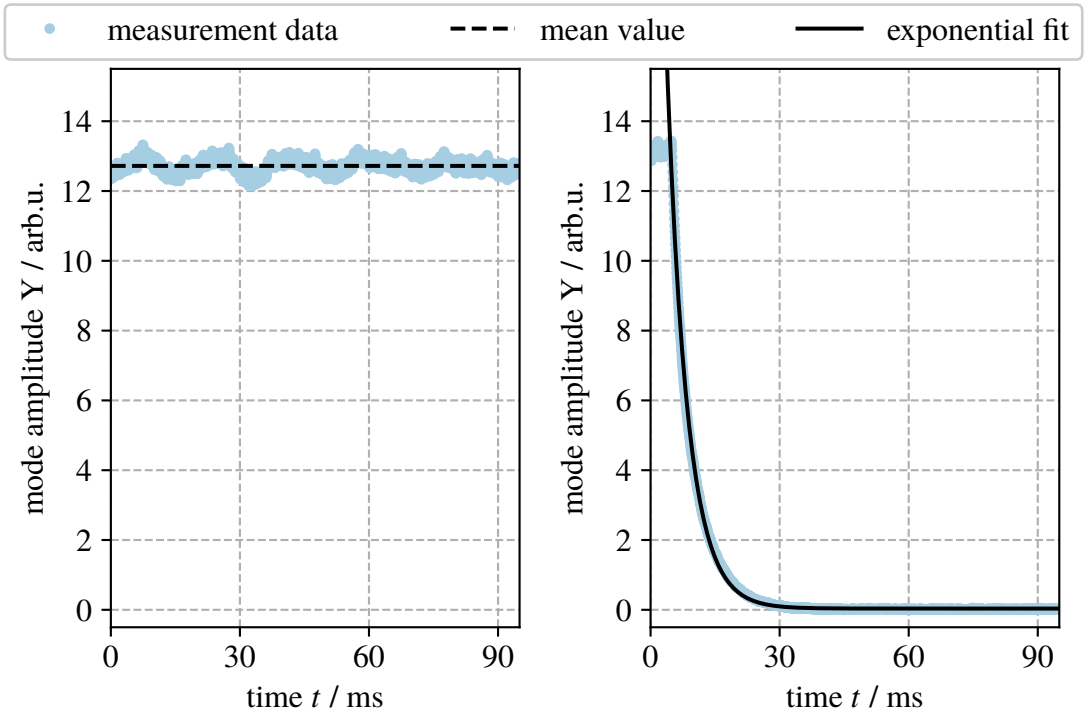

Figure 5.9.: Two datasets of the signal of mode $\mu = 12$ taken for the calibration measurement. **Left:** Permanent excitation to determine Y_{max} by taking the mean of the signal (dashed black line). The noise of the signal is mainly caused by electric hum (50 Hz noise). **Right:** Excitation turned off at $t = 5\,\mathrm{ms}$ to apply an exponential fit to the damping part of the signal (solid black line).

drive resulting in a saturated signal with its mean value being the saturation value

$$Y_{\max} = (12.72 \pm 0.21)\,\text{arb.units},$$

as shown in the left hand side of Fig. 5.9. For the second data set, the excitation was turned off after 5 ms. Subsequently, the beam damped down exponentially and τ^{-1} was determined by using an exponential fit of the form

$$f(t) = a \cdot e^{bt} + c$$

with the fit parameters

$$\begin{aligned} a &= (35.00 \pm 0.02)\,\text{arb.units} \\ b &= (211.96 \pm 0.08) \times 10^{-3}\,\text{ms}^{-1} \\ c &= (35.35 \pm 0.40) \times 10^{-3}\,\text{arb.units} \end{aligned}$$

as shown in the right hand side of Fig. 5.9, where $\tau^{-1} = b$ according to Eq. (2.28).

With the knowledge of $Y_{\max}$ and τ^{-1}, the excitation amplitude resulted in

$$A_{\text{exc}} = \frac{Y_{\max} \cdot \tau^{-1}}{2\pi} = (0.43 \pm 0.02)\,\text{arb.units}.$$

This excitation strength was used for further studies assuming that the excitation parameters of the drive generator remained untouched. This is especially true for RF phase modulation parameters but was also assumed for the beam current.

Next, the RF phase modulation amplitude sweep ws performed by varying the input voltage $\hat{U}_{\text{C}}$ from 0 V to 3 V leading to a phase shift ϕ_{cav} applied to the beam by the RF phase modulation from 0 deg to 4.91 deg. In every step, both types of datasets, as shown before, were recorded to determine $Y_{\max}$ as a function of ϕ_{cav}. With it, the damping rate gathered by the saturation method τ_{sat}^{-1} was calculated by using Eq. (5.3) with A_{exc} from the calibration measurement, to achieve τ_{sat}^{-1} as a function of ϕ_{cav}. In addition, the second type of dataset allows to determine the damping rate τ_{fit}^{-1} directly by exponential fitting to compare the results of both measurement methods. The results are shown in Fig. 5.10 [88].

Comparing the results of both methods leads to the following findings. The first data point of both methods is exactly the same by definition, since τ_{sat}^{-1} is calibrated to match τ_{fit}^{-1} at

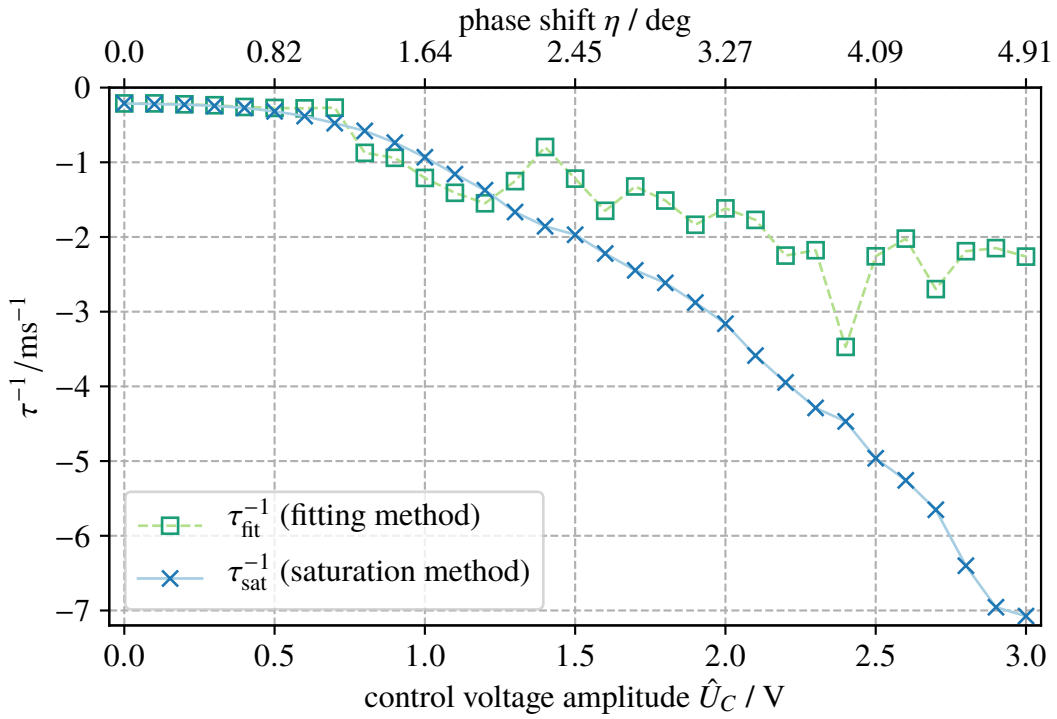

Figure 5.10.: The growth or damping rate τ^{-1} as a function of the phase shift applied to the beam by the RF phase modulation system, determined by exponential fitting (green) and by the saturation method (blue).

$\phi_{\mathrm{cav}} = 0\,\mathrm{deg}$. In the regime between $\phi_{\mathrm{cav}} = 0\,\mathrm{deg}$ and $\phi_{\mathrm{cav}} \approx 0.7\,\mathrm{deg}$, the obtained values of τ^{-1} of both methods are almost identical. For $\phi_{\mathrm{cav}} > 0.7\,\mathrm{deg}$, the data points of τ_{sat}^{-1} clearly follow a trend, while τ_{fit}^{-1} start acting erratically.

For $\phi_{\mathrm{cav}} > 0.7\,\mathrm{deg}$, only the results of the saturation method seem to be realistic and are further investigated in the following. For this purpose, the trend of $\tau_{\mathrm{sat}}^{-1}(\phi)$ was analyzed by fitting different polynomial functions as well as exponential functions to the data. The best match was achieved by a second-order polynomial function of the form

$$\tau^{-1}(\eta) = a \cdot \eta^2 + b$$

with the fit parameters

$$a = (-0.293 \pm 0.003)\,\mathrm{ms}^{-1}\,\mathrm{deg}^{-2}$$
$$b = (-0.254 \pm 0.031)\,\mathrm{ms}^{-1}$$

as shown in Fig. 5.11.

Comparing the results of the dependence of the growth or damping rate τ^{-1} on the RF phase modulation amplitude gathered experimentally at DELTA with the simulation results shown in Chapter 4.4, they shows a very similar behavior [75]. A comparison of both data sets is shown in Fig. 6.1 of the summary. It is important to note, that the rates of the simulation are positive values due to the absence of synchrotron radiation and the growth rate of the coupled-bunch mode τ_{G}^{-1} is evaluated directly. In the measurement, on the other hand, the growth or damping rate τ^{-1} is gathered, which has a constant negative offset τ_{D}^{-1} (see Chapter 2.4). Nonetheless, a quadratic dependence, demonstrated by second-order polynomial fits, exists in both cases. Hence, the assumption of a quadratic dependence of the growth rate on the RF phase modulation amplitude is very convincing, even with no analytical explanation available.

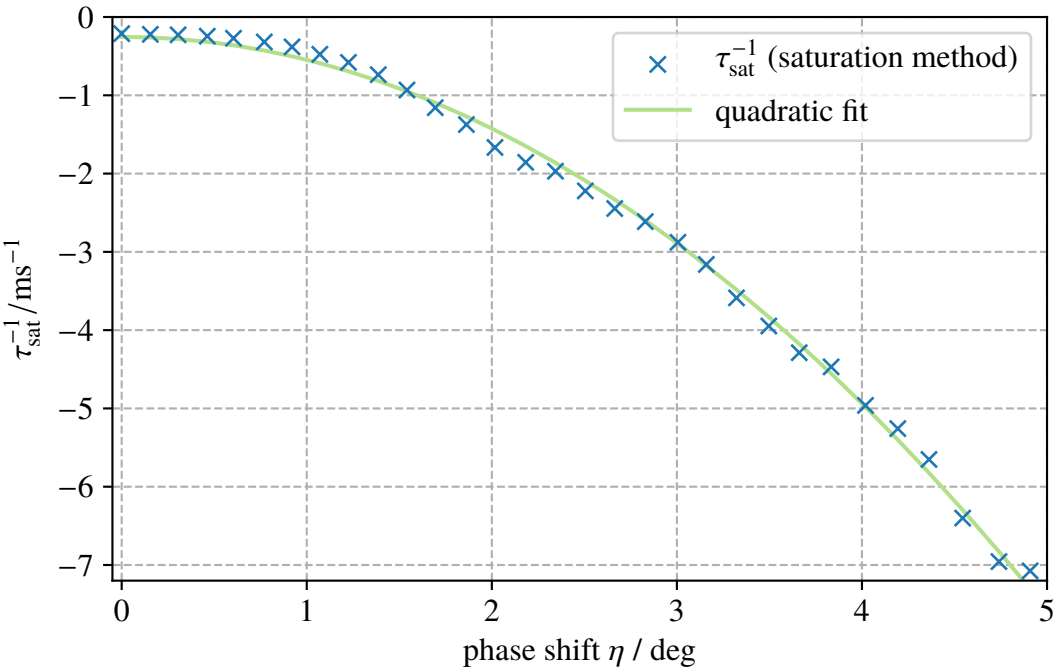

Figure 5.11.: The factor τ_{sat}^{-1} gathered by the saturation method as a function of the phase shift ϕ (blue) with a second-order polynomial fit (green) to investigate the trend.

5.6. Studies to Improve User Operation

During user operation at DELTA, the RF phase modulation system is permanently used to oppose coupled-bunch instabilities and to increase the beam lifetime at the cost of a lower beam quality. Due to higher oscillation amplitudes of the individual particles, the bunch length increases. In addition, mainly caused by the coupling of the longitudinal and the horizontal plane due to dispersion, also the transverse beam size increases. Although the bunch-by-bunch feedback system is capable of eliminating coupled-bunch effects without reducing the beam quality, the increased beam lifetime caused by the RF phase modulation is more important for the users, leaving it as the system of choice at DELTA.

The investigations done in the framework of this thesis regarding RF phase modulation, coupled-bunch instabilities and the bunch-by-bunch feedback system, lead to two ideas how to improve the user operation of DELTA.

Firstly, the injection efficiency can be improved by stabilizing the beam with the bunch-by-bunch feedback system during injection. A measurement showing that effect is presented in Section 5.6.1.

Secondly, a deeper understanding of the effects of RF phase modulation on the beam lead to the possibility to automatize the process of finding optimal values for the RF phase modulation parameters after each injection. For this purpose, a map of stability as a function of the modulation amplitude and frequency was created as shown in Section 5.6.2.

5.6.1. Improving the Injection Efficiency

Although the RF phase modulation is used during user operation when the beam is stored for several hours, it is turned off during injection. The additional longitudinal oscillations induced by phase modulation would lead to transverse oscillations, mainly in the horizontal plane, caused by dispersion leading to particle loss and reducing the injection efficiency. The same is true for coupled-bunch instabilities, which usually occur in the longitudinal plane at DELTA. The impact of both effects on the injection efficiency depends on several machine parameters, e.g., the orbit, the strength of the injection kickers, etc. Basically, a more stable beam is advantageous for the injection efficiency, but RF phase modulation is no option in this case. This leads to the approach of using the bunch-by-bunch feedback system during injection to stabilize the beam with negative feedback. To test this idea, injection was performed increasing the beam current from 100 mA to 120 mA, a regime

in which coupled-bunch instabilities are always present at DELTA. The phase modulation system was turned off and the bunch-by-bunch feedback system was turned on and off periodically. The injection efficiency, the status of the feedback and the beam current were tracked during this test and the results are shown in Fig. 5.12.

Without changing any parameters at high beam currents, the injection efficiency decreases, most likely due to coupled-bunch instabilities, as seen up to 105 mA. Whenever the feedback is turned on, the beam is stabilized resulting in an efficiency increase up to 15 percentage points. A correlation of injection efficiency and bunch-by-bunch feedback is clearly visible.

Consequently, a feature was added to the main control panel of the DELTA control system making easy usage of the bunch-by-bunch feedback system during injection possible for every operator. A status button was also added to the DELTA system overview, which monitors all diagnostic systems.

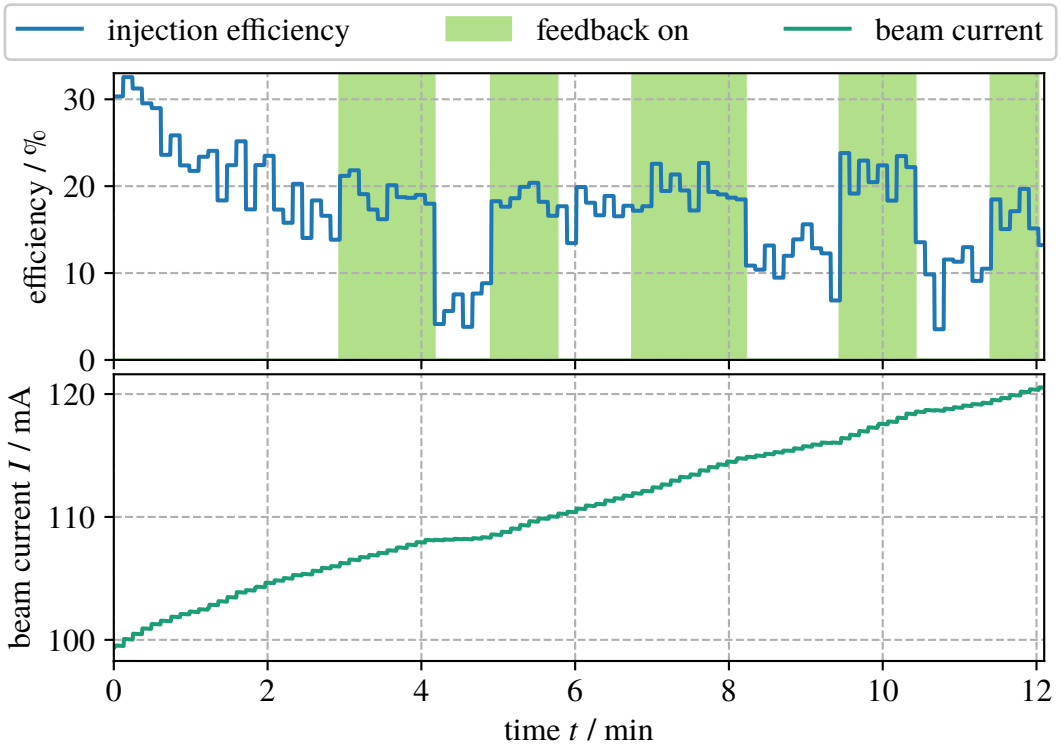

Figure 5.12.: Injection process from approx. 100 mA to 120 mA. **Top:** Injection efficiency as a function of time. The times when the bunch-by-bunch feedback was turned on to stabilize the beam are marked in green. **Bottom:** Corresponding beam current as a function of time.

Over several month, it was observed, that the described impact on the injection efficiency was reproduced multiple times, but is not always present. This is most likely based on the fact that many machine parameters change from week to week. As mentioned before, the particle loss due to coupled-bunch instabilities during injection is strongly dependent on various parameters and is therefore different from week to week. However, stabilizing the beam never resulted in decreased injection efficiency as long as the feedback was well-calibrated. Therefore, the bunch-by-bunch feedback is used during injection on a regular basis now.

5.6.2. Mapping the Stability of the Beam as a Function of Phase Modulation Amplitude and Frequency

After every injection, the RF phase modulation system has to be turned on again by the operator in charge. The general procedure is, that the operator manually changes the control voltage amplitude U_C and frequency f_{mod} to find a regime where the sidebands at the synchrotron frequency f_s in the beam spectrum vanish, which indicates that the most unstable coupled-bunch instability is eliminated. To keep the beam quality reduction at a minimum, $\hat{U}_C$ is set as small as possible.

To optimize this process, a combined parameter sweep was performed altering $\hat{U}_C$ and f_{mod} in steps of 25 Hz resp. 50 mV to create a map of stability. In each iteration, the mean spectral power at the synchrotron frequency $P_\Sigma(f_s)$ was evaluated. The results for f_s = 15.8 kHz are shown in Fig. 5.13 and exhibit a triangular region in which the beam is stable. The beam can already be stabilized at $\hat{U}_C$ = 400 mV with f_{mod} = 31.5 kHz, which is slightly below twice the synchrotron frequency. However, the frequency bandwidth of the stable region at this point is very small. Increasing the amplitude shifts the operation point, reducing the necessary precision of the modulation frequency, giving more space for fluctuations. To ensure an acceptable bandwidth, the value $\hat{U}_C$ = 700 mV is chosen, which already provided good experiences in the past. This leaves f_{mod} as the only parameter that has to be tuned after every injection and should be set slightly below twice the synchrotron frequency. The longitudinal bunch-by-bunch feedback system measures the synchrotron frequency whenever the center-of-mass of the electron bunches oscillate.

To automatize the procedure described above, a Python application was developed and added to the control system of DELTA, working as follows. First, the phase modulation is turned off for 5 seconds to ensure, that the feedback system measures the synchrotron

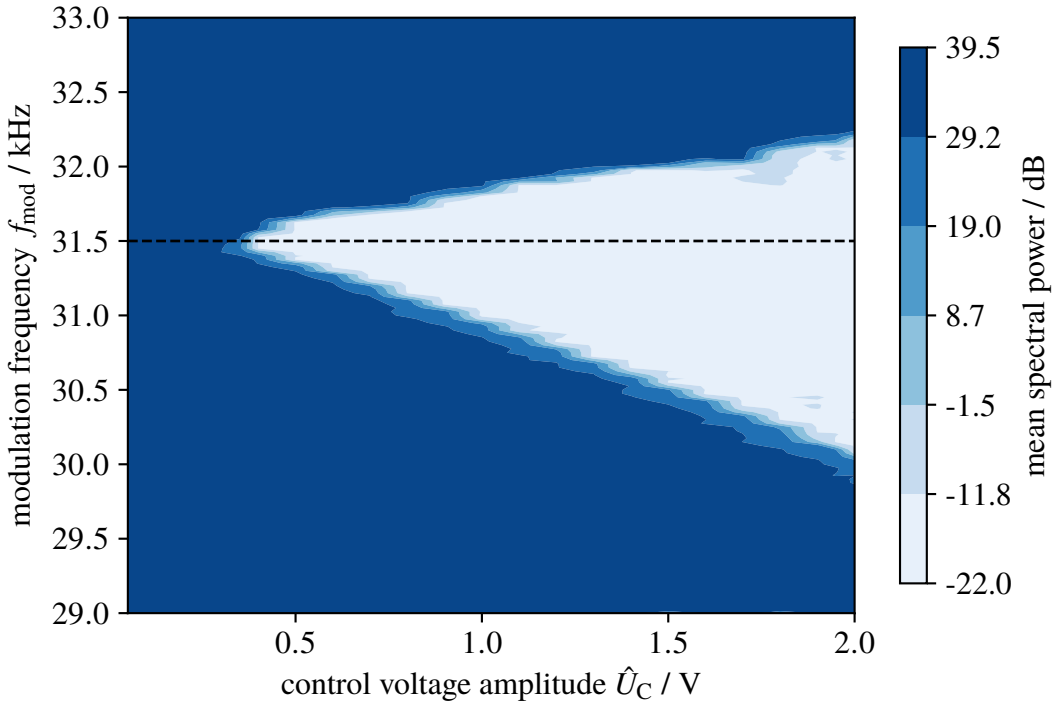

Figure 5.13.: Mean spectral power at the synchrotron frequency for a combined parameter sweep of the RF phase modulation amplitude $\hat{U}_C$ and frequency f_{mod}. Around the optimal modulation frequency (highlighted with a dashed black line) is a triangular region where the beam is stable. Negative values (shown in light blue) indicate that the beam is stable, while high values (dark blue) show that the RF phase modulation has no effect on the beam.

frequency correctly. Then the modulation frequency

$$f_{mod} = 2 \cdot f_s - 300\,\text{Hz}$$

is returned and can be applied to the RF phase modulation system by one click. This additional request is implemented to give the operator the chance to check the modulation frequency, making sure that a meaningful value was set by the script.

The triangular stable region in Fig. 5.13 is not symmetric since the area below 31.5 kHz is larger, than the area above that value. There are two ideas to explain this asymmetry, but also a combination of both is conceivable.
Firstly, the operation range of the RF phase modulation system at DELTA is not linear, as shown in Chapter 3.2. The higher $\hat{U}_C$ is, the stronger these nonlinearities get, which could lead to an asymmetric stable region.

Secondly, it is conspicuous that the map of stability in Fig. 5.13 looks very similar to Fig. 2.8 showing the regimes which determine how many fix points exist in the longitudinal phase space. There is a threshold below which no effect of the RF phase modulation on the beam can be detected, which is therefore most likely a synchrotron radiation threshold. The regime in which the beam is stable corresponds to the regime in which two fix points exist. While the upper bifurcation edge at $f_{\mathrm{mod}} = 2 \cdot f_{\mathrm{s}} + \epsilon$ separates the area of two stable fix points from the area of one stable fix point, the lower bifurcation edge at $f_{\mathrm{mod}} = 2 \cdot f_{\mathrm{s}} - \epsilon$ separates it from the regime of three stable fix points. That would explain why the regime of stability has a different shape at high frequencies than at low frequencies. This was also observed in Chapter 5.1. This means, that RF phase modulation can suppress the excitation of coupled-bunch instabilities as long as more than one stable fix point exist in the longitudinal phase space and as long as the modulation frequency is close to twice the synchrotron frequency.

6. Summary and Outlook

In order to gain a deeper understanding of the particle dynamics regarding the suppression of the excitation of coupled-bunch instabilities by RF phase modulation, different approaches were used. Firstly, numerical tracking codes were utilized to determine the coupled-bunch growth rates under the influence of RF phase modulation. Although a variety of particle tracking codes are available, they cannot be used to solve the problem. These codes either use rigid macro-particles representing the bunches to investigate coupled-bunch effects, which rules out the possibility to take phase modulation effects into account, or use thousands of particles per bunch in all calculations to analyze the effects of RF phase modulation on the longitudinal phase space by using parallelization techniques to improve the performance. Unfortunately, parallelization cannot be utilized in the presence of wake fields, since these effects depend on the preceding particles, making it necessary to calculate each particle one after the other. With coupled-bunch growth rates being in the millisecond range, ten thousands of turns have to be calculated making this approach impractical.

For the aforementioned reasons, a new tracking code was developed, combining the two common approaches of using macro particles for coupled-bunch effects and multi-particle bunches for phase-modulation effects. This is done by using matrix operations for all particles at once to calculate phase focusing in the accelerating cavity in the presence of RF phase modulation and only the center of mass of the bunch for wake field effects. The code was validated by observing the coupled-bunch growth rate as a function of the beam current, resulting in a linear trend, as expected from the theory. Afterwards, the code was used to analyze the effect of RF phase modulation on coupled-bunch instabilities by sweeping the modulation amplitude η and obtaining the coupled-bunch growth rate τ_{G}^{-1} in every iteration. On the left-hand side of Fig. 6.1, the results show a quadratic dependence of τ_{G}^{-1} on η.

In a second approach, the findings stated above were further investigated by experimental studies at the DELTA storage ring. DELTA utilizes an RF phase modulation system as well as

a bunch-by-bunch feedback system as a diagnostic tool to analyze coupled-bunch effects. Both systems were investigated separately to obtain a better understanding of their impact on the electron beam, before they were used in combination.

In the first experimental study, the modulation frequency f_{mod} was swept and the sum of the single-bunch spectra was analyzed to find the optimum value for f_{mod} at which the suppression of coupled-bunch instabilities is maximized. While the effect was observed slightly below the second and third integer harmonic of the synchrotron frequency f_{s}, as already seen at many other facilities, the suppression is significantly stronger at a frequency slightly below twice the synchrotron frequency at DELTA, a value which was used for all further studies.

Afterwards, the RF phase modulation system was in focus. Since the phase shift applied to the beam by the RF phase modulation system is not available at DELTA, a study was performed to determine the phase shift of the RF phase modulation system at its output ϕ_{PS} and inside the accelerating cavity ϕ_{cav} as a function of the amplitude of the control voltage $\hat{U}_{\mathrm{C}}$. The phase shift was observed and showed a linear dependence on $\hat{U}_{\mathrm{C}}$ with a maximum value of $\phi_{\mathrm{cav}} \approx 4.91\,\mathrm{deg}$ at $\hat{U}_{\mathrm{C}} = 3\,\mathrm{V}$. During user operation, the control voltage is usually set to $\hat{U}_{\mathrm{C}} = 0.7\,\mathrm{V}$ which equals a phase shift of 1.08 deg.

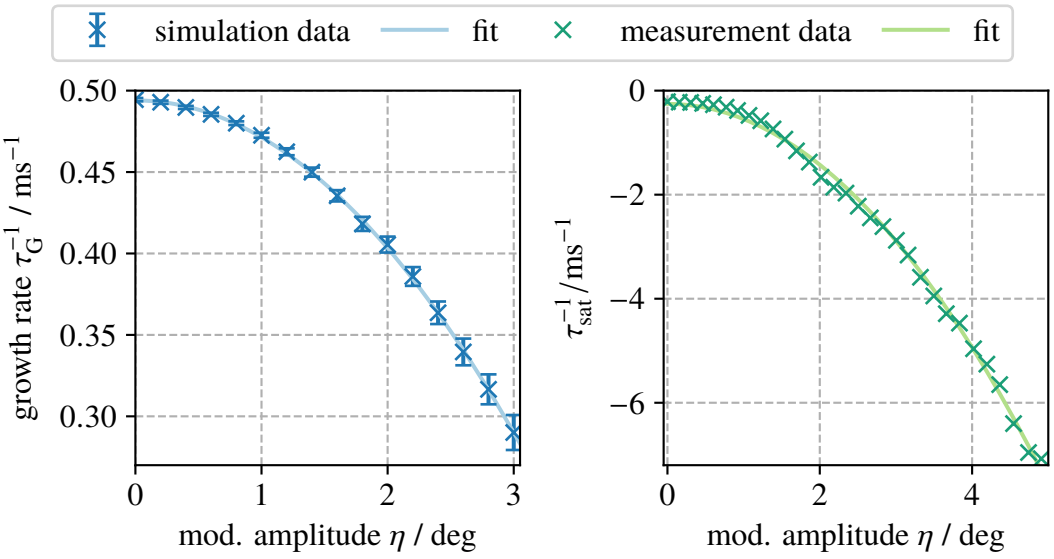

Figure 6.1.: Coupled-bunch growth rate as a function of the modulation amplitude η obtained by numerical simulations (in blue on the left-hand side) and by using the saturation method for measurements at DELTA (in green on the right-hand side). Both show a quadratic dependence on η, highlighted by quadratic fits.

While investigating coupled-bunch instabilities in the presence of RF phase modulation, it was observed that the common method to determine coupled-bunch growth rates by fitting an exponential function to the mode signal is not applicable for high modulation amplitudes. The fact that RF phase modulation causes additional center-of-mass motion and that the bunch-by-bunch feedback system can only measure the center-of-mass of the bunches results in a convolution of both effects in the measured data, which is not accurately described by exponential functions.

To solve this issue, a new measurement technique was developed using the saturation value of the mode signal when the beam is excited at a specific mode by the bunch-by-bunch feedback system while the beam current is well below the instability threshold. With it, the growth or damping rate τ^{-1} was successfully obtained for modulation amplitudes up to $\eta \approx 4.9\,\mathrm{deg}$. The results also show a quadratic dependence of τ^{-1} on the modulation amplitude η and are compared with the simulation data in Fig. 6.1.

Although no analytical description for the quadratic dependence was found, a comparison of the results of simulation and measurement reveals that the dependence of the growth rate on the modulation amplitude was successfully determined to be quadratic in the investigated area. The absolute values do not match due to the fact, that the simulation is able to determine the growth rate τ_{G}^{-1} directly, while in the measurement, only the combination of damping and growth rate $\tau^{-1} = \tau_{\mathrm{D}}^{-1} + \tau_{\mathrm{G}}^{-1}$ can be obtained. In addition, some of the parameters used in the simulation differ from parameters of the DELTA storage ring for performance reasons. This adds small deviations to the absolute values.

Based on the knowledge and experience gained through the aforementioned studies, two additional tools were developed to improve the user operation of the DELTA storage ring. Firstly, it was shown, that the injection efficiency can be improved by using the bunch-by-bunch feedback system to stabilize the beam during the injection process. For this purpose, an easy-to-use application was added to the control system. Secondly, the RF phase modulation parameters were swept in a combined parameter sweep to create a map of stability, which directly shows which parameter sets can be used to stabilize the beam. With these parameters, another application was developed and added to the control system to set the optimum modulation parameters automatically.

A. Appendix

A.1. DELTA Cavity Voltage and Phase

From the main parameters of the DELTA storage ring, shown in Table 3.1, the amplitude of the cavity voltage can be calculated as well as the synchronous phase. For this purpose, Eq. (2.8) is rearranged to calculate the amplitude of the cavity voltage to

$$\hat{U} = \sqrt{2PR_\mathrm{s}} = 387.30\,\mathrm{kV}$$

with the cavity power $P = 25\,\mathrm{kW}$ and the shunt impedance $R_\mathrm{s} = 3\,\mathrm{M\Omega}$.

In order to determine the synchronous phase, the energy loss of the stored electron particles per revolution is calculated using [89]

$$\Delta E = \frac{e^2}{3\epsilon_0 R_\mathrm{b}} \frac{E_0^4}{\left(m_\mathrm{e} c^2\right)^4},$$

with the electron charge e, the electron mass m_e, the speed of light c, the vacuum permittivity ϵ_0, the bending radius $R_\mathrm{b} = 3.33\,\mathrm{m}$ and the nominal energy $E_0 = 1.5\,\mathrm{GeV}$. The resulting voltage necessary to compensate the energy loss per revolution is

$$U_\mathrm{acc} = \frac{\Delta E}{e} = 134.49\,\mathrm{kV}.$$

The synchronous phase results from the ratio of the amplitude of the cavity voltage $\hat{U}$ and the accelerating voltage U_acc, giving [6]

$$\phi_\mathrm{s} = \arcsin\left(\frac{U_\mathrm{acc}}{\hat{U}}\right) = 20.32\,\mathrm{deg}$$

and

$$\overline{\phi}_\mathrm{s} = \pi - \phi_\mathrm{s} = 159.68\,\mathrm{deg}.$$

To test whether these values are reasonable, the synchrotron frequency [89]

$$\omega_\mathrm{s} = \omega_\mathrm{rev}\sqrt{-\frac{e\hat{U}\cos\left(\overline{\phi}_\mathrm{s}\right)}{2\pi\beta^2 E_0}\left(\alpha - \frac{1}{\gamma^2}\right)}$$

is calculated with the revolution frequency $f_\mathrm{rev} = \omega_\mathrm{rev}/2\pi = 2.6\,\mathrm{MHz}$, the Lorentz factor $\gamma = 2935$, the ratio $\beta = v/c \approx 1$ and the momentum compaction factor $\alpha = 4.9 \times 10^{-3}$ and yields

$$f_\mathrm{s} = \frac{\omega_\mathrm{s}}{2\pi} = 15.67\,\mathrm{kHz},$$

which is in good agreement with typical synchrotron frequencies at DELTA of 15.5 kHz to 16.5 kHz.

A.2. Figures of Merit of the DORIS Cavity at DELTA

To verify the design parameters of the DORIS cavity installed at DELTA, a vector network analyzer (VNA) [90] was used. The connection between the klystron and the cavity was cut and the VNA is connected to the coupling loop and the measurement loop of the cavity. With this setup, so-called S-parameter-measurements were performed [91]. The goal was to determine the quality factor Q_0, the loaded quality factor Q_L and the coupling factor κ. The measurements follow the procedures described in [82].

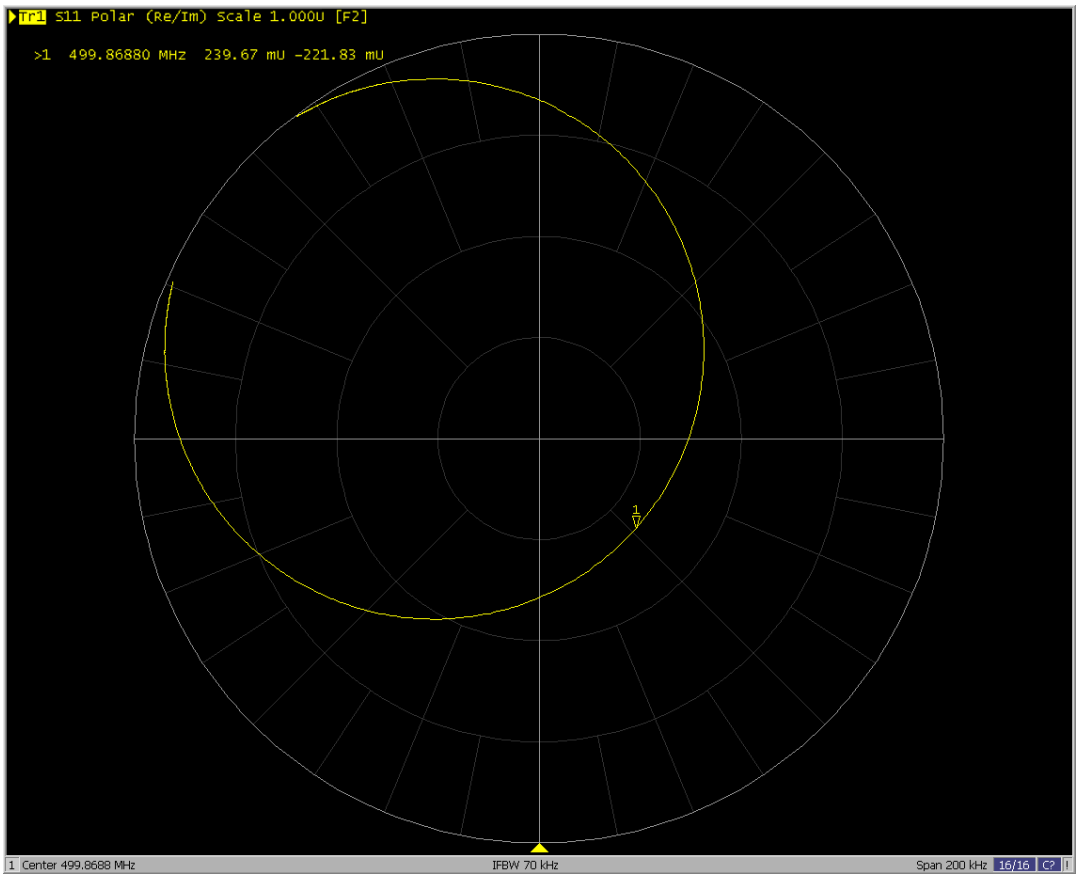

Figure A.1.: Complex plane of the reflected S_{11}-signal of the coupling loop. The circle includes the zero value meaning, that the system is overcritical with $\kappa > 1$.

First, the coupling into the cavity has to be tested. Due to beam loading effects, the cavity has to be detuned to minimize the reflected power at high beam currents. This is done by rotating the coupling loop. Depending on its orientation, the coupling into the cavity can be overcritical ($\kappa > 1$), critical ($\kappa = 1$) or undercritical ($\kappa < 1$). This can be checked by measuring the reflected signal (S_{11}) at the coupling loop and plotting it in the complex plane. The measured complex plane is depicted in Fig. A.1 and shows, that the obtained circle in-

cludes the zero value, which proves that the coupling factor is $\kappa > 1$, which corresponds to an overcritical system.

In this case, the coupling factor equals the standing wave ratio (SWR) of the reflected signal (S_{11}), which was measured with the VNA. The measurement data is shown in Fig. A.2. The SWR-value corresponds to the loss-value in the plot of $\kappa = 1.97$.

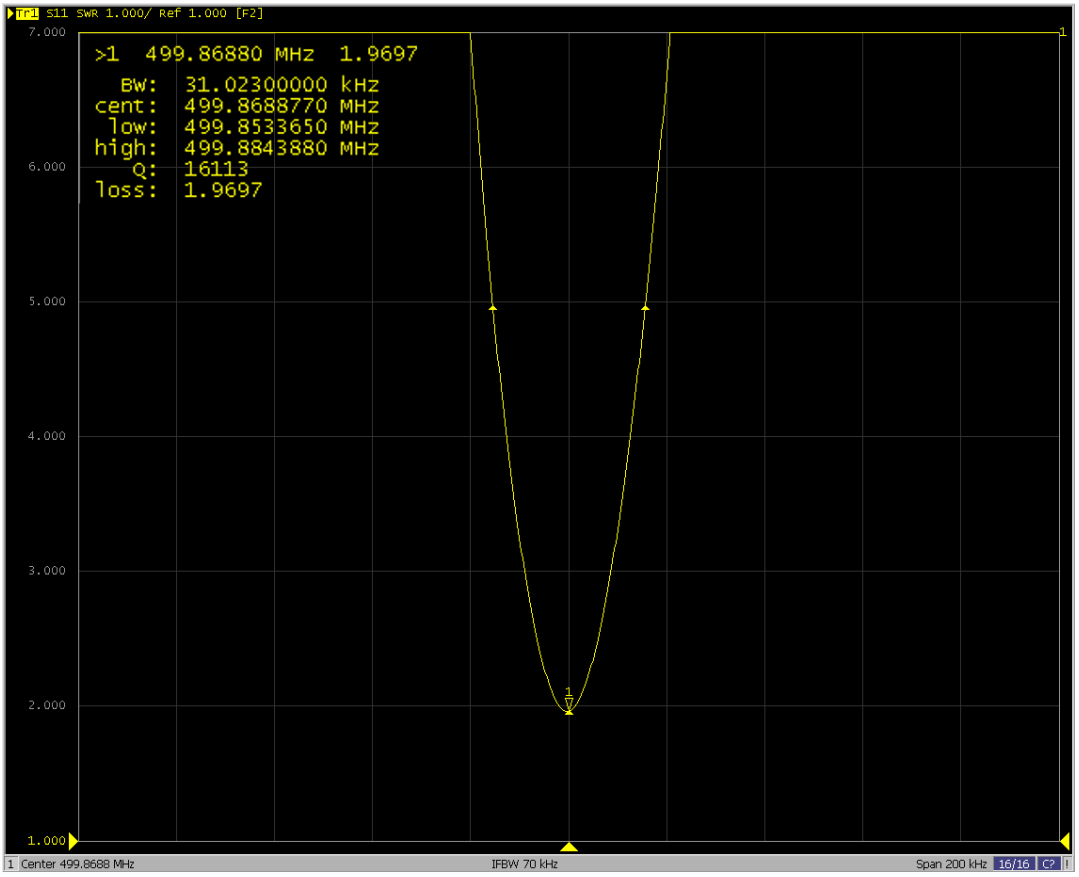

Figure A.2.: Standing wave ratio (SWR) measurement of the S_{11} signal to determine the coupling factor.

Next, the loaded quality factor Q_L was measured by a transmission measurement (S_{21}) from the coupling loop to the measurement loop. With this method, Q_L was determined by the bandwidth $\Delta\omega$ between the -3 dB-points around the resonance frequency ω_{res} with

$$Q_L = \frac{\omega_{res}}{\Delta\omega}.$$

The measured data in Fig. A.3 show a bandwidth of $\Delta\omega = 40.5\,\text{kHz}$ with a resonance frequency of $\omega_{res} = 499.868\,\text{MHz}$, which results in a loaded quality factor of $Q_L = 12\,342$.

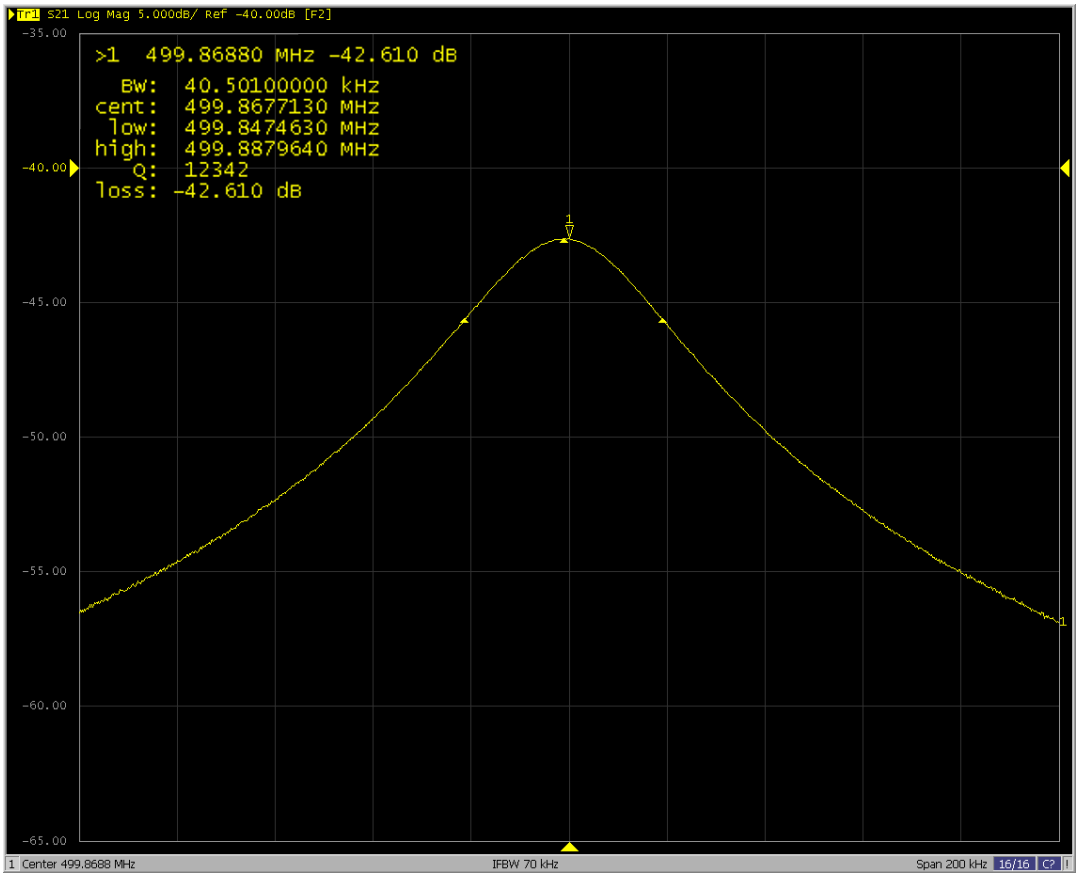

Figure A.3.: Transmission signal (S_{21}) from the coupling loop to the measurement loop. The loaded quality factor of the cavity Q_L was determined by the resonance frequency and the bandwidth between the -3 dB-points.

Eventually, the unloaded quality factor Q_0 of the DORIS cavity installed at DELTA is calculated by

$$Q_0 = Q_L\,(1+\kappa) = 36\,656,$$

according to Eq. (2.7), which is in good agreement with the expected value of 36 000.

A.3. The Saturation Method to determine Coupled-Bunch Damping Rates in the Presence of RF Phase Modulation

For the saturation method introduced in Chapter 5.5, the beam is excited by the bunch-by-bunch feedback system and damped by synchrotron radiation effects resulting in an equilibrium state as shown in the left-hand side of Fig. 5.9. To understand this regime, a mathematical model to reconstruct the measured signal $y(t)$ is developed in the following. In signal processing, the output signal is the result of the convolution of the input signal with the impulse response of the system [68]. In the equilibrium state, the input signal

$$a(t) = A_{\mathrm{exc}} \cdot e^{i\omega_{\mathrm{exc}} t}$$

is the excitation signal of the drive generator of the longitudinal bunch-by-bunch feedback system. The impulse response of the beam is a damped oscillation

$$x(t) = \begin{cases} 0 & \text{for} \quad t < 0 \\ -ie^{\psi t} & \text{for} \quad t \geq 0 \end{cases}$$

with $\psi = i\omega_1 - \tau^{-1}$, the oscillation frequency ω_1 and the factor $\tau^{-1} \geq 0$. This signal is the general form of Eq. (2.28) as shown by

$$\begin{aligned} \mathrm{Re}\{x(t \geq 0)\} &= \mathrm{Re}\left\{-ie^{i\omega_1 t} e^{-t/\tau}\right\} \\ &= \mathrm{Re}\left\{-i\left[\cos(\omega_1 t) + i \sin(\omega_1 t)\right] e^{-t/\tau}\right\} \\ &= \mathrm{Re}\left\{\left[\sin(\omega_1 t) - i \cos(\omega_1 t)\right] e^{-t/\tau}\right\} \\ &= \sin(\omega_1 t)\, e^{-t/\tau}, \end{aligned}$$

which equals Eq. (2.28) with $k = \phi = 0$. Fourier transformation of $a(t)$ provides

$$\begin{aligned} A(\omega) &= \int_{-\infty}^{\infty} A_{\mathrm{exc}} e^{i\omega_{\mathrm{exc}} t} e^{-i\omega t} dt \\ &= A_{\mathrm{exc}} \int_{-\infty}^{\infty} \exp\{-i(\omega - \omega_{\mathrm{exc}})\, t\}\, dt \\ &= 2\pi A_{\mathrm{exc}} \delta(\omega - \omega_{\mathrm{exc}}), \end{aligned}$$

with the delta function

$$\delta(\omega) = \begin{cases} 1 & \text{for} \quad \omega = 0 \\ 0 & \text{otherwise} \end{cases}$$

which represents a normalized pulse [68].

Additionally, the Fourier transform of $x(t)$ yields

$$\begin{aligned} X(\omega) &= \int_{-\infty}^{\infty} x(t \geq 0)\, e^{-i\omega t}\, dt \\ &= \int_{0}^{\infty} -i e^{i\omega_1 t} e^{-\tau^{-1} t} e^{-i\omega t}\, dt \\ &= -i \int_{0}^{\infty} \exp\left\{\left[i(\omega_1 - \omega) - \tau^{-1}\right] t\right\} dt \\ &= -i \left[\frac{1}{i(\omega_1 - \omega) - \tau^{-1}} \exp\left\{i(\omega_1 - \omega)\, t - \tau^{-1} t\right\} \right]_0^{\infty} \\ &= \lim_{t \to 0} \frac{-1}{\omega_1 - \omega + i\tau^{-1}} \left(\underbrace{\exp\left\{i(\omega_1 - \omega)\, t - \tau^{-1} t\right\}}_{\to 0} - 1 \right) \\ &= \frac{1}{\omega_1 - \omega + i\tau^{-1}}. \end{aligned}$$

Multiplying $A(\omega)$ and $X(\omega)$ results in the (measured) output signal

$$\begin{aligned} Y(\omega) &= A(\omega) \cdot X(\omega) \\ &= \frac{2\pi A_{\text{exc}} \delta(\omega - \omega_{\text{exc}})}{\omega_1 - \omega_{\text{exc}} + i\tau^{-1}}, \end{aligned}$$

which simplifies for $\omega = \omega_{\text{exc}}$ to

$$Y(\omega = \omega_{\text{exc}}) = \frac{2\pi A_{\text{exc}}}{\omega_1 - \omega_{\text{exc}} + i\tau^{-1}}.$$

During all measurements, the excitation frequency ω_{exc} was set to the oscillation frequency of the observed coupled-bunch mode ω_1, which leads to

$$Y(\omega = \omega_1 = \omega_{\text{exc}}) = \frac{2\pi A_{\text{exc}}}{i\tau^{-1}}$$

with the amplitude

$$|Y(\omega = \omega_1 = \omega_{\text{exc}})| = Y_{\text{max}} = \frac{2\pi A_{\text{exc}}}{\tau^{-1}},$$

which equals the saturation value of the measurements.

B. Acknowledgements

I want to express my sincerest thanks to Prof. Dr. Thomas Weis, who was a fantastic supervisor. I am really grateful for the opportunity to work on this interesting topic, the chance to participate in several international conferences and for all the support during these past few years. I also want to thank Prof. Dr. Shaukat Khan and Prof. Dr. Andreas Jankowiak, who offered to be the first and second reviewer of my thesis, respectively.

My research and I greatly benefited from the various fruitful and sometimes heated discussions, despite not always being related to my work, and the great atmosphere my colleagues at DELTA created, especially Benjamin Isbarn, Bernard Riemann, Stefan Kötter, Arne Meyer auf der Heide, Carsten Mai, Jochem Friedl, Peter Hartmann, Gerald Schmidt and Detlev Schirmer. I also want to thank my colleagues from the Helmholtz-Zentrum Berlin Dr. Martin Ruprecht, Dr. Paul Goslawski and Prof. Dr. Adolfo Velez as well as Dr. Tobias Tydecks from CERN, with whom I have collaborated on two joint research projects.

I would like to thank the technicians and engineers at DELTA, who keep DELTA running week by week. Special thanks go to Wolfgang Brembt and Vadim Kniss, who helped me several times with their expertise in the electronical departement and with my measurements at the RF phase modulation system as well as the DELTA cavity.

I acknowledge the financial support of the TU Dortmund University and the Bundesministerium für Bildung und Forschung.

I'd like to express my gratitude to Arne Meyer auf der Heide, Benjamin Isbarn, Isabel Großkreuz and Prof. Dr. Shaukat Khan for critically reviewing and, in doing so, helping me finalise my thesis.

Special thanks go to Benjamin Isbarn, who has been the most important colleague and friend during my whole studies. I will always remember all the time we spent together in our office, all the (mostly too loud) discussions, the moments we helped or distracted each other and everything we did outside of work.

I am deeply grateful to my whole family and to Isabel Großkreuz for the continuous support, for being interested in my work, for asking critical questions and for always encouraging me.

The most special acknowledgement goes to my beloved Lisa for always being there for me, for the incredible patience during the writing process of this thesis, for all the supprt, for always being understanding, for making me happy everyday and, most of all, for being mine.

References

[1] Basic Energy Sciences Advisory Committee. "Next-Generation Photon Sources for Grand Challenges in Science and Energy". Tech. rep. U.S: Department of Energy, 2009.

[2] F. R. Elder, A. M. Gurewitsch, R. V. Langmuir, and H. C. Pollock. "Radiation from Electrons in a Synchrotron". In: *Phys. Rev.* 71.11 (1947), pp. 829–830.

[3] "Light Sources of the World". https://lightsources.org/lightsources-of-the-world/. Accessed: 26. August 2018.

[4] S. Khan. "Collective Phenomena in Synchrotron Radiation Sources". Springer Verlag Berlin Heidelberg, 2006. ISBN: 13 978-3-540-34312-7.

[5] R. Nagaoka and K. L. F. Bane. "Collective Effects in a Diffraction Limited Storage Ring". In: *Journal of synchrotron radiation* 21 Pt 5 (2015), pp. 937–60.

[6] H. Wiedemann. "Particle Accelerator Physics". 3rd ed. Springer Verlag London, Limited, 2007. ISBN: 978-3-54-04904-56.

[7] "Photon Source BESSY-II". https://www.helmholtz-berlin.de/quellen/bessy/index_en.html. Accessed: 28. September 2018.

[8] A. Jankowiak, J. Knobloch, P. Goslawski, and N. Neumann. "Technical Design Study BESSY VSR". Tech. rep. Helmholtz-Zentrum Berlin für Materialien und Energie GmbH, 2015.

[9] M. Ruprecht. "Calculation of Coupled Bunch Effects in the Synchrotron Light Source BESSY VSR". Dissertation. Humboldt-Universität zu Berlin, 2016.

[10] MAX IV Facility. "The MAX IV Detailed Design Report". Tech. rep. available online at https://www.maxiv.lu.se/accelerators-beamlines/accelerators/accelerator-documentation/max-iv-ddr/. Lund, Sweden, 2010.

[11] A. R. D. Rodrigues, F. Arroyo, O. R. Bagnato, J. F. Citadini, R. H. A. Farias, J. G. R. S. Franco, R. J. Leão, L. Liu, S. R. Marques, R. T. Neuenschwander, C. Rodrigues, F. Rodrigues, and R. M. S. O. H. V. Silva. "Sirius Light Source Status Report". In: *9th International Particle Accelerator Conference*. Vancouver, BC, Canada, 2018, pp. 2886–2889.

[12] S. C. Leemann, Å. Andersson, M. Eriksson, L.-J. Lindgren, E. Wallén, J. Bengtsson, and A. Streun. "Beam dynamics and expected performance of Sweden's new storage-ring light source: MAX IV". In: *Phys. Rev. ST Accel. Beams* 12.12 (2009), p. 120701.

[13] "SuperKEKB". `http://www-superkekb.kek.jp/`. Accessed: August 2019.

[14] K. Akai, K. Furukawa, and H. Koiso. "SuperKEKB collider". In: *Nuclear Instruments and Methods in Physics Research Section A: Accelerators, Spectrometers, Detectors and Associated Equipment* 907 (2018), pp. 188–199.

[15] N. Lehnart and H. Peterson. "Ferrit-Dämpfungsantennen gegen parasitäre Cavity-Modes in den DORIS-Hohlraum-Resonatoren". Technische Notiz H2-77/12. DESY, Hamburg, Germany, 1977.

[16] B. Dwersteg, E. Seesselberg, and A. Zolfaghari. "Higher Order Mode Couplers for Normal Conducting Doris 5-Cell Cavities". In: *IEEE Transactions on Nuclear Science* 32.5 (1985), pp. 2797–2799.

[17] R. Eichhorn, J. Conway, Y. He, Y. Li, T. O'Connel, P. Quigley, J. Sears, and V. Shemelin. "Higher Order Mode Absorbers for High Current ERL Applications". In: *5th International Particle Accelerator Conference*. Dresden, Germany, 2014, pp. 4037–4039.

[18] Y. V. Shashkov, N. P. Sobenin, and M. M. Zobov. "Suppression of Higher Order Modes in an Array of Cavities Using Waveguides". In: *6th International Particle Accelerator Conference*. Richmond, VA, USA, 2015, pp. 3033–3035.

[19] M. Ellison, M. Ball, B. Brabson, J. Budnick, D. D. Caussyn, A. W. Chao, J. Collins, S. A. Curtis, V. Derenchuk, S. Dutt, G. East, T. Ellison, D. Friesel, W. Gabella, B. Hamilton, H. Huang, W. P. Jones, W. Lamble, S. Y. Lee, D. Li, M. G. Minty, S. Nagaitsev, K. Y. Ng, X. Pei, G. Rondeau, T. Sloan, M. Syphers, S. Tepikian, Y. Yan, and P. L. Zhang. "Driven response of the synchrotron motion of a beam". In: *Phys. Rev. Lett.* 70.5 (1993), pp. 591–594.

[20] M. Syphers, M. Ball, B. Brabson, J. Budnick, D. Caussyn, A. W. Chao, J. Collins, V. Derenchuk, S. Dutt, G. East, M. Ellison, T. Ellison, D. Friesel, W. Gabella, B. Hamilton, H. Huang, W. P. Jones, S. Y. Lee, D. Li, M. G. Minty, S. Nagaitsev, K. Y. Ng, X. Pei, G. Rondeau, T. Sloan, T. Teng, S. Tepikian, Y. Wang, Y. T. Yan, and P. L. Zhang. "Experimental study of synchro-betatron coupling induced by dipole modulation". In: *Phys. Rev. Lett.* 71.5 (1993), pp. 719–722.

[21] H. Huang, M. Ball, B. Brabson, J. Budnick, D. D. Caussyn, A. Chao, J. Collins, V. Derenchuk, S. Dutt, G. East, M. Ellison, D. Friesel, B. Hamilton, W. Jones, S. Lee, D. Li, M. Minty, S. Nagaitsev, K. Ng, X. Pei, A. Riabko, T. Sloan, M. Syphers, L. Teng, Y. Wang, Y. Yan, and P. Zhang. "Experimental determination of the Hamiltonian for synchrotron motion with rf phase modulation". In: *Phys. Rev. E* 48.6 (1993), pp. 4678–4688.

[22] D. Li, M. Ball, B. Brabson, J. Budnick, D. D. Caussyn, A. W. Chao, G. East, M. Ellison, D. Friesel, B. Hamilton, H. Huang, W. P. Jones, S. Y. Lee, M. G. Minty, S. Nagaitsev, K. Ng, X. Pei, T. Sloan, M. Syphers, L. Teng, Y. Wang, Y. Yan, and P. L. Zhang. "Experimental measurement of resonance islands induced by rf voltage modulation". In: *Phys. Rev. E* 48.3 (1993), R1638–R1641.

[23] D. Li, M. Ball, B. Brabson, J. Budnick, D. Caussyn, A. Chao, V. Derenchuk, S. Dutt, G. East, M. Ellison, D. Friesel, B. Hamilton, H. Huang, W. Jones, S. Lee, J. Liu, M. Minty, K. Ng, X. Pei, A. Riabko, T. Sloan, M. Syphers, Y. Wang, Y. Yan, and P. Zhang. "Effects of rf voltage modulation on particle motion". In: *Nuclear Instruments and Methods in Physics Research Section A: Accelerators, Spectrometers, Detectors and Associated Equipment* 364.2 (1995), pp. 205–223.

[24] N. Abreu, R. Farias, and P. Tavares. "Longitudinal dynamics with RF phase modulation in the LNLS electron storage ring". In: *Phys. Rev. ST* 9.1433 (2006).

[25] "Center for Synchrotron Radiation at the TU Dortmund University". `http://www.delta.tu-dortmund.de`. Accessed: 26. August 2018.

[26] K. Wille. "Initial Experience with DELTA". In: *5th European Particle Accelerator Conference*. paper WEX01T. Barcelona, Spain, 1996, pp. 95–98.

[27] G. Schmidt, U. Berges, K. Dunkel, J. Friedl, A. Gasper, M. Grewe, P. Hartmann, R. Heine, E. Kasel, B. Keil, D. Schirmer, T. Weis, K. Wille, and D. Zimoch. "Status of the Synchrotron Light Source DELTA". In: *8th European Particle Accelerator Conference*. paper TUPRI006. Paris, France, 2002, pp. 745–747.

[28] F. Marhauser, E. Weihreter, D. M. Dykes, and P. McIntosh. "HOM Damped 500 MHz Cavity Design for 3rd Generation SR Sources". In: *Particle Accelerator Conference*. paper MPPH033. Chicago, USA, 2001, pp. 846–848.

[29] F. Marhauser and E. Weihreter. "First Tests of a HOM-Damped High Power 500 MHz Cavity". In: *9th European Particle Accelerator Conference*. paper TUPKF011. Lucerne, Switzerland, 2004, pp. 979–981.

[30] R. Heine, P. Hartmann, and T. Weis. "Characterisation of the EU-HOM-Damped Normal Conducting 500 MHz Cavity from the Beam Power Spectrum at DELTA". In: *10th European Particle Accelerator Conference*. paper THPCH035. Edinburgh, Scotland, 2006, pp. 2856–2858.

[31] R. G. Heine. "Untersuchung der Wechselwirkung intensiver Elektronenstrahlen mit höheren Resonatormoden an Delta". Dissertation. TU Dortmund University, 2006.

[32] J. Fürsch. "Lebensdauerverbesserung und Strahlstabilisierung durch longitudinale Phasenmodulation am Elektronenspeicherring Delta". Dissertation. TU Dortmund University, 2014.

[33] M. Bursy. "Untersuchung zur Wirkungsweise der Phasenmodulation an DELTA". Master thesis. TU Dortmund University, 2016.

[34] K. Wille. "The Physics of Particle Accelerators". Oxford University Press, 2000. ISBN: 3-519-03087-X.

[35] H. Padamsee, J. Knobloch, and T. Hays. "RF Superconductivity for Accelerators". 2nd ed. Wiley-VCH Verlag GmbH & Co. KGaA, Weinheim, 2011. ISBN: 978-3-527-408429.

[36] T. P. Wangler. "RF Linear Accelerators". 2nd ed. Wiley-VCH Verlag GmbH & Co. KGaA, Weinheim, 2008. ISBN: 978-3-527-40680-7.

[37] J. Johann. "Modulationsverfahren". Springer Verlag Berlin Heidelberg, 1992. ISBN: 3-540-55769-5.

[38] M. Giovannozzi. "Proposed scaling law for intensity evolution in hadron storage rings based on dynamic aperture variation with time". In: *Phys. Rev. ST Accel. Beams* 15 (2012), p. 024001.

[39] F. Orsini and A. Mosnier. "Effectiveness of rf phase modulation for increasing bunch length in electron storage rings". In: *Phys. Rev. E* 61.4 (2000), pp. 4431–4440.

[40] J. Byrd, W.-H. Cheng, and F. Zimmermann. "Nonlinear effects of phase modulation in an electron storage ring". In: *Phys. Rev. E* 57.4 (1998), pp. 4706–4712.

[41] M. A. Jebramcik. “RF Phase Modulation in the Context of Coherent Harmonic Generation at the DELTA Storage Ring”. Master thesis. TU Dortmund University, 2016.

[42] T. Weiland and R. Wanzenberg. “Wake fields and impedances”. In: *Lect. Notes Phys.* 400.DESY-M-91-06 (1991).

[43] P. A. M. Dirac. “The Principles of Quantum Mechanics”. 3rd ed. Oxford University Press, 1947. ISBN: 9780198520115.

[44] A. W. Chao. “Physics of Collective Beam Instabilities in High Energy Accelerators”. Available online at http://www.slac.stanford.edu/~achao/wileybook.html. John Wiley & Sons Inc., 1993. ISBN: 0-471-55184-8.

[45] G. B. Arfken and H. J. Weber. “Mathematical Methods for Physicists”. 6th ed. Elsevier Academic Press, 2005. ISBN: 0-12-088584-0.

[46] M. Höner. “Investigation of Transient Processes at the DELTA Electron Storage Ring Using a Digital Bunch-by-Bunch Feedback System”. Dissertation. TU Dortmund University, 2016.

[47] S. Khan, T. Knuth, W. Barry, J. Byrd, and G. Stover. “Commissioning results of the transverse Feedback system at BESSY-II”. In: *Proceedings of EPAC*. Vienna, Austria, 2000, pp. 1912–1914.

[48] M. Migliorati and L. Palumbo. “Multibunch and multiparticle simulation code with an alternative approach to wakefield effects”. In: *Phys. Rev. ST Accel. Beams* 18.3 (2015), p. 031001.

[49] P. Furlan. “Das Gelbe Rechenbuch 3”. Verlag Martina Furlan, 2008. ISBN: 3-931645-02-9.

[50] P. Horowitz and W. Hill. “The Art of Electronics”. 2nd ed. Cambridge University Press, 1989. ISBN: 0-521-37095-7.

[51] M. Lonza. “Multi Bunch Feedback Systems”. In: *Cern Accelerator School 2007*. Sigtuna, Sweden, 2007, pp. 285–330.

[52] G. Rumolo. “Beam Instabilities”. In: *CERN Accelerator School: Advanced Accelerator Physics*. Trondheim, Norway, 2013, pp. 199–219.

[53] F. Sacherer. “A Longitudinal Stability Criterion for Bunched Beams”. In: *IEEE Transactions on Nuclear Science* 20.3 (1973), pp. 825–829.

[54] L. Landau. “On the vibrations of the electronic plasma”. In: *Journal of Physics* 10.1 (1946), pp. 25–34.

[55] S. Sakanaka, M. Izawa, T. Mitsuhashi, and T. Takahashi. "Improvement in the beam lifetime by means of an rf phase moudlation at the KEK Photon Factory storage ring". In: *Phys. Rev. ST Accel. Beams* 3.5 (2000), p. 050701.

[56] W. Herr. "Introduction to Landau Damping". In: *CERN Accelerator School: Advanced Accelerator Physics* (2013), pp. 377–404.

[57] MHF-E-Department. "The 1-cell DORIS-Cavity". https://mhf-e.desy.de/e519/e187129/e187151/. Accessed: 10. June 2019.

[58] S. Full, A. Bartnik, I. Bazarov, J. Dobbins, B. Dunham, and G. Hoffstaetter. "Deterction and clearing of trapped ions in the high current Cornell photoinjector". In: *Phys. Rev. ST Accel. Beams* 19.3 (2016), p. 034201.

[59] D. Schirmer. "Synchrotron radiation sources at DELTA". Internal report. TU Dortmund University: Institute of accelerator physics and Synchrotronradiation, 2005.

[60] T. Weis. "DELTA - The Dortmund 1.5 GeV Synchrotron Light Source". Lecture notes http://www.delta.tu-dortmund.de/cms/de/Studium/Homepage_Weis/Vortraege/Vortrag_Status_DELTA_Riezlern2007.pdf. 2007.

[61] M. circuits. "JSPHS-661+, Digital Narrow Band Phase Shifter". https://www.minicircuits.com.

[62] T. instruments. "THS3202-IC, 2 GHz Low Distortion Dual Current-Feedback Amplifier". http://www.ti.com.

[63] Agilent Technologies. "33210A, Arbritrary Waveform generator". https://www.agilent.com.

[64] Dimtel Inc. https://www.dimtel.com.

[65] S. Khan and T. Knuth. "Longitudinal and Transverse Feedback Systems for BESSY-II". In: *AIP Conference Proceedings, 8. beam instrumentation workshop*. Vol. 451. Stanford, CA, United States, 1998, pp. 537–544.

[66] Milmega. "AS0102-200, Broadband Power Amplifier". http://www.milmega.co.uk.

[67] Amplifier Research. "Model 100A250A, self-contained broadband amplifier". https://www.arworld.us.

[68] S. W. Smith. "The Scientist and Engineer's Guide to Digital Signal Processing". Available at www.dspguide.com. California Technical Publishing, 1997. ISBN: 0-9660176-3-3.

[69] M. Sommer. "Untersuchung eines schnellen überdämpften TM_{110}-Feedbackkickers im Vergleich mit einem Striplinekicker". Master thesis. TU Dortmund University, 2013.

[70] R. Boni, A. Gallo, A. Ghigo, F. Marcellini, M. Serio, and M. Zobov. “A Waveguide Overloaded Cavity as Longitudinal Kicker for the DAΦNE Bunch-by-Bunch Feedback System”. In: *Particle Accelerators* 52 (1996), pp. 95–113.

[71] M. Bassetti, A. Ghigo, M. Migliorati, L. Palumbo, and M. Serio. “A Time Domain Simulation Code of the Longitudinal Multibunch Instabilities”. Technical note. DAΦNE, INFN-LNF, Frascati, Italy, 1993.

[72] J. Byrd. “Simulation of the ALS Longitudinal Multibunch Feedback System”. In: *5th Particle Accelerator Conference*. Washington D.C., USA, 1993, pp. 2349–2351.

[73] E. Jones, T. Oliphant, P. Peterson, et al. “SciPy: Open source scientific tools for Python”. http://www.scipy.org/. Accessed: 30.05.2018.

[74] P. B. Wilson and J. E. Griffin. “High energy electron linacs; application to storage ring RF systems and linear colliders”. In: *AIP Conf. Proc.* 87 (1982), pp. 450–555.

[75] M. Sommer, S. Kötter, B. Isbarn, B. Riemann, and T. Weis. “Numerical Multipartilce Tracking Studies on Coupled-Bunch Instabilities in the Presence of RF Phase Modulation”. In: *9th International Particle Accelerator Conference*. paper THPAK115. Vancouver, BC, Canada, 2018, pp. 3511–3514.

[76] M. Höner. “Bunch-by-Bunch Feedback Systems at the DELTA Storage Ring”. In: *3rd International Particle Accelerator Conference*. paperMOPR015. New Orleans, Louisiana, USA, 2012, pp. 807–809.

[77] Y. Senichev, N. Hertel, S. Lunt, S. Moeller, and J. Nielsen. “Increasing the Life Time of SR Sources by RF Phase Modulation”. In: *6th European Particle Accelerator Conference*. paper THP23F. Stockholm, Sweden, 1998, pp. 1339–1341.

[78] M. Sommer, M. Höner, B. Isbarn, S. Khan, B. Riemann, and T. Weis. “Coupled-Bunch Instability Suppression Using RF Phase Modulation at the DELTA Storage Ring”. In: *6th International Particle Accelerator Conference*. paper MOPWA034. Richmond, VA, USA, 2015, pp. 179–182.

[79] Rhode & Schwarz. “FSL Spectrum Analyzer”. https://www.rohde-schwarz.com.

[80] T. Weis. “Private Communication”. TU Dortmund DELTA. 2018.

[81] T. Weis, W. Brembt, V. Kniss, and P. Hartmann. “Extract of internal report: Protokollbuch BODO-HF, DELTA-HF & Cavities”. Tech. rep. TU Dortmund University: Institute of accelerator physics and synchrotron radiation, 2000.

[82] T. Weis. “Interaction between RF-System, RF-Cavity and Beam”. Lecture notes http://www.delta.tu-dortmund.de/cms/de/Studium/Homepage_Weis/Vortraege/Vortrag_BeamLoading_Riezlern2005.pdf. 2005.

[83] D. Teytelman. “Architectures and Algorithms for Control and Diagnostics of Coupled-Bunch Instabilities in Circular Accelerators”. Ph.D. thesis. Stanford University, 2003.

[84] S. Prabhakar. “New Diagnostics and Cures for Coupled-Bunch Instabilities”. Ph.D. thesis. Stanford University, 2001.

[85] S. Prabhakar, J. Fox, D. Teytelman, and A. Young. “Phase Space Tracking of Coupled-Bunch Instabilities”. In: *Phys. Rev. ST Accel. Beams* 2.084401 (1999), pp. 90–95.

[86] J. O. Smith. “Mathematics of the Discrete Fourier Transform (DFT)”. online book, 2007 edition. http://ccrma.stanford.edu/~jos/mdft/, Accessed: 06.12.2018.

[87] M. Höner. “Investigation of Beam Instabilities at DELTA using Bunch-by-Bunch Feedback Systems”. In: *5th International Particle Accelerator Conference*. paper THPME104. Dresden, Germany, 2014, pp. 3486–3488.

[88] M. Sommer, B. Isbarn, B. Riemann, and T. Weis. “Interaction of RF Phase Modulation and Coupled-Bunch Instabilities at the DELTA Storage Ring”. In: *7th International Particle Accelerator Conference*. Busan, South Korea, 2016, pp. 1720–1723.

[89] T. Weis. “Lecture notes in accelerator physics (BP 1)”. http://www.delta.tu-dortmund.de. September 2017 - March 2018.

[90] Agilent Technologies. “ENA series Network Analyzer, E5071C, 9.0 kHz-8.5 GHz”. https://www.keysight.com/de/pdx-x202270-pn-E5071C/ena-vector-network-analyzer.

[91] G. Gonzalez. “Microwave Transistor Amplifiers: Analysis and Design”. 2nd ed. Upper Saddle River, NJ, USA: Prentice-Hall, Inc., 1996. ISBN: 0-13-254335-4.